

MODELING THE SOLVENT EFFECT, KINETICS, MORPHOLOGY AND
CATALYSIS IN POLYMERIZATION REACTIONS

by

Tuğba Özaltın

B.S., Chemistry, Boğaziçi University, 2008

M.S., Chemistry, Boğaziçi University, 2010

Submitted to the Institute for Graduate Studies in
Science and Engineering in partial fulfillment of
the requirements for the degree of
Doctor of Philosophy

Graduate Program in Chemistry

Boğaziçi University

2016

ACKNOWLEDGEMENTS

I would like to express my sincere gratitude to my thesis supervisor Prof. Viktorya Aviyente (Boğaziçi University) for her encouragement, systematic guidance and support. I gained a lot of scientific and teaching experiences thanks to her invaluable guidance. I am very proud of being her student.

Besides my advisor, I would like to thank the rest of my thesis committee, Prof. Duygu Avcı Semiz (Boğaziçi University) for her valuable comments, Prof. Canan Atılgan (Sabancı University) and Prof. Levent Demirel (Koç University) for their great contributions to my thesis and their guidance throughout the study and Assoc. Prof. Şaron Çatak (Boğaziçi University) for her contributions and advices.

I acknowledge the TÜBİTAK BİDEB graduate student scholarship for the financial support and TÜBİTAK ULAKBİM High Performance Computing Center as well as the Istanbul Technical University National Center for high Performance Computing UHEM (Project number- 5003552015) for computational resources. The Tübitak projects 113Z210 and 113T030 and Boğaziçi University research Grants under the project numbers 6981 and 9840 are gratefully acknowledged for providing the computational facilities and the necessary software.

I would like to thank all the former and current members of the Boğaziçi University Computational Chemistry group and the members of the Chemistry Department for always being kind and helpful. I cannot forget the warm family environment of the department. Special thanks go to my dear friends Gülşah Çifci Bağatır and Sesil Agopcan Çınar for their endless support and friendship.

Finally, I thank my family: my parents, sisters and especially my husband for their never ending encouragement and patience.

ABSTRACT

MODELING THE SOLVENT EFFECT, KINETICS, MORPHOLOGY AND CATALYSIS IN POLYMERIZATION REACTIONS

In this dissertation, quantum chemical tools, in particular density functional theory (DFT), molecular dynamics (MD) and coarse-grained (CG) simulations are used to address the solvent effect, kinetics, morphology and catalysis in polymerization reactions. The free-radical copolymerization kinetics of styrene (ST) and 2-hydroxyethyl methacrylate (HEMA) have been investigated by DFT in three different media (bulk, dimethylformamide (DMF), toluene). In DMF, the reactivity of the monomer HEMA, thereby its composition in the copolymer decreases because of the H-bonding tendency of the monomer with DMF. The effect of Lewis acid coordination on the propagation kinetics and mechanism of *N,N*-dimethyl acrylamide (DMAM) has also modeled with DFT. It is shown that the terminal-monomer type of propagation is the most probable pathway favoring the isotactic product formation. A multiscale approach has been used to understand the morphological behavior of thermo-responsive polymer poly (2-isopropyl-2-oxazoline) (PIPOX) in aqueous solution. The most probable structure for the PIPOX chain above T_c is obtained by torsional analysis after reverse-mapping of the CG structure followed by MD simulations. X-ray diffraction pattern well-reproduces the experimental one for crystalline PIPOX nanoribbons formed in water above T_c . The results are important in identifying a new helical conformation for PIPOX prior to crystallization. The mechanisms of cationic ring-opening polymerization of benzoxazines are still not well established. Reaction mechanisms giving phenoxy and phenolic type products have been modeled for pC-m monomer which is expected to give phenolic type product; the rearrangement mechanisms to obtain phenolic type products are also evaluated.

ÖZET

POLİMERİZASYON TEPKİMELERİNDE ÇÖZÜCÜ ETKİSİ, KİNETİK, MORFOLOJİ VE KATALİZİN MODELLENMESİ

Bu tezde kuantum kimyasal yöntemlerle, özellikle yoğunluk fonksiyoneli teorisi (YFT), moleküler dinamik (MD) ve kaba ölçekli simülasyonlar kullanılarak polimerizasyon tepkimelerinde çözücü etkisi, kinetik, morfoloji ve kataliz konuları ele alınmaktadır. Sitren (ST) ve 2-hidroksietil metakrilatın (HEMA) serbest radikal kopolimerizasyon kinetiği üç farklı ortamda (yığın, dimetil formamid (DMF), tolüen) YFT ile incelendi. DMF ortamında HEMA'nın reaktivliğinin ve bununla birlikte kopolimerdeki içeriğinin monomerin polar çözücü ile H-bağı yapma eğiliminden dolayı azaldığı gösterildi. Lewis asit koordinasyonunun *N,N*-dimetil akrilamidin (DMAM) yayılma kinetiği ve mekanizmasına etkisi YFT ile incelendi. Son birim -monomer tipi yayılmanın izotaktik ürün oluşumunu destekleyen en olası yol olduğu gösterildi. Sıcaklığa duyarlı polimer poli(2-izopropil-2-oksazolin)in (PIPOX) sulu çözeltideki morfolojik davranışı farklı hesapsal yaklaşımlarla incelendi. T_c üzerinde en olası PIPOX yapısı kaba ölçekli yapının tersinir eşleştirmesi ve moleküler dinamik simülasyonlarından sonra burulma açısı analizleriyle elde edildi. En olası PIPOX zinciriyle elde edilen X-ışını kırınım şekli, suda T_c üzerinde oluşan kristal yapılı PIPOX nano şeritlerin deneysel X-ışını kırınım şekline uyum sağlamaktadır. Sonuçlar kristallenmeden önce yeni bir sarmal PIPOX konformasyonunun tanımlanması açısından önemlidir. Benzoxazinlerin katyonik halka açılma polimerizasyonlarının mekanizmaları hala iyi bilinmemektedir. Fenolik ürün vermesi beklenen pC-m monomerinin fenoksi ve fenolik ürün veren tepkime mekanizmaları modellendi; fenolik ürün elde etmek için olası düzenlenme mekanizmaları da ayrıca değerlendirildi.

TABLE OF CONTENTS

ACKNOWLEDGEMENTS	iii
ABSTRACT	iv
ÖZET	v
LIST OF FIGURES	ix
LIST OF TABLES	xiii
LIST OF SYMBOLS	xv
LIST OF ACRONYMS/ABBREVIATIONS	xvi
1. INTRODUCTION	1
2. OBJECTIVE AND SCOPE	1
3. THEORETICAL BACKGROUND	2
3.1. Quantum Mechanics	2
3.2. Hartree-Fock Theory	4
3.3. Density Functional Theory	5
3.4. Basis Sets	11
3.5. Solvation Models	12
3.6. Molecular Dynamics	14
3.6.1. COMPASS Forcefield	16
3.7. Dissipative Particle Dynamics	17
4. MODELING THE SOLVENT EFFECT AND CATALYSIS IN FREE RADICAL POLYMERIZATION	21
4.1. Solvent Effects on Free-Radical Copolymerization of Styrene and 2-Hydroxyethyl Methacrylate	21
4.1.1. Introduction	21
4.1.2. Computational Procedure	28
4.1.3. Results and Discussion	32
4.1.3.1. 3D Structures	32
4.1.3.2. Kinetics	37
4.1.4. Conclusions	43
4.2. Effect of Catalysts on the Stereoregularity of Dimethyl Acrylamide	44

4.2.1.	Introduction	44
4.2.2.	Computational Procedure	48
4.2.3.	Results and Discussion	51
4.2.3.1.	Unimeric reactants	51
4.2.3.2.	Dimeric Transition States	52
4.2.3.3.	Trimeric Transition States	54
4.2.3.4.	Dimeric radicalic chains	55
4.2.3.5.	Trimeric radicalic chains	55
4.2.3.6.	Kinetic Results	58
4.2.4.	Conclusions	61
5.	MULTISCALE MODELING OF POLY(2-ISOPROPYL-2-OXAZOLINE) CHAINS IN AQUEOUS SOLUTION	62
5.1.	Introduction	62
5.2.	Computational Procedure	67
5.2.1.	MD Simulations of single oligomeric chains in water	67
5.2.2.	DPD simulations of multiple oligomers in water	68
5.2.3.	Sample calculation for the average repulsion between interacting beads for PIPOX at 60°C	70
5.2.4.	Reverse-mapping and further system relaxation	71
5.2.5.	XRD analysis	72
5.3.	Results and Discussion	72
5.3.1.	Single chain properties of PIPOX in water	72
5.3.2.	Morphologies of PIPOX chains in water	75
5.3.3.	Structure and Stability of Crystalline PIPOX Fibers	79
5.4.	Conclusions	81
6.	MODELING THE KINETICS IN CATIONIC RING-OPENING POLYMER- IZATION OF BENZOXAZINES	83
6.1.	Introduction	83
6.2.	Computational Procedure	85
6.3.	Results and Discussion	86
6.3.1.	Ring-Opening Upon Protonation	86

6.3.2. Type I and Type II Chain Propagation Mechanisms for pC-m	90
6.3.3. Rearrangement of phenoxy product to phenolic product	90
6.4. Conclusions and Future Work	91
7. CONCLUDING REMARKS	93
REFERENCES	95

LIST OF FIGURES

Figure 4.1.	Homopolymerization and copolymerization of HEMA and styrene.	30
Figure 4.2.	Stereoselective Radical (<i>syn</i>) Addition to HEMA (<i>s-cis</i> and <i>s-trans</i>).	31
Figure 4.3.	Gas phase optimized geometries of a) Pro- <i>meso</i> and b) Pro- <i>racemo</i> transition states with M06-2X/6-31+G(d,p) methodology (Relative Gibbs Free Energies (kcal/mol) are in parenthesis).	33
Figure 4.4.	Sample calculation in toluene for HEMA-HEMA homopolymerization.	34
Figure 4.5.	Propagation transition states of HEMA (M06-2X/6-31+G(d,p)). .	35
Figure 4.6.	Propagation transition states of ST (M06-2X/6-31+G(d,p)). . . .	36
Figure 4.7.	Copolymerization transition states of ST/HEMA copolymer system (M06-2X/6-31+G(d,p)).	38
Figure 4.8.	Copolymerization Gibbs free energy profiles for the propagation reactions when a) there is no solvent, b) when the reactants are stabilized and, c) when the transition state is stabilized by solvent molecules (R: Reactant, R-S: Reactant-Solvent complex and P: Product).	39
Figure 4.9.	Copolymer composition data for ST/HEMA system, mole fraction of HEMA in the copolymer (F_{HEMA}) as a function of HEMA mole fraction in solution (f_{HEMA}) (M06-2X/6-31+G(d,p)).	42

Figure 4.10. Stereoselectivity during radical polymerization of DMAM in the absence (1) and the presence (2-4) of ScCl_3 as Lewis acid.	48
Figure 4.11. Stereoselective radical (<i>syn</i> and <i>anti</i>) addition to DMAM (s-cis and s-trans).	50
Figure 4.12. First (A) and second (B) propagation steps for the polymerization of DMAM.	51
Figure 4.13. Relative Gibbs free energies (kcal mol^{-1}), dipole moments (D) in parentheses, and Gibbs stabilization energies (kcal mol^{-1}) in square brackets for the reactants in the absence and the presence of ScCl_3 in methanol (M06-2X/6-311+G(d,p)).	53
Figure 4.14. Relative Gibbs free energies (kcal mol^{-1}), and dipole moments (D) in parentheses for the dimeric transition states in methanol (M06-2X/6-311+G(d,p)).	56
Figure 4.15. Relative Gibbs free energies (kcal mol^{-1}), and dipole moments (D) in parentheses for the trimeric transition states in methanol (M06-2X/6-311+G(d,p)).	57
Figure 4.16. Relative Gibbs free energies (kcal mol^{-1}), and dipole moments (D) in parentheses for the dimeric radicalic chains in the absence and presence of ScCl_3 in methanol (M06-2X/6-311+G(d,p)).	58
Figure 4.17. Relative Gibbs free energies (kcal mol^{-1}), and dipole moments (D) in parentheses for the trimeric products in the absence and presence of ScCl_3 in methanol (M06-2X/6-311+G(d,p)).	60
Figure 5.1. Partitioning of the beads for DPD simulations.	68

Figure 5.2.	PIPOX and solvent beads used in the pattern document. A centroid was created for each bead (green beads in the centers). Green lines and numbers represent the distance of each atom to the center of mass of the bead (centroid) it belongs. Distances are kept constant by adding harmonic restraints (white dots).	72
Figure 5.3.	Radial Distribution Functions for the Hydrogen Bonding Interactions between PIPOX and water at two different temperatures. . .	73
Figure 5.4.	Numbering of the PIPOX chain (8 repeating units) for torsional analysis.	74
Figure 5.5.	PIPOX conformations displaying the most frequently observed torsional angles in the MD simulations.	74
Figure 5.6.	DPD simulation results for the aqueous solutions of PIPOX. . . .	76
Figure 5.7.	Density field representations of six successive frames (125 th -130 th ps) during the MD simulations at 40°C.	77
Figure 5.8.	Reverse-mapping result for the PIPOX aqueous solution above T_c	77
Figure 5.9.	The most-probable PIPOX chain at 60°C after MD simulation to the reverse-mapped system.	78
Figure 5.10.	Triclinic unit cell assigned to two helical PIPOX chains: $a = 11.30 \text{ \AA}$; $b = 5.00 \text{ \AA}$; $c = 6.37 \text{ \AA}$; $\alpha = 76^\circ$; $\beta = 89^\circ$; $\gamma = 88^\circ$; (b) XRD data: Crystalline PIPOX nanoribbons formed in H ₂ O at 65°C (black); calculated XRD of the unit cell in (a) (red).	80

Figure 5.11.	(a) The pair of helical chains selected for stability analysis. (b) Chains that are immersed in water as a pair and (c) a single chain in water at the end of 1 ns equilibration.	81
Figure 6.1.	Methyl substituted benzoxazines to be modeled.	85
Figure 6.2.	Ring-opening, propagation and rearrangement mechanisms for pC-m.	86
Figure 6.3.	Most stable conformers for the monomer pC-m.	87
Figure 6.4.	Protonated monomers and their relative Gibbs free energies (kcal/mol). (M06-2X/6-31+G(d,p) – CPCM).	88
Figure 6.5.	Gibbs free energy, ΔG^\ddagger and activation energy barriers (in parenthesis), E_a (kcal/mol) for TS1 for pC-m with trifluoroacetic acid (CF_3COOH) and acetic acid (CH_3COOH). (B3LYP/6-31+G(d)-Gas phase).	88
Figure 6.6.	Reaction paths and Gibbs free energy barriers for Type I and Type II chain propagation steps (M06-2X/6-31+G(d,p) – CPCM). . . .	89
Figure 6.7.	Mechanisms for model reactions.	90
Figure 6.8.	Reaction paths and Gibbs free energy barriers for rearrangement mechanism (2011) with the mechanisms for model reactions in Figure 6.7 (M06-2X/6-31+G(d,p) – Gas phase).	91

LIST OF TABLES

Table 4.1.	Sum of electronic and thermal Gibbs Free Energies for the structures in Figure 4.3.	32
Table 4.2.	Parameters for sample calculation in toluene for HEMA-HEMA Homopolymerization (M06-2X/6-31+G(d,p)).	34
Table 4.3.	Gas phase standard (at 298 K), activation barriers (kcal/mol) and stabilization energies (kcal/mol) (M06-2X/6-31+G(d,p)).	40
Table 4.4.	Activation energy barriers E_a (kcal/mol), Gibbs free energies of activation ΔG^\ddagger (kcal/mol), propagation rate constants k_p (L/mol.s), pre-exponential factors A (L/mol.s), monomer reactivity ratios and relative propagation rate constants (Experimental values [52] are in parenthesis) at 298.15 K.	41
Table 4.5.	Mulliken atomic spin densities (M06-2X/6-31+G(d,p)) for the radicalic carbon atoms of HEMA and ST radicals.	43
Table 4.6.	Experimental findings for stereocontrol in the presence of Lewis acids in methanol [131].	47
Table 4.7.	Gibbs free energy barriers, (ΔG^\ddagger , kcal mol ⁻¹), activation energy barriers, (E_a , kcal mol ⁻¹), propagation rate constants, (k_p , L mol ⁻¹ s ⁻¹), and tacticity percentages of the best dimeric and trimeric transition state pathways at 298.15 K (M06-2X/ 6-311+G(d,p)).	59
Table 5.1.	The most frequently observed torsional angles during MD simulations for PIPOX (8 repeating units).	75

Table 6.1.	Relative Gibbs Free Energies (kcal/mol) of the most stable conformers of monomer pC-m. (Relative electronic energies (kcal/mol) are given in the parenthesis). (Functional/6-31+G(d,p)).	87
------------	--	----

LIST OF SYMBOLS

E_x^{exact}	Exact exchange energy
$E_c[\rho]$	Correlation energy
$E_x[\rho]$	Exchange energy
$E_{\sigma\sigma^*}$	Non-covalent contributions to the energy
$J[\rho]$	Coulomb energy
$T[\rho]$	Kinetic energy of interacting electrons
$T_s[\rho]$	Kinetic energy of non-interacting electrons
$U_{x\sigma}$	Exchange energy density
$V_{ee}[\rho(r)]$	Interelectronic interactions
$V_{ext}(r)$	External potential
V_{KS}	Kohn-Sham potential
ΔE^\ddagger	Electronic activation energy
ΔE_x^{B88}	Becke's gradient correction
ΔE_0	Relative electronic energy at 0 K
ΔE_{0+ZPE}	Sum of the change in electronic and zero point energy at 0 K
ΔG^\ddagger	Gibbs free energy of activation
ΔH_{rxn}	Heat of reaction as electronic energy
$v(r)$	External potential
$\rho(r)$	Electron density
ψ_i	Kohn-Sham potential

LIST OF ACRONYMS/ABBREVIATIONS

B3LYP	Becke-3-parameter Lee-Yang-Parr functional
B88	Becke 88 exchange functional
BMK	Boese-Martin for Kinetics
DFT	Density Functional Theory
HF	Hartree-Fock theory
LDA	Local Density Approximation
M06-2X	Empirical exchange-correlation functionals

1. INTRODUCTION

Computational chemistry is a field of chemistry that complements experimental data on the structures, properties and reactions of substances. It has been used in a wide range of research areas such as materials science and drug discovery. It is particularly useful for the determination of properties that are inaccessible experimentally and for the interpretation of experimental data. Making predictions by computation before running the actual time-consuming experiments is very advantageous for chemists. Also, it is a powerful tool to explore reaction mechanisms that are not easy to study by experimental means.

In this dissertation, the solvent and catalyst effects on the polymer tacticity and kinetics in free radical polymerization (Chapter 4), polymer morphology (Chapter 5) and reaction mechanism of a cationic ring-opening polymerization (Chapter 6) have been explored by computational tools.

Acrylic copolymers are used as binder resins in solvent-borne automotive coatings. Copolymer composition and distribution of reactive functional groups are critical since they change the physical properties of the product. 2-Hydroxyethyl methacrylate (HEMA) is an important functional monomer used in the coatings industry. It is highly polar, so its usage in the formation of copolymer chains has gained attention since it was found that polarity and hydrophilicity of solvents affect copolymer composition and the copolymerization rate of styrene/2-hydroxyethyl methacrylate (ST/HEMA) system. So, in this dissertation, the effect of solvent on the polymerization rate and copolymer composition of the system is discussed in Section 4.1.

Tacticity is a measure of stereoregularity of a polymer chain and many of the polymer properties such as tensile strength, melting point, and solubility depend on it. There are two fundamental approaches for stereochemical control of polymers during free radical polymerization: catalytic control of the propagating chain end using Lewis acids, solvents, and chiral auxiliaries, and the use of polymerizations in organized and

constrained media. The isotactic specific radical polymerization of various acrylamides and methacrylamides was achieved in the presence of a catalytic amount of Lewis acids such as $\text{Y}(\text{OTf})_3$ and $\text{Yb}(\text{OTf})_3$. In Section 4.2, the control of stereoregulation by the aid of Lewis acids during free radical polymerization is examined by using computational tools. Comparison of the calculated results with experiment will shed light on the role of the medium on the control of stereoregularity of the polymeric chain.

Solvation is important in lowering the kinetic barriers in the crystallization process, and it affects the morphology of the polymeric materials. Poly(2-isopropyl-2-oxazoline) (PIPOX) is a structural isomer of poly(*N*-isopropyl acrylamide) (PNIPAM) which also shows lower critical solution temperature (LCST) behaviour around human body temperature. However, in contrast to PNIPAM, it undergoes irreversible phase transition above its critical temperature (T_c) and forms nanoribbons by self-crystallization in water. In Chapter 5, the morphological behaviour of PIPOX in water around its T_c have been explored.

Computational chemistry allows the investigation of challenging reaction mechanisms. It is possible to locate the short-lived intermediates and transition states by theoretical modeling. 1,3-Benzoxazines are a class of heterocyclic compounds which are able to undergo ring opening polymerization, resulting in highly advanced materials in terms of mechanical strength, thermal stability, and durability in humid environment. However, since the spectroscopic observation of active species is difficult, mechanism of ring opening polymerization of benzoxazines remained speculative over the years of study on this subject. In Chapter 6, ring opening polymerization mechanisms of several benzoxazines are explored by computational means.

Overall, this dissertation addresses the challenging problems in the polymerization reactions that cannot be solved easily by experimental means. Observation of reaction mechanisms and controlling stereoregulation in free radical polymerization reactions are difficult because of the highly active character of the free radicals. This thesis provides a deeper insight into the solvent and catalysis effects on the free radical

polymerization reactions and reaction mechanisms in cationic ring-opening polymerizations by modeling. Also, crystallization behavior of a thermoresponsive polymer is examined by a practical multi-scale approach that brings a new perspective to the investigation of a physical behavior of a polymer by computational chemistry tools.

2. OBJECTIVE AND SCOPE

In the first section of the dissertation, a brief introduction to the use of computational chemistry in the investigation of solvent effects, catalysis, morphology and kinetics of polymer reactions is given. More detailed discussion of each one is presented in the following chapters.

In Chapter 3 (Theoretical Background), the fundamental principles of the methodologies involved in this thesis, including Density Functional Theory, Molecular Dynamics, Dissipative Particle Dynamics, Reverse Mapping and Powder Diffraction are introduced.

After the theoretical background section, the results of the four topics, briefly introduced in the introduction part, are thoroughly presented in individual chapters. In Chapter 4, the effect of solvent choice on the copolymerization kinetics and copolymer ratio in the ST/HEMA copolymer system and effect of Lewis acid catalysis on the polymer stereoregularity during polymerization of dimethyl acrylamide (DMAM) are explored. In Chapter 5, the morphological behavior of PIPOX in aqueous solutions around its LCST is examined. Also, crystallization of PIPOX in solution is investigated by hybrid computational tools. As the last topic of the dissertation, Chapter 6 includes the results of the reaction mechanism survey of the cationic polymerization of some benzoxazines. Finally, in Chapter 7, general conclusions drawn from each chapter and concluding remarks are presented.

3. THEORETICAL BACKGROUND

This chapter provides the basic principles of the theoretical approaches including Quantum Mechanics, Hartree-Fock Theory, Density Functional Theory, Molecular Dynamics, Dissipative Particle Dynamics, Reverse Mapping and Powder Diffraction. Because of the rich content of each theory, the most commonly used methods or the ones used in this dissertation are presented.

3.1. Quantum Mechanics

Quantum mechanical computation is based on solving the Schrödinger equation:

$$H\psi = E\psi \quad (3.1)$$

where H is the Hamiltonian energy operator, E is the energy of the system and ψ is the wave function. ψ is an amplitude function, which is the eigenfunction with E as the eigenvalue. The equation is unique for each system since the Hamiltonian for different systems are different [1]. The Hamiltonian operator can be expanded as:

$$H = - \sum_i \frac{\hbar^2}{2m_e} \nabla_i^2 - \sum_k \frac{\hbar^2}{2m_k} \nabla_k^2 - \sum_i \sum_k \frac{e^2 Z_k}{r_{ik}} + \sum_{i<j} \frac{e^2}{r_{ij}} + \sum_{k<l} \frac{e^2 Z_k Z_l}{r_{kl}}. \quad (3.2)$$

Here, m_e and m_k are the masses of the electron and the nuclei, respectively, \hbar is the Planck's constant divided by 2π , ∇^2 is the Laplacian operator, e is the charge on the electron, Z is an atomic number and r is the distance between the particles. The first two terms are the kinetic energy of the electrons and the nuclei, respectively. The third term represents the Coulomb attraction of the electrons to the nuclei and the last two terms give the inter-electronic and internuclear repulsions, respectively.

Accurate wave functions for many-particle molecular systems are extremely difficult to express due to correlated motions of particles. That is, the Hamiltonian in Equation 3.2 contains pairwise attraction and repulsion terms, implying that no particle is moving independently of all of the others. Born-Oppenheimer approximation simplifies the problem somewhat [2]. Under typical physical conditions, the nuclei of molecular systems are moving much more slowly than the electrons. For practical purposes, electronic relaxation with respect to nuclear motion is instantaneous. So, it is convenient to decouple these two motions, and compute electronic energies for fixed nuclear positions. That is, the nuclear kinetic energy term is taken to be independent of the electrons, correlation in the attractive electron-nuclear potential energy term is eliminated, and the repulsive nuclear-nuclear potential energy term becomes a simply evaluated constant for a given geometry. Thus, the electronic Schrödinger equation becomes:

$$(H_{el} + V_{nn})\psi_{el} = E_{el}\psi_{el} \quad (3.3)$$

where H_{el} includes only the first, third, and fourth terms on the r.h.s. of Equation 3.2, V_{nn} is the nuclear-nuclear repulsion energy. The eigenvalue of the electronic Schrödinger equation is called the ‘electronic energy’.

The variational theorem provides the best solution for the many-body systems. It states that the energy calculated from an approximation to the exact wavefunction will always be higher than the true energy. This means the better the wavefunction, the lower the energy. The best wavefunction is thus obtained when the energy is minimum. The Hartree-Fock method and Density Functional Theory, which will be discussed in the next section, depend on the variational theorem.

3.2. Hartree-Fock Theory

Among the approximate ways to solve Equation 3.3, the Hartree-Fock (HF) method has a prominent status to pave the way for more accurate calculations in modern quantum chemistry. The HF method starts by using the single Slater determinant as an approximation to wave function of the ground state of the N -electron system:

$$\psi_{SD} = \frac{1}{\sqrt{N!}} \begin{vmatrix} \chi_1(1) & \cdots & \chi_N(1) \\ \vdots & \ddots & \vdots \\ \chi_1(N) & \cdots & \chi_N(N) \end{vmatrix} \quad (3.4)$$

which is constructed from a set of N single-electron wave functions (N being the total number of electrons in the molecule and χ a spin-orbital equal to the spin function multiplied by the spatial wave function). By applying the variational method to a single Slater determinant, the calculation of the lowest possible energy is possible through the optimization of the orbitals χ . The equations formed are called Hartree-Fock equations [1],

$$f_i \chi_i = \varepsilon_i \chi_i \quad (3.5)$$

and their solution determines the best spin orbitals for which E will reach its lowest value. In Equation 3.5, f_i is the Fock operator, χ_i is an eigenfunction of f_i and ε_i is the corresponding energy of the orbital. The one electron Fock-operator is defined for each electron i as

$$f_i = -\frac{1}{2} \nabla_i^2 - \sum_k^{\text{nuclei}} \frac{Z_k}{r_{ik}} + V_{HF}(i) \quad (3.6)$$

where the final term $V_{HF}(i)$ is the Hartree-Fock potential. $V_{HF}(i)$ represents the average repulsive potential experienced by each electron due to the other electrons. Now the interaction of each electron with the static field of all of the other electrons includes exchange effects on the Coulomb repulsion.

All ab initio quantum chemistry methods are based on Hartree-Fock (HF) method for modeling molecules. The Hartree-Fock method uses an iterative, fixed-point type algorithm in order to solve equations. Therefore, this method is also called the self-consistent field (SCF) method. That is, the orbitals are improved from cycle to cycle until the electronic energy reaches a constant minimum value and the orbitals no longer change.

Hartree-Fock theory is very helpful for providing initial, first-level predictions for many systems. It performs reasonably well for computing the structures and vibrational frequencies of stable molecules and some transition states. However, the Hartree-Fock method does not take into account the electron correlation resulting from the instantaneous repulsions between electrons. So it is not suitable for the accurate modeling of the energetics of reactions and bond dissociation. There are methods based on the calculation of the wave function including the electron correlation effects, but these methods are computationally very expensive. Instead, density functional methods which will be the focus of the next section offer a cheaper solution of this problem.

3.3. Density Functional Theory

The Density Functional Theory (DFT) [3] is based on the Kohn-Hohenberg theorems proposed in 1964 [4, 5]. It is a quantum mechanical approach to the electronic nature of atoms and molecules. Kohn-Hohenberg theorems state that all the ground-state properties of a system are functions of the charge density.

The first theorem of DFT states that the electron density $\rho(r)$ determines the external potential $v(r)$, i.e. the potential due to the nuclei. The second theorem introduces the variational principle. Hence, the electron density can be computed vari-

ationally and the position of nuclei, energy, wave function and other related parameters can be calculated.

The electron density is defined as:

$$\rho(r) = N \int \dots \int |\psi(r_1, r_2, \dots, r_n)|^2 dr_1 dr_2 \dots dr_n \quad (3.7)$$

where r represents both spin and spatial coordinates of electrons. The ground state electronic energy is a function of electron density function implying the “functional” part of DFT and is expressed as:

$$E[\rho(r)] = \int V(r) \rho(r) dr + T[\rho(r)] + V_{ee}[\rho(r)] \quad (3.8)$$

where $T[\rho]$ is the kinetic energy of the interacting electrons and $V_{ee}[\rho]$ is the interelectronic interaction energy. The electronic energy may be rewritten as

$$E[\rho(r)] = \int V(r) \rho(r) d(r) + T_{ni}[\rho(r)] + J[\rho(r)] + E_{XC}[\rho(r)] \quad (3.9)$$

with $J[\rho]$ being the coulomb energy, $T_{ni}[\rho]$ being the kinetic energy of the non-interacting electrons and $E_{XC}[\rho]$ being the exchange-correlation energy functional. The exchange-correlation functional is expressed as the sum of an exchange functional $E_X[\rho]$ and a correlation functional $E_C[\rho]$, although it contains also a kinetic energy term arising from the kinetic energy difference between the interacting and non-interacting electron systems. The kinetic energy term, being the measure of the freedom, and exchange-correlation energy, describing the change of opposite spin electrons (defining extra freedom to an electron), are the favorable energy contributions. The Coulomb energy term describes the unfavorable electron-electron repulsion energy and therefore disfavors the total electronic energy [6].

In Kohn-Sham density functional theory, a reference system of independent non-interacting electrons in a common, one-body potential V_{KS} yielding the same density as the real fully-interacting system is considered. More specifically, a set of independent reference orbitals ψ_i satisfying the following independent particle Schrödinger equation are imagined.

$$\left[-\frac{1}{2}\nabla^2 + V_{KS} \right] \psi_i = \varepsilon_i \psi_i \quad (3.10)$$

with the one-body potential V_{KS} is defined as

$$V_{KS} = v(r) + \frac{\partial J[\rho]}{\partial \rho(r)} + \frac{\partial E_{xc}[\rho]}{\partial \rho(r)} \quad (3.11)$$

$$V_{KS} = v(r) + \int \frac{\rho(r')}{|r-r'|} dr' + v_{xc}(r) \quad (3.12)$$

where $V_{xc}(r)$ is the exchange-correlation potential. The independent orbitals ψ_i are known as Kohn-Sham orbitals and give the exact density by

$$\rho(r) = \sum_i^N |\psi_i|^2 \quad (3.13)$$

if the exact form of the exchange-correlation functional is known. However, the exact form of this functional is not known and approximate forms are developed starting with the local density approximation (LDA). This approximation gives the energy of a uniform electron gas, i.e. a large number of electrons uniformly spread out in a cube accompanied with a uniform distribution of the positive charge to make the system neutral. The energy expression is

$$E[\rho] = T_s[\rho] + \int \rho(r) v(r) dr + J[\rho] + E_{xc}[\rho] + E_b \quad (3.14)$$

where E_b is the electrostatic energy of the positive background. Since the positive charge density is the negative of the electron density due to uniform distribution of particles, the energy expression is reduced to

$$E[\rho] = T_s[\rho] + E_{xc}[\rho] \quad (3.15)$$

$$E[\rho] = T_s[\rho] + E_x[\rho] + E_c[\rho] \quad (3.16)$$

The kinetic energy functional can be written as

$$T_s[\rho] = C_F \int \rho(r)^{5/3} dr \quad (3.17)$$

where C_F is a constant equal to 2.8712. The exchange functional is given by

$$E_x[\rho] = -C_x \int \rho(r)^{4/3} dr \quad (3.18)$$

with C_x being a constant equal to 0.7386. The correlation energy, $E_c[\rho]$, for a homogeneous electron gas comes from the parametrization of the results of a set of quantum Monte Carlo calculations.

The LDA method underestimates the exchange energy by about 10 percent and does not have the correct asymptotic behavior. The exact asymptotic behavior of the exchange energy density of any finite many-electron system is given by

$$\lim_{x \rightarrow \infty} U_x^\sigma = -\frac{1}{r} \quad (3.19)$$

U_x^σ being related to $E_x[\rho]$ by

$$E_x[\rho] = \frac{1}{2} \sum_{\sigma} \int \rho_{\sigma} U_x^{\sigma} dr \quad (3.20)$$

A gradient-corrected functional is proposed by Becke

$$E_x = E_x^{LDA} - \beta \sum_{\sigma} \int \rho_{\sigma}^{4/3} \frac{x_{\sigma}^2}{1 + 6\beta x_{\sigma} \sinh^{-1} x_{\sigma}} dr \quad (3.21)$$

where σ denotes the electron spin, $x_{\sigma} = \frac{|\nabla \rho_{\sigma}|}{\rho_{\sigma}^{4/3}}$ and β is an empirical constant ($\beta = 0.0042$). This functional is known as Becke88 (B88) functional [5].

The adiabatic connection formula connects the non-interacting Kohn-Sham reference system ($\lambda = 0$) to the fully-interacting real system ($\lambda = 1$) and is given by

$$E_{xc} = \int_0^1 U_{xc}^{\lambda} d\lambda \quad (3.22)$$

where λ is the interelectronic coupling-strength parameter and is the potential energy of exchange-correlation at intermediate coupling strength. The adiabatic connection formula can be approximated by

$$E_{xc} = \frac{1}{2} E_x^{exact} + \frac{1}{2} U_{xc}^{LDA} \quad (3.23)$$

since $U_{xc}^0 = E_x^{exact}$, the exact exchange energy of the Slater determinant of the Kohn-Sham orbitals, and $U_{xc}^1 = U_{xc}^{LDA}$ [4].

The closed shell Lee-Yang-Parr (LYP) correlation functional [7] is given by

$$(E_c = -a \int \frac{1}{1 + d\rho^{-1/3}} \{ \rho + b\rho^{-2/3} [C_F \rho^{5/3} - 2t_w + (\frac{1}{9}t_w + \frac{1}{18}\nabla^2\rho)] e^{-c\rho^{-1/3}} dr \quad (3.24)$$

where

$$t_w = \frac{1}{8} \frac{|\nabla\rho(r)|^2}{\rho(r)} - \frac{1}{8} \nabla^2\rho \quad (3.25)$$

The mixing of LDA, B88, E_x^{exact} and the gradient-corrected correlation functionals to give the hybrid functionals [8] involves three parameters.

$$E_{xc} = E_{xc}^{LDA} + a_0 (E_x^{exact} - E_x^{LDA}) + a_x \Delta E_x^{B88} + a_c \Delta E_c^{non-local} \quad (3.26)$$

where ΔE_x^{B88} is the Becke's gradient correction to the exchange functional. In the B3LYP functional, the gradient-correction ($\Delta E_c^{non-local}$) to the correlation functional is included in LYP. However, LYP contains also a local correlation term which must be subtracted to yield the correction term only.

$$\Delta E_c^{non-local} = E_c^{LYP} - E_c^{VWN} \quad (3.27)$$

where E_c^{VWN} is the Vosko-Wilk-Nusair correlation functional, a parametrized form of the LDA correlation energy based on Monte Carlo calculations. The empirical coefficients are $a_0=0.20$, $a_x=0.72$ and $a_c=0.81$ [9].

M06-2X [10] is another hybrid functional introduced by Zhao et al. and this hybrid functional is extensively used in this thesis. The hybrid exchange-correlation

can be written as follows:

$$E_{XC}^{hyb} = \frac{X}{100} E_X^{HF} + \left(1 - \frac{X}{100}\right) E_X^{DFT} + E_C^{DFT} \quad (3.28)$$

where X (X=54 in the case of M06-2X functional) is the percentage of Hartree–Fock exchange in the hybrid functional and corresponds to a in Equation 3.26.

3.4. Basis Sets

The basis set is the set of mathematical functions from which the wave function is constructed. A complete basis set means that an infinite number of functions must be used, which is impossible in actual calculations. An unknown MO can be thought of as a function in the infinite coordinate system spanned by the complete basis set. When a finite basis set is used, only the components of the MO along those coordinate axes corresponding to the selected basis functions can be represented. The smaller the basis set, the poorer the representation. However, the better a single basis function is able to reproduce the unknown function, the fewer basis functions are necessary for achieving a given level of accuracy [11]. There are two types of basis functions commonly used in electronic structure calculations: Slater Type Orbitals (STO) and Gaussian Type Orbitals (GTO), the latter being the extensively studied one in modern DFT.

The next level of basis sets developed by Pople is referred to as the split-valence basis sets. The problem of any minimal basis set is its inability to expand or contract its orbitals to fit the molecular environment. One solution to the problem is to use split valence or double zeta basis sets in which the basis sets are split into two parts, an inner, compact orbital and an outer, more diffuse one. Thus the size of the atomic orbital that contributes to the molecular orbital can be varied within the limits set by the inner and outer basis functions. Split-valence basis set splits only the valence orbitals in this way, whereas double zeta basis also have split core orbitals.

Basis sets can be further modified with the addition of two functions: polarization and diffuse functions. Polarization functions add higher angular momentum orbital to all heavy atoms designated with a * or (d). Hydrogen atoms can be polarized as well, this would be done by ** or (d,p). Diffuse functions, represented by a “+”, allow orbitals to occupy larger spaces. The inclusion of diffuse functions in the basis sets is important especially in the case of anions, weak interactions and lone pairs.

The selection of appropriate functional and basis set for quantum chemical calculations is very important and calculations can often be improved by the addition of diffuse and polarization functions. However, the level of DFT functional and the basis sets should be arranged with respect to the properties of the system modeled as well as to which property of the system we seek for an answer.

3.5. Solvation Models

Continuum solvation models are the most efficient way to include condensed-phase effects into quantum mechanical calculations [12]. Advantage of these models is that they decrease the number of the degrees of freedom of the system by describing them in a continuous way, usually by means of a distribution function [13, 14]. In continuum solvation models, the solvent is represented as a polarizable medium characterized by its static dielectric constant ϵ and the solute is embedded in a cavity surrounded by this dielectric medium. The total solvation free energy is defined as

$$\Delta G_{solvation} = \Delta G_{cavity} + \Delta G_{dispersion} + \Delta G_{electrostatic} + \Delta G_{repulsion} \quad (3.29)$$

where ΔG_{cavity} is the energetic cost of placing the solute in the medium. Dispersion interactions between solvent and solute are expressed as $\Delta G_{dispersion}$, this adds stabilization to solvation free energy. $\Delta G_{electrostatic}$ is the electrostatic component of the solute-solvent interaction energy. $\Delta G_{repulsion}$ is the exchange solute-solvent interactions not included in the cavitation energy.

The central problem of continuum solvent models is the electrostatic problem described by the general Poisson equation:

$$-\vec{\nabla} \left[\epsilon(\vec{r}) \nabla \vec{V}(\vec{r}) \right] = 4\pi \rho_M(\vec{r}) \quad (3.30)$$

simplified to

$$-\nabla^2 V() = 4\pi \rho_M(\vec{r}) \quad \text{within C} \quad (3.31)$$

$$-\epsilon \nabla^2 V(\vec{r}) = 0 \quad \text{outside C} \quad (3.32)$$

where C is the portion of space occupied by cavity, ϵ is dielectric function, V is the sum of electrostatic potential V_M generated by the charge distribution ρ_M and the reaction potential V_R generated by the polarization of the dielectric medium:

$$V(\vec{r}) = V_M(\vec{r}) + V_R(\vec{r}) \quad (3.33)$$

Polarizable Continuum Model (PCM) belongs to the class of polarizable continuum solvation models [15]. In PCM, the solute is embedded in a cavity defined by a set of spheres centered on atoms (sometimes only on heavy atoms), having radii defined by the van der Waals radius of the atoms multiplied by a predefined factor (usually 1.2). The cavity surface is then subdivided into small domains (called tesserae), where the polarization charges are placed. There are three different approaches to carry out PCM calculations. The original method is called Dielectric PCM (D-PCM), the second model is the Conductor-like PCM (C-PCM) [16] in which the surrounding medium is modeled as a conductor instead of a dielectric, and the third one is an implementation whereby the PCM equations are recast in an integral equation formalism (IEF-PCM) [17, 18].

3.6. Molecular Dynamics

An effective tool of computer simulations for almost 30 years is molecular dynamics (MD) which contribute the understanding of the internal motions of the systems as a function of time [19] and determining equilibrium properties. MD method is introduced in 1950s by Alder and Wainwright [20]. MD simulations were developed for more complex molecules in 1970s and first protein simulation took place in 1977 [21]. Now this method is being applied in a wide range of science such as biophysics, biochemistry, enzymology, molecular biology and materials science.

MD simulates the time-dependent behavior of a system of atoms or molecules. MD simulations employ the numerical methods instead of the analytic approach because the high number of particles and interactions between them complicate the calculations. Because of the same reason the quantum mechanical effects can be ignored. Additionally, in order to calculate the future position of the particles, the potential energy is used by MD simulations method. Generally, the energy of system is separated into two parts as bonded and non-bonded energies:

$$U_{total} = U_{bonded} + U_{nonbonded} \quad (3.34)$$

where the term non-bonded refers to the non-bonded atomic interactions and the bonded stands for the atoms being connected with three or less bonds. In general, the number of bonded interactions to be calculated is less than the non-bonded interactions due to being clearly defined and limited. On the contrary, the non-bonded interactions to be calculated are massive since each atom can potentially interact with almost all other atoms [22]. All these bonded and nonbonded interactions which are required to describe the behavior of different kinds of atoms and bonds, are called force-field [23]. All of the needed values such as energy parameters, bond lengths and bond angles are usually taken from experimental structural data or from quantum chemical calculations.

The MD simulation method simply based on the Newton's second law leading the equation of motion,

$$F_i = m_i a_i \quad (3.35)$$

where F is the force exerted of an atom in the case of molecular motion. As the gradient of the potential energy function with respect to the internal coordinates gives the force, the force acting on each atom, i could be found by the gradient of the forcefield:

$$F_i = -\frac{dU(r)}{dr_i} \quad (3.36)$$

Combining these two equations yields:

$$-\frac{dU(r)}{dr_i} = m_i \frac{d^2 r}{dt^2} \quad (3.37)$$

Potential energy is a function of positions of the atoms in the system. Hence this equation becomes very complicated and can not be solved analytically, it must be solved numerically [24]. To solve equations of motion, there are many numerical algorithms. Some of them are Verlet Algorithm, Velocity-Verlet Algorithm, Leap-Frog Algorithm. In many algorithms integration is partitioned into small steps, each of these steps is separated in specific time period Δt .

Molecular simulation of bulk matter is difficult since most simulations can only handle thousands, perhaps millions, of molecules. Using these quantities is only enough to simulate a small liquid droplet or microcrystal whereby molecules on surface boundaries have fewer neighbours and experience different forces from molecules further inside. The periodic boundary condition (PBC) is a method to simulate bulk matter and eliminate surface effects. Using PBC, a simulation box is replicated throughout

space to form an infinite lattice so that whole system properties are represented in a reasonable computation time [25].

3.6.1. COMPASS Forcefield

Condensed-phase Optimized Molecular Potentials for Atomistic Simulation Studies (COMPASS) forcefield is the first ab initio forcefield that has been parameterized and validated using condensed phase properties in addition to various ab initio and empirical data for molecules in isolation. Consequently, this forcefield enables accurate and simultaneous prediction of structural, conformational, vibrational, and thermophysical properties, that exist for a broad range of molecules in isolation and in condensed phases, and under a wide range of conditions of temperature and pressure [26].

To derive COMPASS forcefield, a hybrid approach consisting of both ab initio and empirical methods was employed based on the PCFF forcefield. In addition to the molecular classes covered in the PCFF forcefield, new molecular classes were parametrized. Especially, nonbond parameters were completely re-parametrized in this new forcefield. The functional forms used are the same as those used in CFF-type forcefields [27–34]:

$$\begin{aligned}
 E_{total} = & \sum_b [k_2(b - b_0)^2 + k_3(b - b_0)^3 + k_4(b - b_0)^4] \\
 & + \sum_\theta [k_2(\theta - \theta_0)^2 + k_3(\theta - \theta_0)^3 + k_4(\theta - \theta_0)^4]
 \end{aligned}
 \tag{3.38}$$

The functions can be divided into two categories: valence terms including diagonal and off-diagonal cross-coupling terms and nonbond interaction terms. The valence terms represent internal coordinates of bond (b), angle (θ), torsion angle (Φ), and outof-plane angle (χ), and the cross-coupling terms include combinations of two or three internal coordinates. The crosscoupling terms are important for predicting vibration frequencies and structural variations associated with conformational changes.

A large number of atom types are used for the three elements C, O, N which reflects the wide variation of the organic chemistry of these elements. Several hydrogen types are introduced, based on the polar strength of the atom that the hydrogen is attached to, from nonpolar (h1) to modest polar (h1n) and highly polar (h1o). This classification is necessary and appears to be sufficient for modeling various hydrogen bonds using the simple nonbond functions. For halogen atoms (F, Cl) in halogenated alkanes, the atom types are defined based on how many halogen atoms are attached to the same carbon atom. This is due to the strong interaction (anomeric effect) between the adjacent halogen atoms.

3.7. Dissipative Particle Dynamics

The Dissipative Particle Dynamics (DPD) is a mesoscale technique to simulate the dynamic and rheological behavior of simple and complex fluids in which the particles are clustered into coarse-grained beads. It was first developed to simulate hydrodynamic behavior by Hoogerbrugge and Koelman [35] and subsequently modified by Espanol and Warren [36]. Atomistic details of the systems studied are not considered in this method. So, it provides longer time and length scales than are possible using conventional MD simulations [37].

The time evolution of each DPD particle is calculated by Newton's second law:

$$\frac{dr_i}{dt} = v_i, \quad \frac{dp_i}{dt} = \sum_{j \neq i} F_{ij} \quad (3.39)$$

where r_i , v_i and p_i are the position, velocity and momentum vector of particle i , respectively. F_{ij} is the total interparticle force exerted on particle i by particle j and defined as:

$$F_{ij} = F_{ij}^C + F_{ij}^D + F_{ij}^R \quad (3.40)$$

where F_{ij}^C , F_{ij}^D and F_{ij}^R are the conservative force, dissipative or frictional force which represent the effects of viscosity and slows down the particles motion with respect to each other and random force between i and j beads representing the thermal and vibrational energy of system, respectively. These force components can be individually written as:

$$F_{ij}^C = \omega^C(r_{ij}) e_{ij} \quad (3.41)$$

$$F_{ij}^D = -\gamma\omega^D(r_{ij}) [v_{ij} \cdot e_{ij}] e_{ij} \quad (3.42)$$

$$F_{ij}^R = \sigma\omega^R(r_{ij}) \theta_{ij} e_{ij} \quad (3.43)$$

where $e_{ij} = r_{ij}/r_{ij}$, $r_{ij} = r_i - r_j$, $r_{ij} = |r_i - r_j|$ and $v_{ij} = v_i - v_j$. ω^C , ω^D and ω^R are conservative, dissipative and random r dependent weight functions. The θ_{ij} term is a Gaussian white noise function with symmetry property $\theta_{ij}=\theta_{ji}$ to ensure the total conservation of momentum. All of the above forces are acting within a sphere of interaction or cut-off radius r_c , which is the length scale parameter of the system. The symbols γ and σ are the coefficients of the dissipative and random forces, respectively.

The conservative force weight function can be defined as:

$$\omega^C(r_{ij}) = \begin{cases} a_{ij} \left(1 - \frac{r_{ij}}{r_c}\right) & r_{ij} \leq r_c \\ 0 & r_{ij} > r_c \end{cases} \quad (3.44)$$

where a_{ij} is the repulsion parameter between particles i and j . Defining the conservative weight function and especially the repulsion parameter is one of the most important aspects of DPD simulations.

The dissipative and random weight functions take the general form:

$$\omega^D(r_{ij}) = [\omega^R(r_{ij})]^2 = \begin{cases} \left(1 - \frac{r_{ij}}{r_c}\right)^s & r_{ij} \leq r_c \\ 0 & r_{ij} > r_c \end{cases} \quad (3.45)$$

where the exponent $s = 1$ in the original DPD algorithm and other values for s can be chosen to adjust the fluid viscosity.

Groot and Warren [38] specified the repulsion parameter between different type of particles. In order to consider interaction between components in the solution, they related the DPD parameters to the χ -parameters in Flory-Huggins theory for polymers, and subsequently obtained the relation between the χ -parameters and the repulsion parameters for unequal particles. At a given density of $\rho = 3$ relation takes the form:

$$a_{ij} \approx a_{ii} + 3.27\chi_{ij} \quad (3.46)$$

where a_{ii} is 25 in units of $k_B T$. Values larger than 25 $k_B T$ signify repulsive and those below 25 $k_B T$ signify attractive interactions between beads i and j . Solubility parameters (δ) are used to calculate the Flory-Huggins interaction parameter:

$$\chi = \frac{V_m(\delta_i - \delta_j)^2}{RT} \quad (3.47)$$

where V_m is the average molar volume of the beads.

In this thesis, the χ , Flory-Huggins interaction parameters between DPD pairs of particles were obtained from the calculation of the mixing energy through MD sim-

ulations [39], which is defined as:

$$\chi = \left(\frac{\Delta E_{mix}}{RT} \right) V_{bead} \quad (3.48)$$

where V_{bead} is the molar volume of the one repeating unit of the polymer. Also, the energy of mixing, ΔE_{mix} is defined as:

$$\Delta E_{mix} = \varphi_A \left(\frac{E_{coh}}{V} \right)_A + \varphi_B \left(\frac{E_{coh}}{V} \right)_B - \left(\frac{E_{coh}}{V} \right)_{mix} \quad (3.49)$$

A and B represent the pure components and mix defines their blends. ϕ_A and ϕ_B are the volume fractions of the pure components in the mixture. Also, E_{coh} is calculated from the relationship between solubility parameter (δ) obtained from Hildebrand's definition [40]:

$$\delta = \left(\frac{\Delta E_{coh}}{V} \right)^{1/2} = (CED)^{1/2} \quad (3.50)$$

where CED is the cohesive energy density.

4. MODELING THE SOLVENT EFFECT AND CATALYSIS IN FREE RADICAL POLYMERIZATION

4.1. Solvent Effects on Free-Radical Copolymerization of Styrene and 2-Hydroxyethyl Methacrylate

The free-radical homopolymerization and copolymerization kinetics of styrene (ST) and 2-hydroxyethyl methacrylate (HEMA) in three different media (bulk, DMF, toluene) have been investigated by means of Density Functional Theory (DFT) calculations in combination with the Polarizable Continuum Model (PCM) and the Conductor like Screening Model for Real Solvents (COSMO-RS). The conventional Transition State Theory (TST) is applied to calculate the rate parameters of polymerizations. Calculated propagation rate constants are used to predict the monomer reactivity ratios, which are then used in the evaluation of the copolymer composition following the Mayo-Lewis equation. It is found that copolymerization reactions in bulk and toluene show similar transition geometries; whereas, DMF has a tendency to form H-bonding interactions with the polar HEMA molecules, thus decreasing the reactivity of this monomer during homopolymerization and towards ST during copolymerization. Calculations of copolymer composition further show that the amount of HEMA monomer in the ST/HEMA copolymer system decreases in the polar DMF solution. The calculated spin densities of the radical species are in agreement with the rate parameters and confirm that the copolymerization propagation rate of ST/HEMA system is in the order: $k_p(\text{bulk}) \approx k_p(\text{toluene}) > k_p(\text{DMF})$.

4.1.1. Introduction

Acrylic copolymers are used as binder resins in solvent-borne automotive coatings. Copolymer composition and distribution of reactive functional groups are critical since they change the physical properties of the product. 2-hydroxyethyl methacrylate (HEMA) is an important functional monomer used in coatings industry. It is

highly polar, so its usage in the formation of copolymer chains with styrene (ST) has gained attention since it was found that polarity and hydrophilicity of solvents affect copolymer composition and the copolymerization rate of the ST/HEMA system [41]. Free-radical copolymerization is a type of chain-growth polymerization to synthesize functional polymers [42]. During free-radical copolymerization chain-growth can be made possible by one of the following four propagation steps:



It is important to monitor copolymer composition as a function of monomer reactivity and concentration at any time. By assuming a steady-state concentration of radicals during propagation, the relative change in the copolymer composition is derived by Mayo and Lewis [43]:

$$\frac{d[M_1]}{d[M_2]} = \frac{[M_1]}{[M_2]} \left(\frac{r_1 [M_1] + [M_2]}{[M_1] + r_2 [M_2]} \right) \quad (4.5)$$

where r_1 and r_2 are the monomer reactivity ratios for monomers 1 and 2 respectively. They can be defined by using the propagation rate constants:

$$r_1 = \frac{k_{11}}{k_{12}} \quad \text{and} \quad r_2 = \frac{k_{22}}{k_{21}} \quad (4.6)$$

Mayo-Lewis equation (Equation 4.5) can be used to estimate the copolymer composition at any instant during the polymerization when the monomer reactivity ratios are known. Reactivity ratios have been determined for many important monomers and tabulated in several reference sources, such as the Polymer Handbook [44].

The copolymer composition at any instant during polymerization can also be written in an alternative form by using the mole fraction of each monomer in the feed (f):

$$F_1 = 1 - F_2 = \frac{r_1 f_1^2 + f_1 f_2}{r_1 f_1^2 + 2f_1 f_2 + r_2 f_2^2} \quad (4.7)$$

where F is the mole fraction of each monomer in the copolymer, $r_1 = k_{11}/k_{12}$, $r_2 = k_{22}/k_{21}$, and k_{ij} is the propagation rate coefficient for addition of monomer-j to radical-i.

One of the simplest models used for copolymerization reactions is the terminal model [43, 45, 46], in which it is assumed that only the terminal unit of the propagating radical influences its reactivity. In a given copolymerization system in which the terminal model is valid, only two types of radicals (i.e. corresponding to the two types of terminal unit) are considered and therefore only four different propagation reactions (i.e. corresponding to the additions of the two types of radicals to the two monomers) are characterized. A refinement of the terminal model is the penultimate model [47] in which it is assumed that both the terminal and penultimate units of a polymer radical can affect its reactivity. Apart from bootstrap effect, other factors such as solvent polarity, radical-solvent and monomer-solvent complexes are demonstrated to affect the free-radical copolymerization [48]. Thus, when the Mayo-Lewis copolymer composition equation (also known as the terminal model) is not sufficient to explain the solvent effects, penultimate unit effects are used to explain the solvent dependence of copolymerization. According to penultimate unit model as originally formulated by Merz et al. [47] and used by Fukuda and co-workers [49, 50], the solvent modifies the overall propagation rate coefficient, $k_{(p, cop)}$, by affecting the reactivity of the radicals and penultimate units, where a propagation rate coefficient, k_{ijk} ($i, j, k = 1$ or 2), refers to the addition of monomer k to polymeric radical j , with i being the penultimate unit.

The overall propagation rate coefficient, $k_{(p, cop)}$, in the penultimate model is:

$$k_{p, cop} = \frac{\bar{r}_1 f_1^2 + 2f_1 f_2 + \bar{r}_2 f_2^2}{\left(\frac{\bar{r}_1 f_1}{k_{11}}\right) + \left(\frac{\bar{r}_2 f_2}{k_{22}}\right)} \quad (4.8)$$

Where

$$\bar{k}_{11} = \frac{k_{111}(r_1 f_1 + f_2)}{r_1 f_1 + \frac{f_2}{s_1}} \quad \text{and} \quad \bar{k}_{22} = \frac{k_{222}(r_2 f_2 + f_1)}{r_2 f_2 + \frac{f_1}{s_2}} \quad (4.9)$$

and the radical reactivity ratios are defined as:

$$s_1 = k_{211}/k_{111} \quad \text{and} \quad s_2 = k_{122}/k_{222} \quad (4.10)$$

According to the penultimate unit model, the solvent effect on copolymerization may be explicit or implicit. If the solvent modifies both copolymer composition and propagation rate coefficient, it is known as an explicit solvent effect; whereas, if solvent only influences the propagation rate coefficient without changing the copolymer composition (the situation when $\bar{r}_1 = r_1$ and $\bar{r}_2 = r_2$, then it is named as an implicit solvent effect following the original terminology used by Fukuda and co-workers [50]. For instance, in the case of styrene/methyl methacrylate (ST/MMA) system in benzyl alcohol, it is found that the modifications in the monomer reactivity ratios in solvent are minor, so, the copolymer composition is unchanged, but solvent induces an implicit solvent effect in the propagation rate coefficient [51].

For example, it is now very well demonstrated that polar solvents significantly affect the copolymerization reactions of donor-acceptor type copolymers through stabilization of their charge-transfer type transition state. The solvent can also affect the reaction through complex formation either with the propagating radical or the monomer [48]. H-bonding interactions are shown to significantly modify the copoly-

merization kinetics. For instance, the observed solvent dependence of the propagation rate coefficient for ST/HEMA system in alcohols is explained by an implicit penultimate unit effect specific to H-bonding [52].

Under the penultimate model, there are four different types of radical ($-M_1M_2\bullet$, $-M_2M_2\bullet$, $-M_1M_1\bullet$, $-M_2M_1\bullet$) and thus eight different types of reaction that need to be characterized. Fukuda *et al.* [49] proposed a restricted form of the penultimate model, known as the implicit penultimate model (IPUM). In this model, it is assumed that the magnitude of the PUE on radical reactivity is independent of the coreactant and that there is thus no PUE on the selectivity of the radical. A consequence of this assumption is that the implicit PUE affects only the overall propagation rate of a copolymerization and not the composition or microstructure of the resulting polymers which can thus be fitted by the terminal model. The implicit penultimate model has been widely adopted [50], however the explicit penultimate model [47] in which the PUE is allowed to affect both the reactivity and selectivity of the radical has also been used. Details of the both models have been reported in a review by Coote *et al.* [53].

Coote *et al.* in their study for the addition of gamma-substituted propyl radicals to alkenes have demonstrated computationally that the magnitude of the penultimate unit effect is strongly dependent on the reacting alkene [54, 55]. The same group has studied the effect of substituents ($X = H, F, \text{ or } CN$) on the addition of 1-Y,3-X-disubstituted propyl radicals ($Y = F \text{ or } CN$) to ethylene and found out that the explicit rather than implicit penultimate model should provide a more physically realistic description of copolymerization kinetics [56]. Finally it was shown for para substituted styrenes that the explicit penultimate model provides a more physically realistic description of copolymerization kinetics than the implicit penultimate model [57]. The same group, in their study of the penultimate effect for the ATRP activation step has identified significant penultimate effects in the equilibrium constants between active and dormant species [58]. In the radical ring-opening copolymerization of 2-methylene 1,3-dioxepane and methyl methacrylate, Davis *et al.* claimed that the terminal and penultimate unit models for copolymerization could not adequately describe the experimental results [59]. The effect of solvent on the free-radical copolymerization has

been the subject of many investigations since the first demonstration of solvent effects on the radical polymerization of methyl methacrylate and styrene [60]. Among several explanations of solvent effects in radical copolymerization, the ‘bootstrap’ model as suggested by Harwood [61] proposes that the solvent does not affect the reactivity of the growing chain radical, but it affects the partitioning of the monomer between the free solvent and the growing chain radicals. As a result, by changing the monomer concentration in the feed (appears as the mole fraction of the monomer in the above copolymer equation), the solvent modifies the *copolymer composition*. Later, Klumperman and O’Driscoll [62] proposed a partition coefficient (K) as the ratio between the monomer concentration in the vicinity of the growing chain radicals (local concentration) and in the solution (global concentration), thus quantifying the partitioning phenomena described by Harwood.

Experimental studies of solvent effects on copolymerization kinetics involve measuring propagation rate coefficients via pulsed laser polymerization (PLP) technique [51, 63–69]. Solvent effect on the propagation of methacrylic acid (MAA) is studied with PLP and specific monomer-solvent interactions are investigated with FTIR spectroscopy [70]. Propagation rate constants of acrylic acid (AA) and MAA in water are significantly influenced by organic solvents and changing monomer concentrations [71]. Also, benzyl alcohol and N-methyl pyrrolidinone (NMP) as solvents influence MMA and ST homopolymerizations by changing the activation energies and preexponential factors [72]. Beuermann *et. al.* studied the radical polymerization of AA and MAA in aqueous solutions in several studies [73–77] and observed an increase in k_p with dilution of monomer concentration. Besides AA, MAA and acrylates, acrylamide (AAm) and N-isopropyl acrylamide (NIPAM) aqueous phase monomer concentrations, apparent k_p values in water decrease upon formation of dimers in water phase [78, 79]. Quantum-chemical calculations with the incorporation of solvation methods offer a fast and reliable approach to investigate the solvent effects on the kinetics of complicated systems [80–82]. Since experimental determination of reactivity ratios and kinetic parameters can sometimes be challenging particularly for complex systems, the results of quantum-chemical calculations can be useful in describing solvent effects on the copolymerization kinetics of many systems.

It is important to note that there have been several studies [83–87] including our recent work [88–91] on the theoretical modeling of free-radical polymerization and copolymerization kinetics by means of quantum-chemical approaches; however, the vast majority of these theoretical studies focus on the evaluation of kinetic parameters without incorporating solvent effects. Among few theoretical studies including solvent effects is the work by Thickett and Gilbert [92] where a simple Polarizable Continuum Model (PCM) [93, 94] was used to model the AA propagation kinetics; though, the method used in this study turned out to be insufficient for a quantitative description of the reaction rate. In a more recent study by Coote et al. [95], the use of Conductor-like Screening Model (COSMO) [96–99] resulted in a better agreement between theory and experimental rate parameters; yet, the systems under investigation (vinyl chloride and acrylonitrile) showed minor solvent dependence. In other systems, such as ethyl-hydroxymethacrylate (EHMA) that exhibit strong molecular interactions through H-bonding, the application of continuum solvation methods was insufficient for a quantitative description of the propagation rate coefficients presumably due to the neglect of H-bonding interactions in the continuum solvent models [100]. In a recent study by some of us, propagation rates of AA and MAA in bulk and in water are reproduced qualitatively; the rate acceleration in solution is reproduced by using both implicit/explicit solvation models and COSMO-RS calculations [101]. Also, for methyl acrylate (MA) and vinyl acetate (VA) propagations, the calculated reaction barriers reproduced the experimental findings to within 4 kJ/mol by correcting gas phase calculations to solution phase using free energies of solvation computed by COSMO-RS [102]. Therefore, in particular for systems that show strong solvent dependence through specific interactions with solvent, the propagating radical and/or monomers, the inclusion of explicit solvent molecules in the calculations should provide reliable rate parameters, as in one of our recent studies where explicit solvent plays an important role on the tacticity of the propagating chain and rate of the polymerization [91].

In this regard, we have performed quantum-chemical calculations to monitor solvent effects on the free-radical *copolymer composition* and *propagation rate coefficient* of ST with HEMA; polar aprotic *N,N*-dimethylformamide (DMF), and nonpolar toluene are used as solvents in the calculations. The choice of these solvents depends on the

experimental findings that both of these solvents have an impact on the copolymer composition (and monomer reactivity ratios) of ST/HEMA system [52].

4.1.2. Computational Procedure

The rate of a free-radical polymerization reaction is expressed as

$$R_p = -\frac{d[M]}{dt} = k_p \left(f \frac{k_d}{k_t} \right)^{0.5} [M] [I]^{0.5} \quad (4.11)$$

where k_p , k_d and k_t are the rate coefficients for the propagation, initiator decomposition and termination steps. f is the initiator efficiency, $[M]$ and $[I]$ are the concentrations of the monomer and initiator, respectively [103]. In this study, the effect of solvent on the homopolymerization of HEMA and ST, and on the copolymerization of ST/HEMA copolymer system have been investigated; the propagation steps have been modeled and their k_p values have been used to represent the homo- and copolymerization reactions.

The conventional transition state theory (TST) is used to calculate the rate constants. The rate constant of a bimolecular reaction $A + B \rightarrow C$ is expressed [104] in terms of the molecular Gibbs free energy difference between the activated complex and the reactants (with inclusion of zero point vibrational energies):

$$k_2 = \kappa \frac{kT}{h} \frac{RT}{p^\theta} e^{-\Delta G^\ddagger/RT} \quad (4.12)$$

where R represents the universal gas constant and κ is the transmission coefficient which is assumed to be about 1 and p^θ is the standard pressure 10^5 Pa (1 bar) [105].

To achieve the above-mentioned goal, the stationary points corresponding to the 3D structures along the reaction paths depicted in Figure 4.1 have been located with M06-2X/6-31+G(d,p) since this methodology [10] is recommended for thermochem-

istry, kinetics, and noncovalent interactions. A detailed conformation search has been carried out in each case and the structures corresponding to the global minima have been considered later for the evaluation of the energetics and kinetics. The structures of the most stable conformations of the reactants have been considered in generating the transition state structures, this is followed by a full conformer search around the critical bond, a 30 degrees rotation followed by optimization. The above mentioned procedure has been carried out both in bulk and in solution. Geometries in solution have been located with the Polarizable Continuum Model (PCM) [93,94] and solvation effects have been included with the COSMO-RS [96–99] methodology. In PCM calculations the dielectric of the medium in toluene has been taken as 2.4 whereas in DMF this has a value of 37.2. On the other hand, for the copolymerization in bulk where ST acts as a monomer, the medium has a dielectric of 2.4 -similar to toluene; when HEMA acts as a monomer, the bulk has been treated as a medium similar to HEMA with a dielectric of 7.6. (Note HEMA has a dielectric constant of 7.6 similar to one of THF). Consequently, for the homopolymerization of HEMA in bulk, the dielectric of the medium has been taken as 7.6 and, for the ST homopolymerization it has been considered as 2.4.

The Gaussian 09 program package [106] has been used for geometry optimizations, whereas single point COSMO calculations have been performed with ADF (Amsterdam Density Functional Theory) [107] package. Single point COSMO calculations in ADF using the BP/TZP level are performed to generate the cavity and surface charge densities in conducting medium. For the COSMO-RS calculations in bulk, the medium is considered to consist of the monomers themselves (i.e. ST if HEMA radical attacks ST or HEMA if ST radical attacks HEMA); the monomer concentration is assumed to be higher than that of the radical concentration during propagation. In these calculations, the solute is embedded in a molecule shaped cavity and its surface is polarized by the solvent molecules. Thus we assumed that during the polymerization reactions in bulk, the radical species are in contact with the monomers to which they are supposed to attack and the polarization of the surface of the solute is affected by the molecules which are closer to it. During the free-radical polymerization, the propagating radical may attack the double bond of the monomer to yield either the pro-*meso* or the pro-

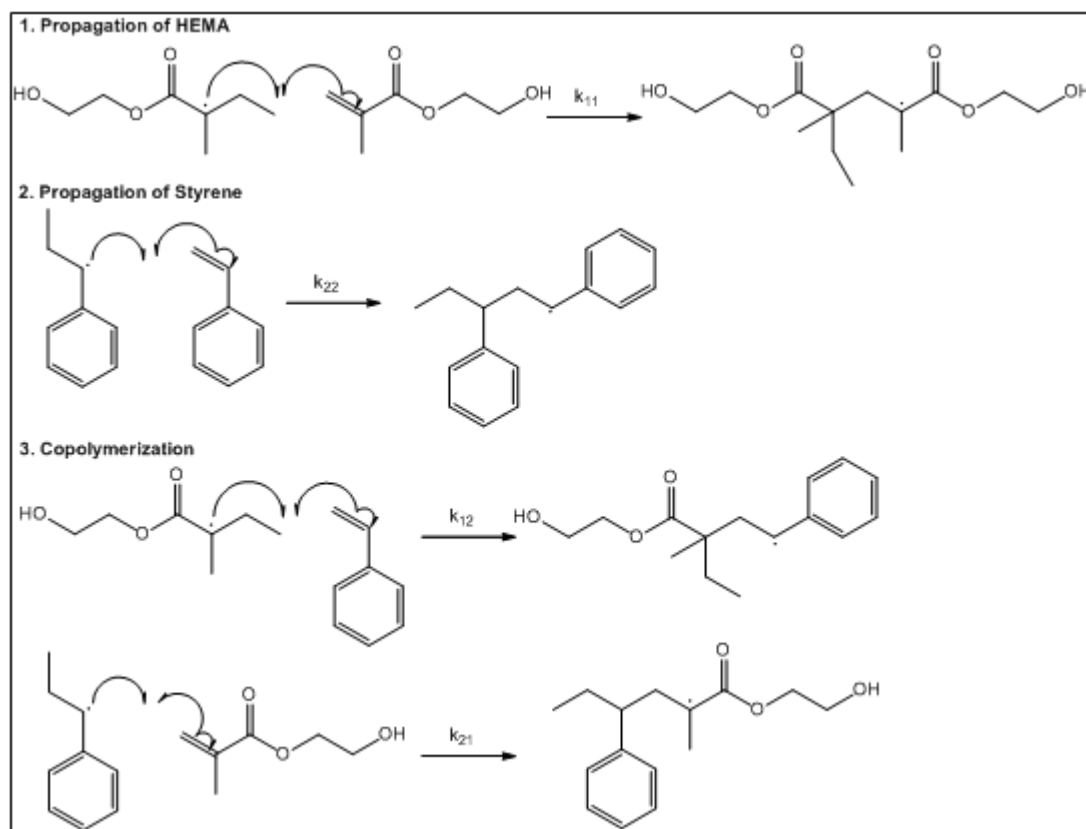


Figure 4.1. Homopolymerization and copolymerization of HEMA and styrene.

racemo dimeric radicals. The attack of a *syn* HEMA radical to a HEMA monomer during the propagation step is depicted in Figure 4.2. Radical species can attack the monomer from two directions: attack of the radical to the *s-cis* or *s-trans* monomer from the direction shown in the upper part is expected to yield the *pro-meso* dimeric radical products. However, for the attack from the lower part (shown with a line), *pro-racemo* dimeric radicals are obtained. Overall there are 4 possible ways for a *syn* HEMA radical to attack a HEMA monomer. Similarly there are four other possibilities for the attack of an *anti*-radical: overall 8 different transition state structures for the propagation step of HEMA during homopolymerization have been located (Figure 4.3 and Table 4.1). Note that in all media the structures corresponding to global minima have been considered (Figure 4.4) for further kinetic investigations.

In DMF, explicit solvent molecules have been included and the supermolecules are optimized in solution with the PCM methodology (implicit/explicit solvation model).

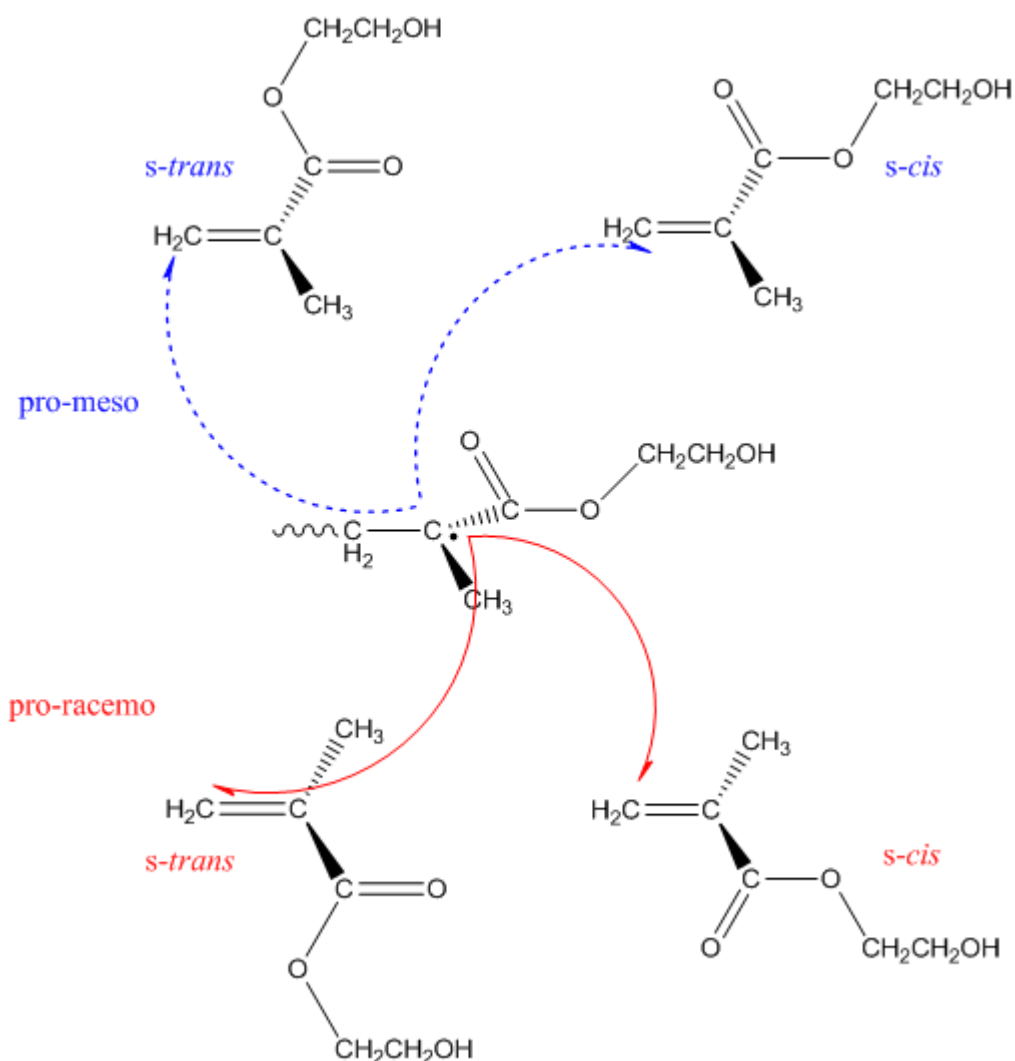


Figure 4.2. Stereoselective Radical (*syn*) Addition to HEMA (*s-cis* and *s-trans*).

The calculated free energy of solvation was corrected with the term $RT \ln$ (24.46) in order to take into account the unit transformation from $1 \text{ mol L}^{-1} (\text{g})$ to $1 \text{ mol L}^{-1} (\text{solution})$ [108]. Contribution of the solvent to the Gibbs free energy computed by COSMO-RS and thermal corrections from the methodology with which the structures are optimized is finally added to the electronic energy. (A sample calculation is displayed in Table 4.2 and Figure 4.4).

The mole fraction of monomer-1 in the copolymer (F_1) depends only on monomer mole fractions (f_1 and f_2 , with $f_1 + f_2 = 1$) and the monomer reactivity ratios can be calculated with the Mayo-Lewis equation [43] (Equation 4.5).

Table 4.1. Sum of electronic and thermal Gibbs Free Energies for the structures in Figure 4.3.

	Pro-meso	Pro-racemo
Mon-cis-Rad- <i>anti</i>	-959.8547126	-959.8539292
Mon-trans-Rad- <i>syn</i>	-959.8532521	-959.8553738
Mon-cis-Rad- <i>syn</i>	-959.8543982	-959.8545557
Mon-trans-Rad- <i>anti</i>	-959.8535183	-959.8529964

In the copolymerization reactions two alternatives have been considered: a HEMA radical attacking a ST monomer and a ST radical attacking a HEMA monomer. The effect of polar, nonpolar media as well as the copolymer composition on the copolymerization kinetics is investigated. After the calculation of homo- and copolymerization rate constants, the monomer reactivity ratios and copolymer compositions are estimated with Equations 4.6 and 4.7. Spin density calculations have also been used to rationalize our findings.

In this study, the terminal rather than the penultimate model has been used to understand qualitatively the role of the solvent on the copolymerization kinetics of the ST/HEMA system. The presence of explicit solvent molecules together with the increasing number of alternatives for the transition structures would render the calculations with the penultimate model too cumbersome to be of practical usage.

4.1.3. Results and Discussion

4.1.3.1. 3D Structures. The most stable transition state structures for the homopropagation of HEMA in bulk, toluene, and DMF are depicted in Figure 4.5. In bulk and in toluene, intramolecular H-bonding interactions to form 7-membered rings between the hydroxyl proton and carbonyl oxygen have been observed in both moieties of the transition structures; these structures resemble each other. The transition structure in toluene has a lower dipole moment (8.345 D) as compared to the one in bulk (9.152 D) and also the charge separation between the carbonyl oxygen and the methyl proton in HEMA in toluene stabilizes this transition state more than the one in the bulk.

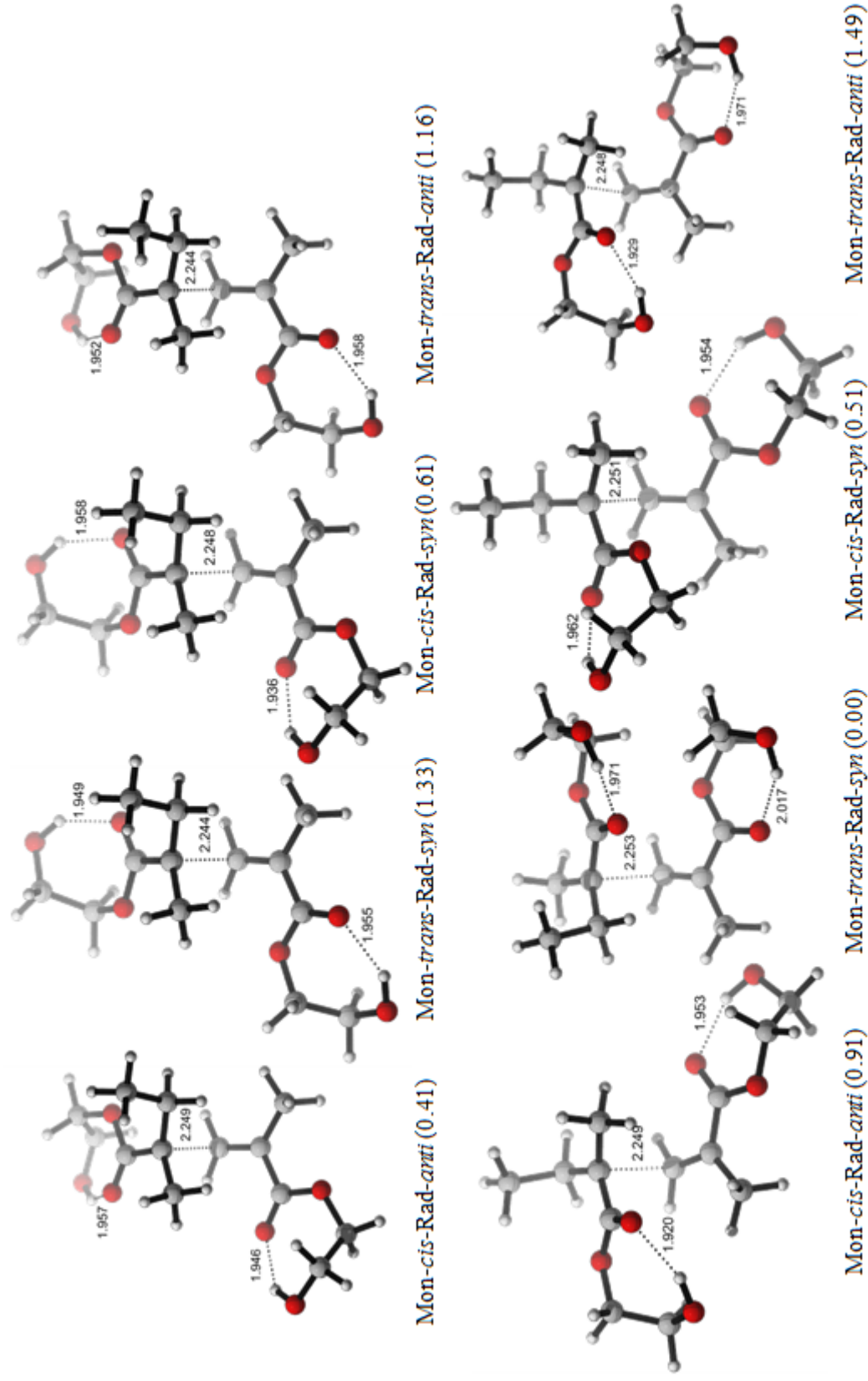


Figure 4.3. Gas phase optimized geometries of a) Pro-*meso* and b) Pro-*racemo* transition states with M06-2X/6-31+G(d,p) methodology (Relative Gibbs Free Energies (kcal/mol) are in parenthesis).

Table 4.2. Parameters for sample calculation in toluene for HEMA-HEMA Homopolymerization (M06-2X/6-31+G(d,p)).

T=298.15 K	HF Energy in PCM	Thermal correction to Gibbs Free Energy in PCM (Hartree/Particle)	Zero point Correction in PCM (Hartree/Particle)	COSMORS $\Delta\Delta G$ (kcal/mol)	Bimolecular Correction (RTln(24.5)) (kcal/mol)
HEMA monomer	-460.1478923	0.123553	0.159206	-6.85231894	
HEMA radical	-500.0206983	0.158193	0.197557	-7.88562909	1.9
HEMA-HEMA-Toluene (TS)	-960.1691186	0.305711	0.358383	-14.31466402	

$$\begin{aligned}
 \Delta G^\ddagger \left(\frac{\text{kcal}}{\text{mol}} \right) &= ((\text{HF Energy in PCM} + \text{Thermal correction to Gibbs Free Energy in PCM})_{\text{HEMA-HEMA-Toluene}} - (\text{HF Energy in PCM} \\
 &+ \text{Thermal correction to Gibbs Free Energy in PCM})_{\text{HEMA monomer}} \\
 &- (\text{HF Energy in PCM} + \text{Thermal correction to Gibbs Free Energy in PCM})_{\text{HEMA radical}}) * 627.51 \\
 &+ (\text{COSMORS } \Delta\Delta G)_{\text{HEMA-HEMA-Toluene}} - (\text{COSMORS } \Delta\Delta G)_{\text{HEMA monomer}} - (\text{COSMORS } \Delta\Delta G)_{\text{HEMA radical}} - \text{RTln}(24.5) \\
 &= ((-960.1691186 + 0.305711) - (-460.1478923 + 0.123553) - (-500.0206983 + 0.158193)) * 627.51 \\
 &+ (-14.31466402) - 6.85231894 - (-7.88562909) - 1.9 = 13.23 \\
 E_a \left(\frac{\text{kcal}}{\text{mol}} \right) &= ((\text{HF Energy in PCM} + \text{Zero point Correction in PCM})_{\text{HEMA-HEMA-Toluene}} \\
 &- (\text{HF Energy in PCM} + \text{Zero point Correction in PCM})_{\text{HEMA monomer}} \\
 &- (\text{HF Energy in PCM} + \text{Zero point Correction in PCM})_{\text{HEMA radical}}) * 627.51 = 0.69k_p (\text{L} \cdot \text{mol}^{-1} \cdot \text{s}^{-1}) = \kappa \frac{kT}{h} \frac{RT}{p} e^{-\Delta G^\ddagger / RT} \\
 &= \frac{1.38066 * 10^{-23} * 298.15}{6.62608 * 10^{-34}} * \frac{8.3145 * 298.15}{101035} * e^{\frac{-13.23 * 4.184 * 1000}{8.3145 * 298.15}} = 30.6 \\
 A (\text{L} \cdot \text{mol}^{-1} \cdot \text{s}^{-1}) &= \frac{k_p}{e^{-E_a / RT}} = \frac{30.6}{e^{1986 * 298.15}} = 97
 \end{aligned}$$

Figure 4.4. Sample calculation in toluene for HEMA-HEMA homopolymerization.

The intramolecular interactions are ruptured with the inclusion of explicit DMF molecules in the system: the hydroxyl proton prefers to form H-bonds with the amide oxygen of the solvent. A weak interaction between the carbonyl oxygen and the amide proton stabilizes this structure as well.

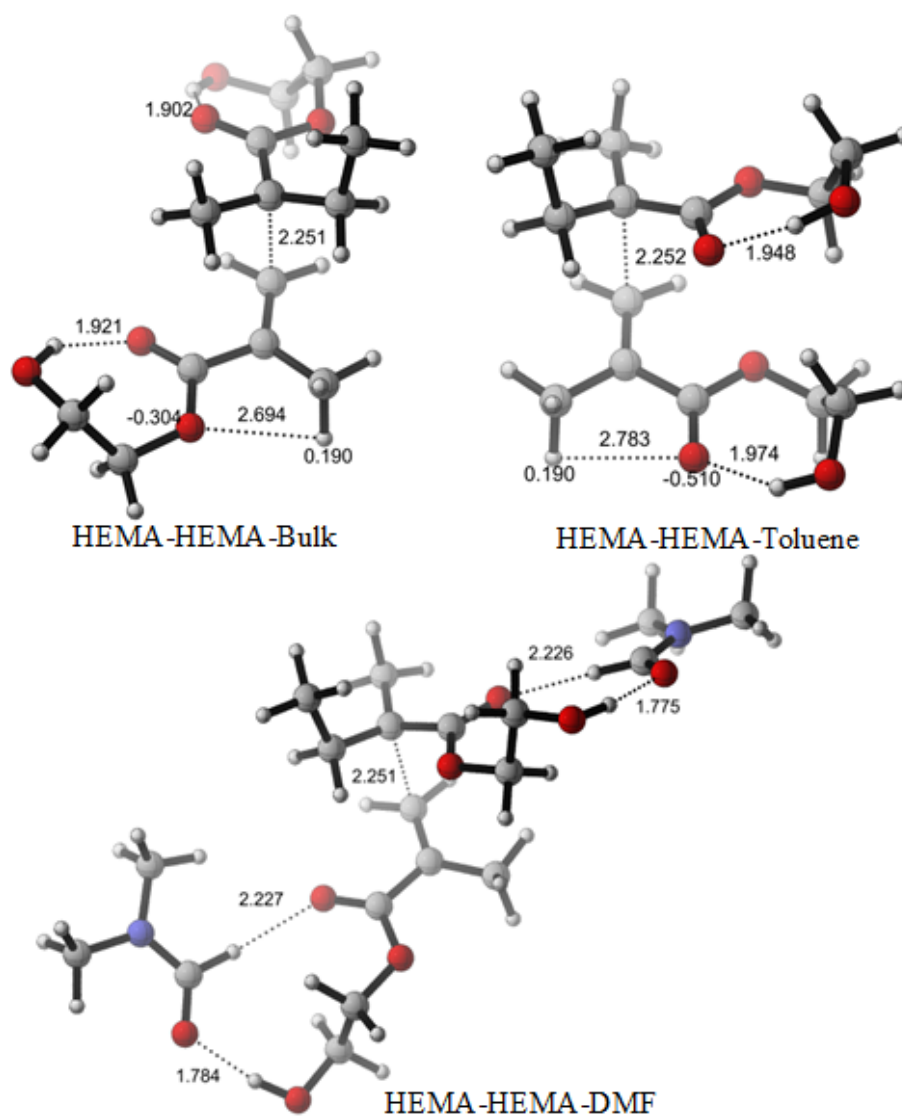


Figure 4.5. Propagation transition states of HEMA (M06-2X/6-31+G(d,p)).

In the case of styrene (Figure 4.6), the transition state structures are similar in bulk and in solution: the two aromatic rings are close to each other due to C-H- π interactions, known to be important non-covalent interactions between benzene and heterocycles, especially in biomolecular systems or between 2 benzene rings [109, 110]. The critical bond distance in bulk ($d=2.260$ Å) is longer as compared to the one in

DMF ($d=2.255 \text{ \AA}$), thus an early transition state, and faster propagation is expected in bulk. In DMF, as the polarity of the medium increases, the critical bond distance shortens. In bulk medium, the reactants combine easily to yield a transition structure, however in polar medium the forming critical bond is screened by the continuum: as the polarity of the solvent increases, reactants are more shielded by the solvent and transition structures form later.

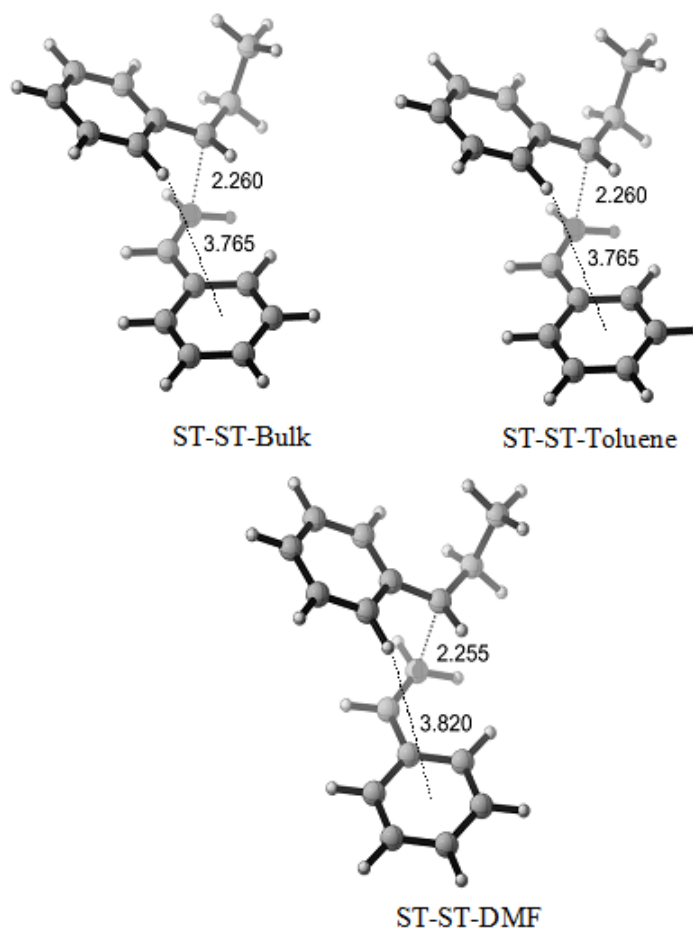


Figure 4.6. Propagation transition states of ST (M06-2X/6-31+G(d,p)).

For copolymerization reactions, both cases where ST radical attacks to a HEMA monomer and HEMA radical attacks to a ST monomer have been considered. The most stable copolymerization transition states are depicted in Figure 4.7. In bulk and in toluene the transition structures are similar, whereas in DMF, the intramolecular H-bonds are replaced by interactions with solvent molecules. In DMF, the number of intermolecular H-bonding interactions increases because of the explicit solvent molecules

in the vicinity, thereby decreasing the disorder in the system. Thus, the entropy of activation decreases and slower propagation is anticipated in DMF.

4.1.3.2. Kinetics. The transition structures for homopolymerization and copolymerization look very much alike in bulk and in toluene. In DMF, explicit solvent molecules provide more ordered structures, except in the case of ST-HEMA(R)-DMF case. In this transition structure, the unbridged DMF molecule increases the disorder, thereby having higher pre-exponential factor. In solution if the reactants are more stabilized than the transition state, the Gibbs free energy of activation increases, however, if the reverse happens, the barrier decreases and accelerates the propagation reaction (Figure 4.8). For example in DMF, all the propagation rate constants decrease as compared to the ones in bulk and toluene; in cases where HEMA is present, intramolecular H-bonding interactions are disturbed, intermolecular H-bonds stabilize the species. In the homopolymerization of HEMA, DMF stabilizes the reactants by 3.74 kcal/mol, and the transition state by 3.29 kcal/mol, the reactants are stabilized more than the transition structure as displayed by the Gibbs free energy profile (Figure 4.8b). The rate deceleration in DMF compared to toluene can be attributed to the relative stabilization of the reactants in the two media: in toluene, HEMA and HEMA(R) are destabilized by 2.18 and 2.17 kcal/mol, whereas in DMF due to the stabilizing H-bonding interactions HEMA and HEMA(R) are stabilized by 1.73 and 2.00 kcal/mol respectively. For ST and ST(R) the stabilization energies are 0.06 kcal/mol and 0.09 kcal/mol in toluene and 1.72 kcal/mol and 1.45 kcal/mol in DMF, respectively, these small differences are reflected in the values of the rate constants. Furthermore, in the homopolymerization of HEMA, toluene destabilizes the reactants by 4.35 kcal/mol, while it destabilizes the transition state by 3.55 kcal/mol indicating that in a nonpolar medium, the activation energy barrier is lower due to the larger destabilization of the reactants. In cases where H-bonds are not present (ST-ST-DMF) the dielectric of the polar medium decelerates the reaction. (Activation barriers and stabilization energies for the gas phase geometries are provided in Table 4.3).

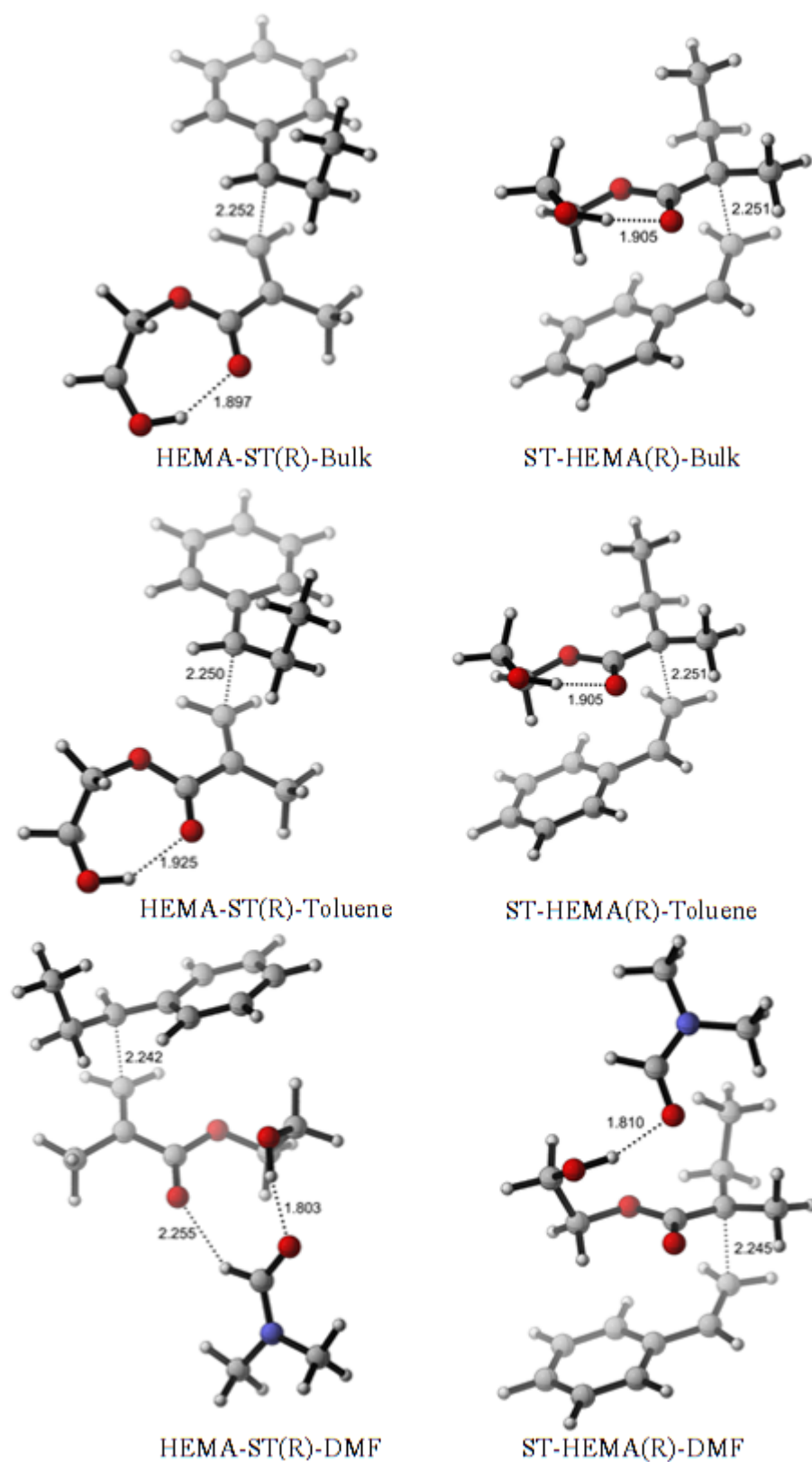


Figure 4.7. Copolymerization transition states of ST/HEMA copolymer system (M06-2X/6-31+G(d,p)).

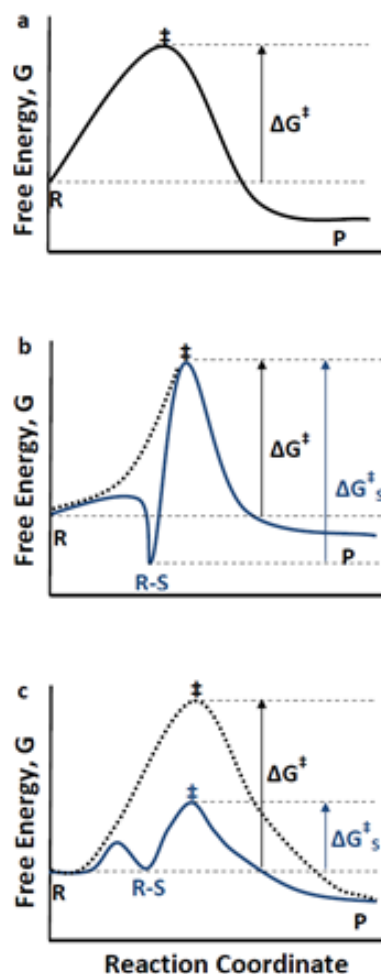


Figure 4.8. Copolymerization Gibbs free energy profiles for the propagation reactions when a) there is no solvent, b) when the reactants are stabilized and, c) when the transition state is stabilized by solvent molecules (R: Reactant, R-S: Reactant-Solvent complex and P: Product).

As displayed in Table 4.4, ordered transition structures have low pre-exponential factors and entropies of activation due to stronger inter or intramolecular interactions. Note that, in the homopolymerization of ST, the pre-exponential factors are higher as compared to the ones in homopolymerization of HEMA: this can be attributed to the weak interactions between the ST rings increasing the disorder of the system as opposed to HEMA-HEMA(R) where the transition structures are more ordered due to the presence of intramolecular H-bonding interactions.

Table 4.3. Gas phase standard (at 298 K), activation barriers (kcal/mol) and stabilization energies (kcal/mol) (M06-2X/6-31+G(d,p)).

	Stabilization Energy in DMF	Stabilization Energy in Toluene	E_a
HEMA monomer	-9.24	-2.69	
HEMA radical	-9.46	-2.90	
ST monomer	-3.17	-1.51	
ST radical	-2.48	-1.12	
HEMA-HEMA homopropagation	-20.56	-4.85	2.35
ST-ST homopropagation	-3.77	-1.60	3.97
HEMA-ST(R) copolymerization	-10.44	-3.75	2.96
ST-HEMA(R) copolymerization	-15.21	-3.39	0.47

The monomer reactivity ratios are in good qualitative agreement with the experimental values, except for r_{HEMA} in toluene. In toluene, r_{HEMA} is greater than 1, indicating that in a nonpolar medium, homopolymerization of HEMA is preferred over copolymerization as mentioned earlier. The deviation from experiment in toluene may be due to the overestimation of the homopolymerization rate constant due to the presence of regular intramolecular interactions which in reality may be somewhat ruptured. On the other hand, r_{ST} values indicate that for ST, copolymerization reactions are faster than homopolymerization in all media.

The propagation rate constants for the homopolymerization reactions reveal the fact that even though the calculated values are not in quantitative agreement with experiment, they depict the experimental trend qualitatively pretty well (Table 4.4). In both cases (ST and HEMA), polymerization in polar medium is slower compared to bulk and nonpolar medium. In ST-ST case, rate constants in bulk and toluene increase almost to the same extent as compared to the one in DMF. In toluene, for the HEMA-HEMA homopolymerization, the deviation from experiment maybe attributed to the overestimation of the propagation rate constant in this medium as mentioned earlier. The discrepancies between experimental and calculated values may also be due to the simplicity of the models used. A thorough conformer search in a longer polymeric chain followed by inclusion of the penultimate effects might lead to quantitative agreement with experimental values.

Table 4.4. Activation energy barriers E_a (kcal/mol), Gibbs free energies of activation ΔG^\ddagger (kcal/mol), propagation rate constants k_p (L/mol.s), pre-exponential factors A (L/mol.s), monomer reactivity ratios and relative propagation rate constants (Experimental values [52] are in parenthesis) at 298.15 K.

	HEMA-HEMA	ST-ST	HEMA-ST(R)	ST-HEMA(R)
Bulk				
E_a	2.91	4.44	3.25	1.04
ΔG^\ddagger	14.04	14.43	12.63	13.79
k_p	7.81E+00	4.05E+00	8.46E+01	1.19E+01
A	1064	7291	20595	69
k_{pBulk}/k_{pDMF}	2.1 (1.7)	4.7 (1.3)		
r_{HEMA}	0.65 (0.49)			
r_{ST}	0.05 (0.27)			
DMF				
E_a	1.89	4.96	3.37	2.11
ΔG^\ddagger	14.47	15.35	14.35	13.79
k_p	3.78E+00	8.59E-01	4.63E+00	1.18E+01
A	91	3759	1370	418
k_{pDMF}/k_{pDMF}	1.0 (1.0)*	1.0 (1.0)**		
r_{HEMA}	0.32 (0.53)			
r_{ST}	0.19 (0.45)			
Toluene				
E_a	0.69	4.44	3.13	1.04
ΔG^\ddagger	13.23	14.49	12.55	13.83
k_p	3.06E+01	3.66E+00	9.63E+01	1.10E+01
A	97	6591	18963	64
$k_{pToluene}/k_{pDMF}$	8.1 (1.7)	4.3 (1.3)		
r_{HEMA}	2.77 (1.09)			
r_{ST}	0.04 (0.23)			

* $k_{pDMF}(HEMA - HEMA)$: 3763 L/mol.s

** $k_{pDMF}(ST - ST)$: 691 L/mol.s

The calculated and experimental monomer reactivity ratios in Table 4.4 have been used in the Mayo-Lewis equation to deduce the copolymer composition data for the ST/HEMA copolymer system (Figure 4.9). In DMF, the HEMA monomer fraction in the copolymer is lower than the one in toluene since in DMF, HEMA interacts with the solvent and the local monomer concentration around the ST radical decreases. As the HEMA fraction in solution increases, the local HEMA monomer concentration around radical species increases and the mole fraction in the copolymer increases. The mole fractions of HEMA in the copolymer (FHEMA) increases and become closer to

the experimental values as the f_{HEMA} increases. In toluene, the higher deviation from experiment may be attributed to the higher monomer reactivity ratio (r_{HEMA}) in this medium as compared to the ones in bulk and DMF.

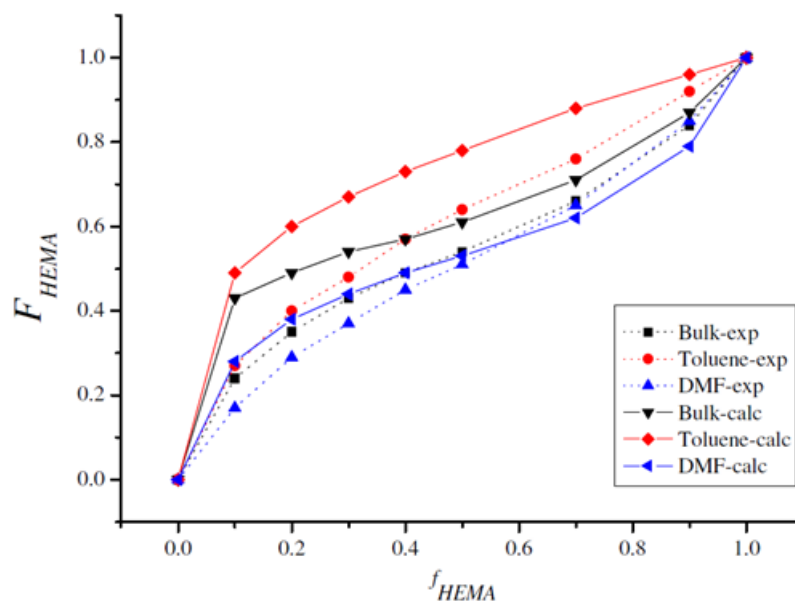
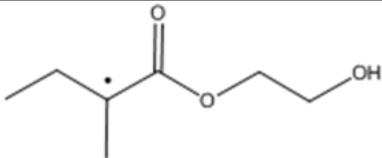
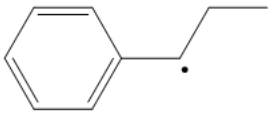


Figure 4.9. Copolymer composition data for ST/HEMA system, mole fraction of HEMA in the copolymer (F_{HEMA}) as a function of HEMA mole fraction in solution (f_{HEMA}) (M06-2X/6-31+G(d,p)).

Mulliken atomic spin densities on the radicalic carbon atoms of HEMA and ST radicals are given in Table 4.5. The radicals have the lowest spin densities in DMF, thus the lowest rate constants in polar medium (Table 4.4) can be attributed to the lower reactivity of the radical species in this medium. The spin densities are higher in bulk and toluene where the calculated values for propagation rate constants are higher. In all media, the ST radical bears the highest spin density, in bulk and in toluene the copolymerization reaction where the ST radical attacks the HEMA monomer (HEMA-ST(R)) is favored over the attack of the HEMA radical on the styrene monomer (HEMA(R)-ST) (Table 4.4). However in DMF due to the presence of explicit solvent molecules around HEMA, the attack by the ST radicals is inhibited. On the other hand, HEMA will easily attack the free ST monomers as demonstrated by the calculations.

Table 4.5. Mulliken atomic spin densities (M06-2X/6-31+G(d,p)) for the radicalic carbon atoms of HEMA and ST radicals.

	Bulk	DMF	Toluene
	0.815	0.802*	0.825
	0.885	0.882	0.885

* In the presence of explicit DMF.

4.1.4. Conclusions

By performing quantum-mechanical calculations on the solvent effects of the ST/HEMA homo- and copolymerization kinetics, we find that noncovalent interactions like H-bonding within the monomers or with the solvent are the key to understand the solvent dependence of polymerization reaction. The intramolecular H-bonding interactions within HEMA molecules in bulk and nonpolar media are replaced with intermolecular H-bonding interactions between HEMA and polar solvent (DMF). Interestingly, this gives rise to a pronounced rate reduction in the polymerization of ST/HEMA system in the DMF solution. Variations in the propagation rate in different media affect the monomer reactivity ratios, which in turn affect the copolymer composition. In agreement with the pronounced rate reduction of ST/HEMA system in DMF, the HEMA fraction in the copolymer is found to be low in this media as compared to the other cases (bulk and toluene environment). Spin density calculations of the radical species further support the calculated and measured rate parameters.

In summary, the change in the polymerization environment (bulk, nonpolar, polar) does affect the free-radical polymerization kinetics of ST/HEMA system; this effect is more pronounced when there are specific interactions like H-bonding between the monomers and solvents. This study qualitatively describes the solvent dependence of free-radical polymerization kinetics of ST/HEMA system through a combination of

quantum-mechanical tools with the incorporation of solvation methods and we believe it provides a fast and reliable method for the study of solvent effects in the free-radical homo- and copolymerization kinetics. Longer polymeric chain where penultimate effects are considered may reproduce quantitatively the experimental findings provided that the conformational space for all the possible modes of attack is carefully explored.

4.2. Effect of Catalysts on the Stereoregularity of Dimethyl Acrylamide

In this study, the effect of Lewis acid coordination (ScCl_3) in controlling the stereoregularity during the free radical polymerization of *N,N*-dimethyl acrylamide (DMAM) has been investigated by Density Functional Theory (DFT). Experimentally, ScCl_3 , $\text{Sc}(\text{OTf})_3$ and $\text{Yb}(\text{OTf})_3$ have been used to increase the isotactic percentage in the polymerization of another acrylamide derivative, *N*-isopropyl acrylamide (NIPAM) (Habaue, S., Isobe, Y., Okamoto, Y., Tetrahedron, 2002, 58, 8205). The relative orientation of the terminal and penultimate side chains is expected to determine the stereoregularity in free radical polymerization reactions (Noble, B. B., Smith, L. M., Coote, M. L., Polym Chem, 2014, 5,4974). We have analysed the mechanistic details of the propagation reaction by considering all coordination types of the Lewis acid to the propagating species. Calculations have shown the bridging of the Lewis acid between the terminal side chain and the monomer to be the most probable pathway, which is in favour of the *pro-meso* propagation during the free radical polymerization of DMAM. In this case, it is the bridging capacity of the catalyst along the less crowded direction that dictates the preference for isotacticity. Overall, the strategy suggested in this study can be easily used by experimentalists in their endeavour of choosing the catalysts in order to end-up with the desired stereoregulation of the polymer chain.

4.2.1. Introduction

Living/controlled radical polymerization has gained great attention because the control of highly active radical species is very difficult, since they undergo very fast propagation and termination steps and generate dead chains [111]. However, well-defined polymers with controlled molecular weights can be obtained with living/control-

led radical polymerization [112]. The tacticity of the growing chain should also be controlled during the free radical polymerization since it affects the physical properties of the final product. For instance, crystallinity leads to high physical strength and to an increased solvent and chemical resistance and is significantly affected by stereoregularity of the polymer chain. While *atactic* polymers are amorphous (noncrystalline), the corresponding *isotactic* and *syndiotactic* polymers are usually highly crystalline materials [113]. The glass transition temperature, T_g , [114–116] the association behavior [117], and the chain conformation [118] are affected by the tacticity of the growing chain. It was also observed that the tacticity influences the hydrophobicity, and thus the phase transition behavior, of poly (*N*-isopropylacrylamide) (PNIPAM). The hydrophobicity has been observed to increase as the *meso* content increases [119–121].

Many attempts to produce stereospecific or stereoregular polymers have been made in confined media, such as the solid state, inclusion compounds, porous materials, and templates [122]. In solution polymerization, it is more difficult to provide a stereospecific environment around the growing radical center, because the monomer and the growing radical species move freely and diffuse in the reaction media. Therefore, vinyl monomers usually produce polymers with an inherent tacticity specific to their chemical structures. In view of production cost, solvent or additive-mediated systems might be the most promising solutions to obtain stereospecific polymers.

Lewis acids have been widely used in the regulation of tacticity in the polymerization reactions over the last few decades. In 1963, Imoto *et. al.* [123, 124] reported the acceleration of the polymerization and copolymerization of methylmethacrylate (MMA) in the presence of zinc chloride (ZnCl_2), but no stereoregularity was obtained at the concentrations used. However, in 1966 Otsu *et. al.* investigated the slight increase in the isotacticity of poly (MMA) with high concentrations of ZnCl_2 [125]. Magnesium bromide (MgBr_2), which has a poor solubility, is used as Lewis acid in the polymerization of MMA. A bidentate complex between the carbonyl oxygens of the propagating chain and the solid surface of the catalyst is reported to form [126]. In this study, as the amount of soluble MgBr_2 increases, the syndiotactic stereospecificity increases, whereas with the solid Lewis acid, isotacticity is preferred. In the radical

polymerization of -alkoxymethacrylates, zinc bromide (ZnBr_2) increases the syndiotacticity. On the other hand, around 70% isotacticity is obtained in the presence of scandium (III) triflate ($\text{Sc}(\text{OTf})_3$, $\text{OTf} = \text{CF}_3\text{SO}_3^-$) in the same polymerization. Isobe *et al.* [127] have gained great success in obtaining isotactic products in the polymerization of methacrylates by using $\text{Sc}(\text{OTf})_3$ among various metal triflates [128]. In the atom transfer radical polymerization (ATRP) of acrylamide, the Lewis acids yttrium (III) triflate ($\text{Y}(\text{OTf})_3$) and aluminium chloride (AlCl_3) have led to increased isotacticity with increased polymerization rate [129]. Okamoto and coworkers have carried out a stereocontrolled radical polymerization of acrylamides; the isotactic specific radical polymerization of various acrylamides [130, 131] and methacrylamides [132, 133] was achieved in the presence of a catalytic amount of Lewis acids such as $\text{Y}(\text{OTf})_3$ and ytterbium (III) triflate ($\text{Yb}(\text{OTf})_3$). Methacrylamides and their N-monosubstituted derivatives can be polymerized only by the free radical method because of the acidic amide proton; thus the development of an effective and facile stereocontrol method is very important. In the living anionic propagation of *N,N*-dimethyl acrylamide (DMAM), the effect of triethylaluminum (Et_3Al) on the relative stabilities of chain end structures with different tacticities has been investigated by Density Functional Theory (DFT) calculations where complexation of Lewis acid with monomer leads to its activation [134]. Experimentally, the interaction between the monomer and Lewis acids was investigated as the basis of stereocontrol in favor of isotactic specificity in the radical polymerization of (S)-*N*-(2-hydroxy-1-phenylethyl) methacrylamide ((S)-HPEMA) [135]. Recently, the dual role of some alkali metal salts such as lithium bis(trifluoromethanesulfonyl)imide (LiNTf_2) in the radical polymerization of DMAM has been investigated experimentally and computationally; in this study Li^+ was stabilizing the propagating radical species and also activating the incoming monomer [136].

Acrylamides are very important monomers and are used in daily life in pesticide formulations, cosmetics and packaging. DMAM, has been recognized as a co-monomer for the conformational control of polypeptides, as well as an anti-aging agent [137, 138]. DMAM was also used as a co-monomer for pH-responsive photoluminescent polymer [139] and as a non-thermoresponsive reference co-monomer [140].

Table 4.6. Experimental findings for stereocontrol in the presence of Lewis acids in methanol [131].

Monomer	Lewis acid	Tacticity (m/r)
NIPAM	-	45/55
NIPAM	Sc(OTf) ₃	62/38
NIPAM	ScCl ₃	57/43
NIPAM	Yb(OTf) ₃	82/18
DMAM	-	46/54
DMAM	Yb(OTf) ₃	84/16

Habaue *et. al.* reported the effect of various Lewis acids on the stereochemical control during the radical polymerizations of some acrylamides and methacrylamides (Table 4.6) [131]. In the absence of a Lewis acid, both monomers in the table yield slightly syndiotactic polymers. However, in the presence of Lewis acids, isospecificity increases. Although the rare earth metal chloride ScCl₃ was slightly less effective than its triflate salt in enhancing the isotactic products, ScCl₃ is used in this study since it will decrease the computational cost.

This study aims to examine the control of stereoregulation by Lewis acids during the free radical polymerization of DMAM making use of computational tools. Our previous studies on modeling the tacticity of N-isopropylacrylamide (NIPAM) and MMA in H-bonding solvents have given a solid basis for modeling free radical polymerization in a complex molecular environment [91,141]. In this paper we go beyond the standard protocol for modeling the stereoregularity in a free radical polymerization process by including a Lewis acid and examine the terminal and penultimate unit coordination effects.

The relative orientation of the terminal and penultimate side chains is expected to determine the stereoregularity in the free radical polymerization reaction. The *meso* and *racemo* propagation of DMAM in the absence and the presence of ScCl₃ is depicted in Figure 4.10. In part 1, where no acid is present in the medium, the probability of having both *meso* and *racemo* propagation should be equal since the radicalic chain end and the incoming monomer are free to rotate. In the presence of Lewis acid, more than

one way of coordination is possible. Coordination with the terminal and the penultimate units (Figure 4.10, part 2) is proposed as the isotactic regulating route [126,142]. However, the reaction in part 3 of Figure 4.10 can also provide stereoregulation since in this case the Lewis acid interacts with both the terminal side-chain and the incoming monomer. It is also possible that the catalyst only interacts with the terminal group (Figure 4.10, part 4); this type of complexation is not expected to assist stereoregulation. Herein we will investigate each of these possibilities to unravel the molecular origin of the observed stereoselectivity.

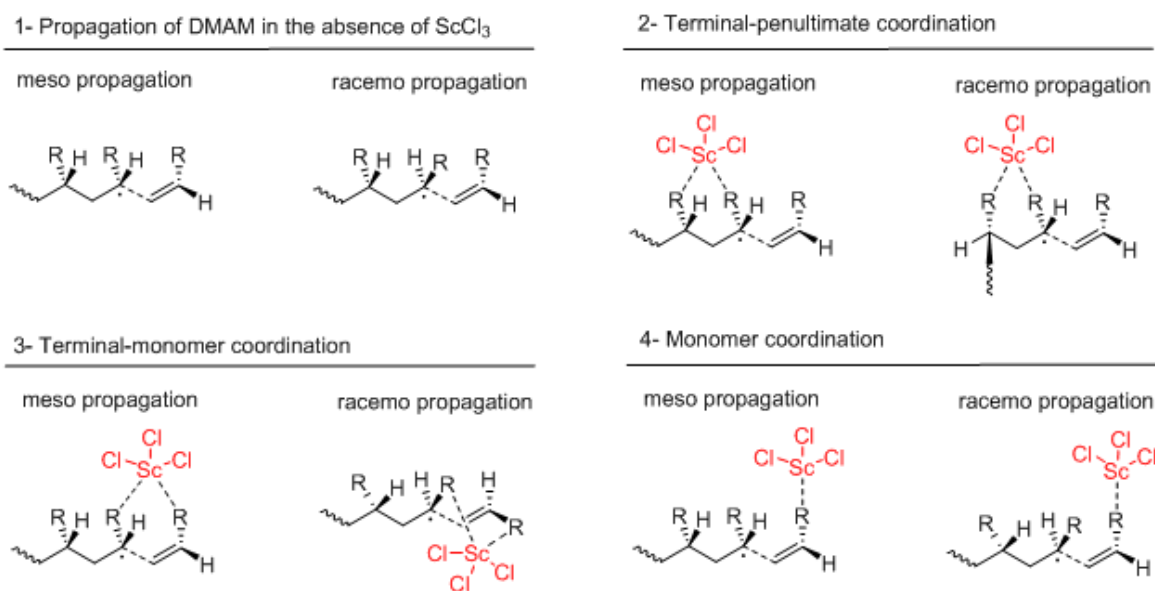


Figure 4.10. Stereoselectivity during radical polymerization of DMAM in the absence (1) and the presence (2-4) of ScCl_3 as Lewis acid.

4.2.2. Computational Procedure

In order to understand the role of Lewis acids in controlling the stereoregularity in the propagation of DMAM, structures along the reaction paths depicted in Figure 4.10 have been constructed, and optimized with M06-2X/6-311+G(d,p) since this functional is recommended for thermochemistry, kinetics, and description of noncovalent interactions [10]. Recently, this functional has been used successfully to calculate the activation energy of MMA homopropagation [143]. All geometry optimizations have

been performed in methanol with the Polarizable Continuum Model (PCM) [93, 94]. For each stationary point a conformational search has been carried out with the same methodology. The calculated free energy of solvation was corrected with the term $RT \ln 24.46$ in order to take into account the unit transformation from $1 \text{ mol L}^{-1} (\text{g})$ to $1 \text{ mol L}^{-1} (\text{solution})$ [108]. The Gaussian 09 program package [106] has been used throughout the study. The Gibbs free energy barriers of the propagation steps were calculated as the Gibbs free energy difference of transition states and the separated reactants in the absence of Lewis acid coordination. The same strategy has been used for the terminal-penultimate model propagation where the separated reactants are the dimeric radical complexed with the Lewis acid and the monomer itself. In the terminal-monomer type of propagation the Gibbs free energy barriers were calculated as the Gibbs free energy difference of transition states and the most stable pre-reactive complexes. Finally, the Gibbs stabilization energies of the complexes were calculated as the differences of the Gibbs free energies between the propagating radical complex with the Lewis acid (dimer or trimer), the propagating radical (dimer or trimer) and the Lewis acid.

In the free radical polymerization, the relative orientation of the terminal and the penultimate side-chains of the polymer terminus determines the stereochemistry. Thus, the direction of approach of the incoming monomer to the pro-chiral center is important. In this paper, we want to model all possible coordination modes of the Lewis acid to the propagating species as schematically depicted in Figure 4.10. Since the system may be subjected to a lot of attack modes and conformational changes, we first performed an in depth analysis of the propagation step in the absence of the Lewis acid. At second instance, ScCl_3 is systematically added to the system. The propagating radical may attack the double bond of the monomer to yield either the *pro-meso* or the *pro-racemo* radical chains. The attack of *syn*- and *anti*-DMAM radicals to *s-cis* and *s-trans* DMAM monomers during the propagation step is depicted in Figure 4.11. A *syn*-DMAM radical, can approach the DMAM monomer from 4 different directions. Similarly, there are 4 possible ways for an *anti*-DMAM radical to attack a monomer. Overall, 8 different transition states displayed in Figure 4.11 have been located for the dimeric propagation step (Part A in Figure 4.12) of the DMAM polymerization. This

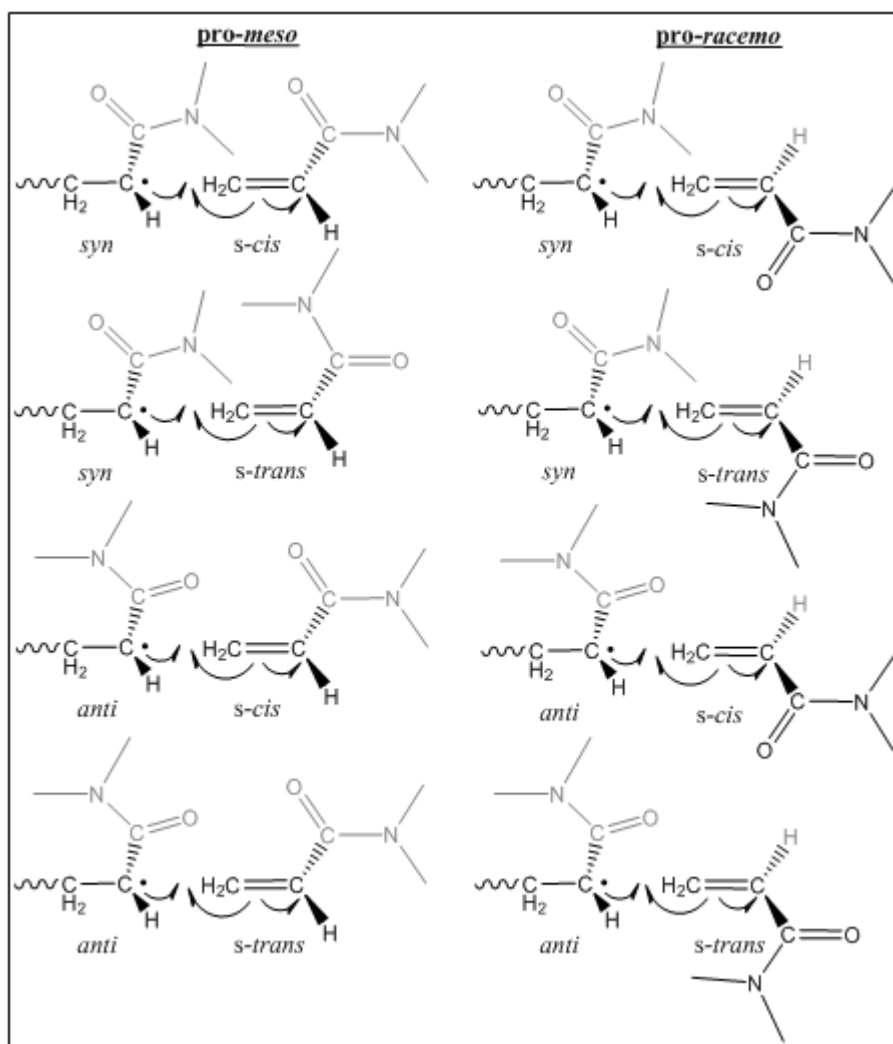


Figure 4.11. Stereoselective radical (*syn* and *anti*) addition to DMAM (*s-cis* and *s-trans*).

is followed by a full conformational search around the forming bond. The stationary points located in this manner were used for further analysis. IRC calculations [144,145] were carried out in order to justify the nature of the transition states. Dimeric radicalic chains obtained from the IRC calculations were used in modeling the next step of the propagation (Part B in Figure 4.12) where a dimeric radical attacks the incoming monomer. After locating the global minima and their corresponding transition states for the first and the second propagation steps, the Lewis acid coordination scenarios depicted in Figure 4.10 have been investigated. Dimeric and trimeric radicalic chains obtained from the IRC calculations are shown in Figure 4.16 and Figure 4.17.

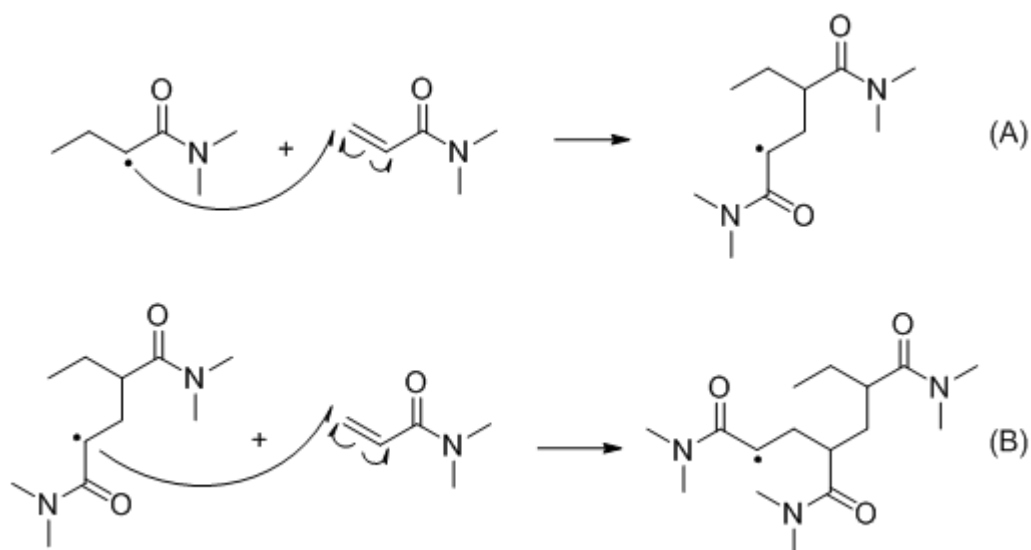


Figure 4.12. First (A) and second (B) propagation steps for the polymerization of DMAM.

4.2.3. Results and Discussion

4.2.3.1. Unimeric reactants. The conformational study in methanol revealed that the *s-cis* conformation for DMAM monomer and the *syn* conformation of DMAM radical are preferred over *s-trans* and *anti* conformations of the monomer and the radical by 2.05 and 3.12 kcal mol⁻¹, respectively (Figure 4.13). Similarly, in the previous computational studies on the radical polymerization of acrylamide (AM), methacrylamide (MAM) [146], and *N*-isopropylacrylamide (NIPAM) [91], the *s-cis* monomer and the *syn*-radical were more stable than their *s-trans* and *anti* counterparts.

In the presence of the Lewis acid the optimized structures of all conformations of both the monomer and radical are displayed in Figure 4.13. The reactant complexes where the ScCl₃ catalyst interacts with the carbonyl oxygen are clearly preferred over the complexes where the catalyst interacts with the nitrogen with an energy gain of more than 25 kcal mol⁻¹. In addition the *s-cis* conformer of the monomer and the *syn* conformer of the radical are the most stable structures as was the case without catalyst. The most stable conformations are displayed in Figure 4.13.

Notice that the Lewis acid destabilizes the monomer *s-cis*-N-ScCl₃ by 5.99 kcal mol⁻¹ Gibbs energy. Monomer (O)-ScCl₃ and Radical (O)-ScCl₃ complexes have stabilization energies of -19.59 and -24.08 kcal mol⁻¹, respectively. Whereas Sc-N distances are shorter than 2 Å for the Monomer (O)-ScCl₃ and Radical (O)-ScCl₃ complexes, Sc-N distances are longer than 2 Å in the case of Monomer (N)-ScCl₃ and Radical (N)-ScCl₃ complexes. Steric repulsions between the dimethyl groups and the catalyst may be the cause for this elongation and the destabilization of these species. Therefore, for the remainder of this article, only coordination on the carbonyl oxygens of the monomers and the radicals will be considered.

4.2.3.2. Dimeric Transition States. For the construction of the dimeric transition states, all combinations of *s-cis* and *s-trans* conformations of the monomer with *syn* and *anti* conformations of the radicalic species yielding *pro-meso* and *pro-racemo* configurations have been considered (Figure 4.11). All prestructures of possible transition states are then optimized following the standard procedure in searching transition states. It is not surprising that a combination of the most stable reactant pairs (*s-cis* monomer and *syn* radical) has the largest potential to generate the transition state with the lowest barrier. Indeed, di-TS-*pro-meso* is the lowest energy isotactic structure and di-TS-*pro-racemo* is the lowest energy syndiotactic structure (Figure 4.14). However, the energy difference between these two is negligible.

To understand the effect of the catalyst on the tacticity, transition states with ScCl₃ have been located starting from the transition state structures without a Lewis acid (Figure 4.14). Transition states in which the Lewis acid is interacting with the radical (LA-on radical), the monomer (LA-on monomer) and both (LA-bridged) have been modeled. In these structures, the coordination number of the Lewis acid seems to be the determining factor for the stability of the transition states. The most stable transition state that has only one Lewis acid/Lewis base interaction is di-TS-S1-*pro-meso*, which has a relative Gibbs free energy (RGFE) of 15.32 kcal mol⁻¹ with respect to the most stable LA-bridged transition state, di-TS-S12-*pro-meso*. This can be explained by the fact that ScCl₃ prefers penta-coordination rather than tetra-coordination. ScCl₃

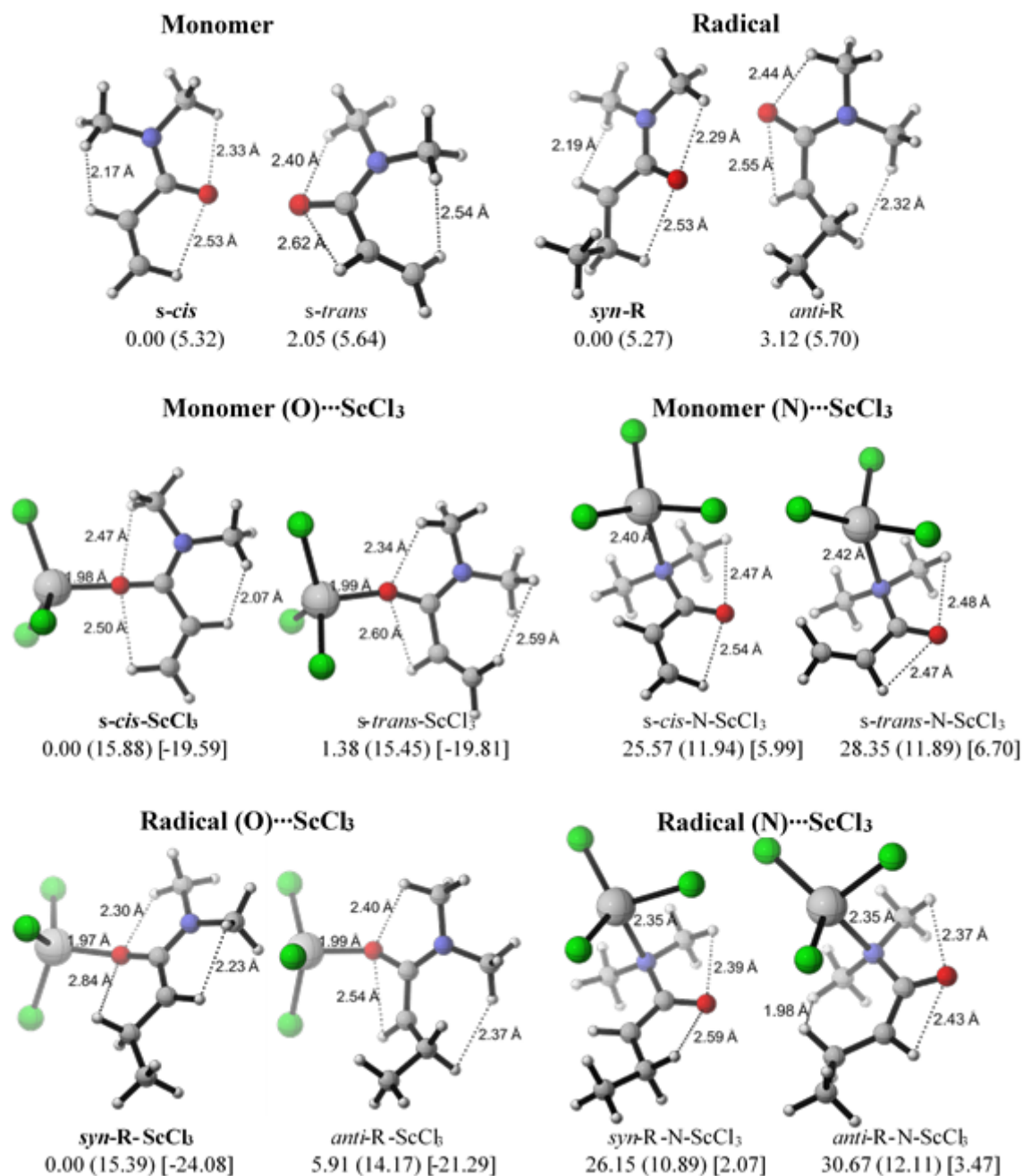


Figure 4.13. Relative Gibbs free energies (kcal mol^{-1}), dipole moments (D) in parentheses, and Gibbs stabilization energies (kcal mol^{-1}) in square brackets for the reactants in the absence and the presence of ScCl_3 in methanol (M06-2X/6-311+G(d,p)).

can have six-membered chelation with the polar groups of the monomers or the solvent in the medium due to its high coordination number [127,147]. However, due to the complexity of the transition state structures, a consistent coordination number of five will be used for ScCl_3 in the bridging position in the remainder of this article. Structures of all pro-meso and pro-racemo dimeric transition states in the presence of ScCl_3 are calculated, of which a selection of LA-bridged, LA-on radical and LA-on monomer cases is displayed in Figure 4.14. Pro-meso transition state with ScCl_3 at bridging position, di-TS-S12-pro-meso, has an interaction between the chlorine (Cl) atom of the ScCl_3 and methyl proton of the monomer, which may cause extra stabilization compared to the pro-racemo transition state di-TS-S12-pro-racemo. The Gibbs free energy differences of pro-meso and pro-racemo transition states are negligible at dimeric transition state level.

4.2.3.3. Trimeric Transition States. To better understand the role of Lewis acids in enhancing the stereoregulation during the free radical polymerization of DMAM, the study has been extended to trimers. The optimized dimeric radicalic chains and more specifically transition states resulting from combining an *s-cis* monomer and a *syn*-radical as most stable reactant pair, have been used as initial structures for the trimeric propagation (Figure 4.10, Part B). In a next step their attack to the *s-cis* monomer is considered since it was previously found to be the most stable unimeric reactant (Figure 4.15). Like in the dimeric case, pro-*meso* and pro-*racemo* transition states have comparable energies. Both structures have a curling pattern along the propagating chain, which could be expected in the absence of a Lewis acid.

In the presence of a Lewis acid, the monomer-coordination scenario in Figure 4.10 (Part 4) is omitted since it was already investigated in the dimeric case (Figure 4.14), where ScCl_3 was found to prefer the bridging position in order to have penta-coordination. So, the cases where ScCl_3 molecules are bonded to the transition states in terminal-penultimate coordination (Figure 4.10, Part 2) and terminal-monomer coordination manner (Figure 4.10, Part 3) have been modeled (Figure 4.15).

In both terminal-penultimate and terminal-monomer cases the pro-*meso* propagation is favored over the pro-*racemo* propagation. Pro-*meso* transition states have extra stabilizing hydrogen bonds between the Cl of the Lewis acid and the methyl protons of the DMAM monomer which are absent in the pro-*racemo* cases. The Gibbs free energy difference between the terminal-monomer coordinated transition state *tri*-TS-S23-pro-*meso* and its terminal-penultimate coordinated counter-part *tri*-TS-S12-pro-*meso* was negligible. Also, *tri*-TS-S23-pro-*racemo*, which has a relative Gibbs free energy of 2.74 kcal mol⁻¹, is slightly less stable than *tri*-TS-S12-pro-*racemo*. Steric crowding in the *tri*-TS-S12-pro-*meso* and *tri*-TS-S23-pro-*racemo* makes these transition states slightly less stable than their counter-parts. In the terminal-monomer coordination transition states, the Lewis acid interacts with both incoming monomer and rotatable radicalic chain end. It can be suggested that the catalyst travels to radicalic site as the chain grows, accepting the new monomer in a new terminal-monomer transition state.

4.2.3.4. Dimeric radicalic chains. Dimeric radicalic products obtained after the IRC calculations of the dimeric transition states followed by geometry optimizations are depicted in Figure 4.16. In the absence of ScCl₃, products have comparable energies. In the presence of the Lewis acid, dimeric product in *meso* configuration (*di*-P-S12-*meso*) is slightly more stable than its *racemo* counterpart (*di*-P-S12-*racemo*).

4.2.3.5. Trimeric radicalic chains. Trimeric products obtained after the IRC calculations of the trimeric transition states followed by geometry optimizations are depicted in Figure 4.17. In the absence of ScCl₃, *meso* product (*tri*-P-*meso*) is slightly more stable than the *racemo* product (*tri*-P-*racemo*). In the presence of ScCl₃, the Gibbs free energy difference between the *meso* and the *racemo* products slightly increase. Gibbs free energy difference between the *meso* products (*tri*-P-S12-*meso* and *tri*-P-S12-*racemo*) in terminal-penultimate and terminal-monomer cases are negligible.

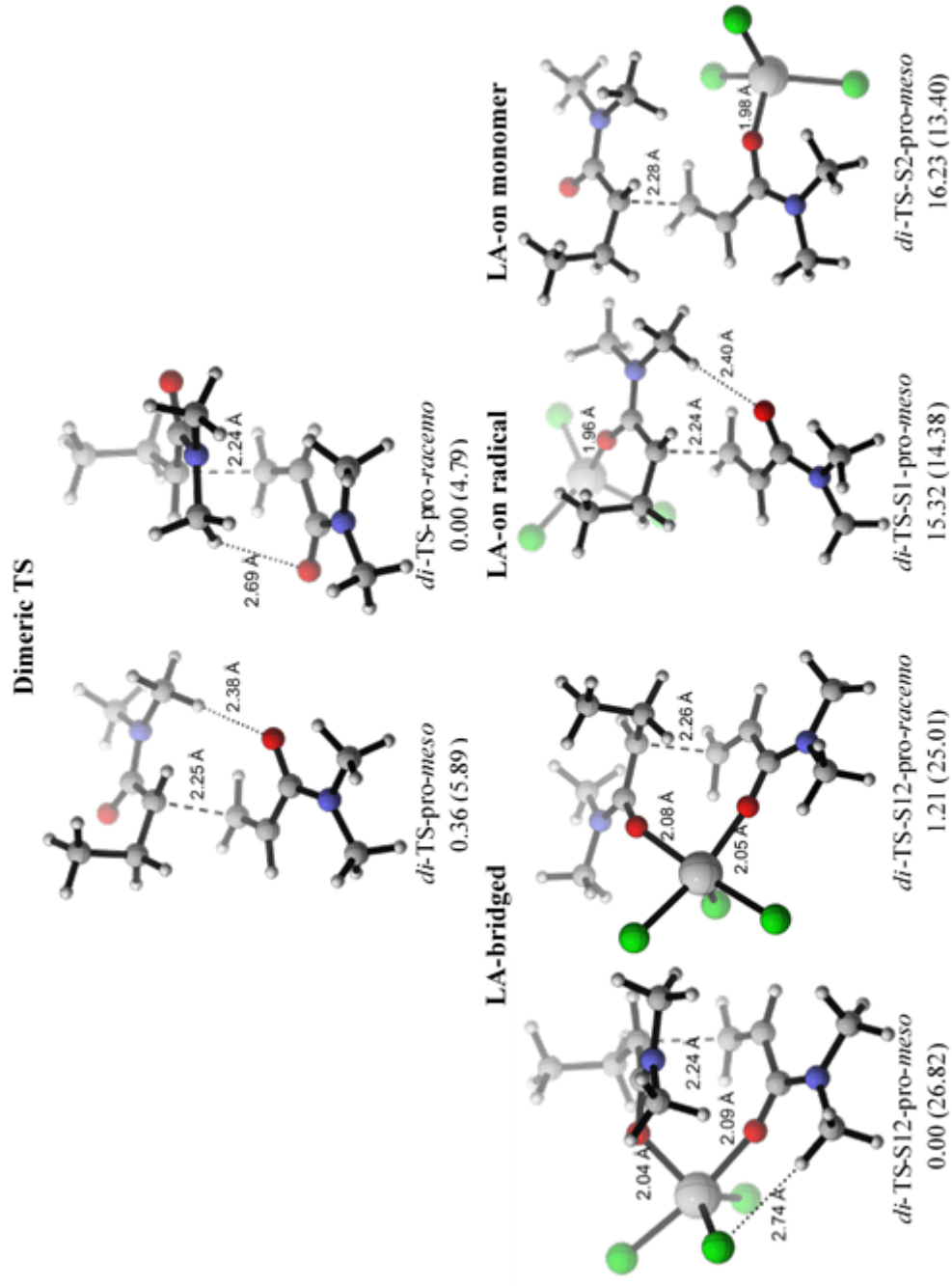


Figure 4.14. Relative Gibbs free energies (kcal mol⁻¹), and dipole moments (D) in parentheses for the dimeric transition states in methanol (M06-2X/6-311+G(d,p)).

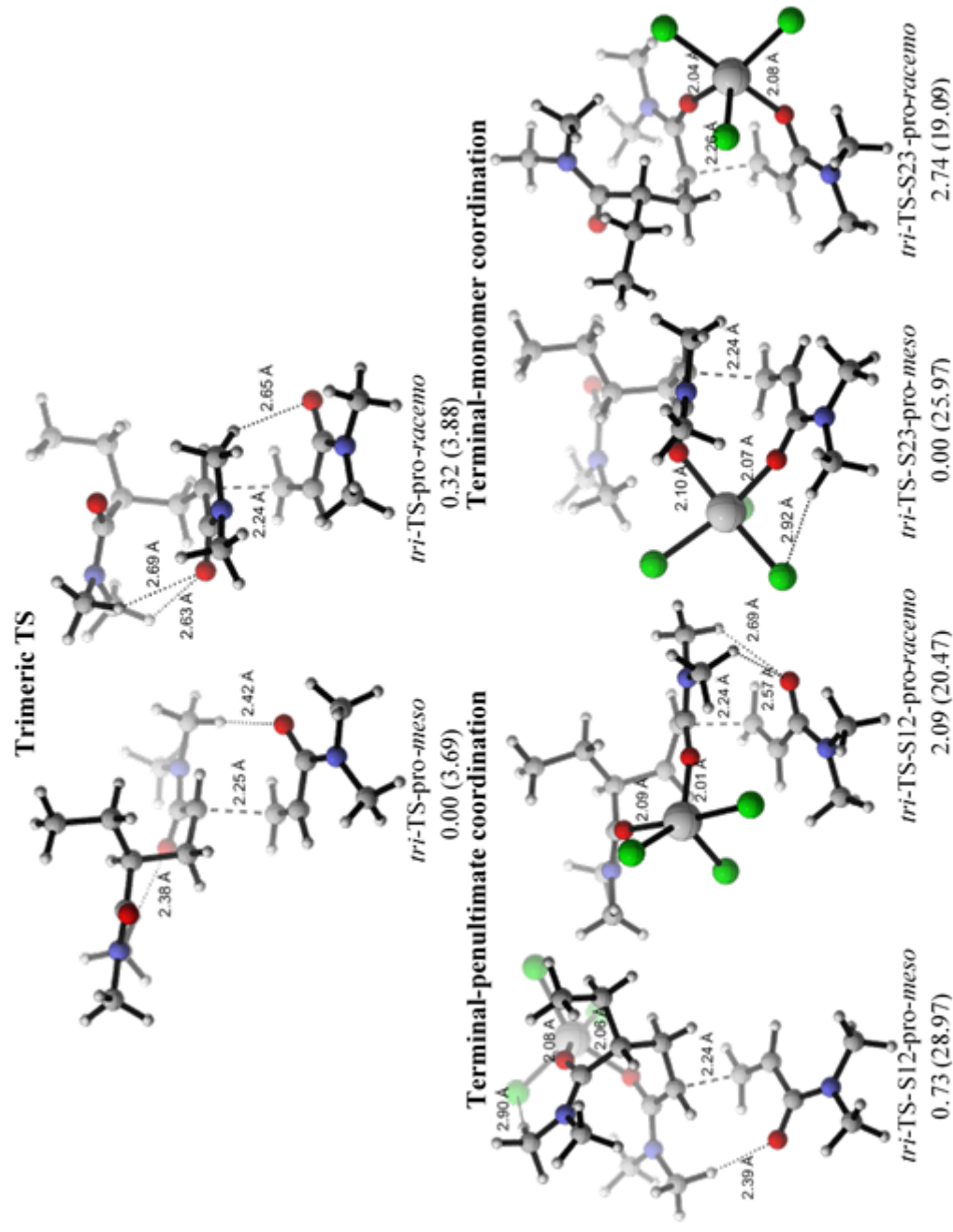


Figure 4.15. Relative Gibbs free energies (kcal mol⁻¹), and dipole moments (D) in parentheses for the trimeric transition states in methanol (M06-2X/6-311+G(d,p)).

4.2.3.6. Kinetic Results. Table 4.7 reports the kinetic results for the dimeric and the trimeric propagation steps of DMAM. In the absence of Lewis acid coordination, the *pro-racemo* propagation is favored in the dimeric case, this was also proposed in the experimental study by Habaue *et. al.*[131]. Furthermore, the difference between the Gibbs free energy barriers of the *meso* and *racemo* propagations in the trimeric case is negligible. Since the radical end of the propagating chain and the incoming monomer are easily rotatable, no stereoselectivity was expected in the absence of ScCl_3 .

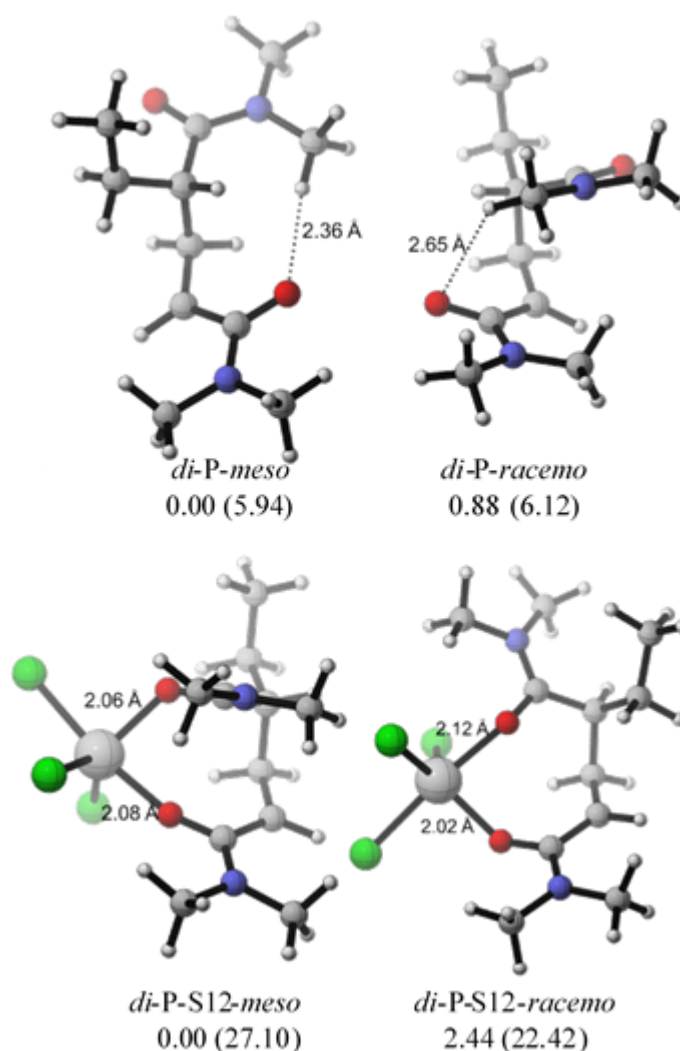


Figure 4.16. Relative Gibbs free energies (kcal mol⁻¹), and dipole moments (D) in parentheses for the dimeric radicalic chains in the absence and presence of ScCl_3 in methanol (M06-2X/6-311+G(d,p)).

In the presence of a Lewis acid, bridging to the carbonyl oxygens at the end of the propagating chain and incoming monomer in dimeric case, there is pro-*meso* selectivity. In the presence of ScCl₃ a linear propagation is observed for pro-*meso* case, that is why lower activation barriers and higher propagation rate constants are observed for these dimeric transition states. In the trimeric propagation case in the presence of Lewis acid coordination, Boltzmann distributions of pro-*meso* and pro-*racemo* transition states based on Gibbs free energies of activation revealed that 90.87% and 99.02% of the products will be in *meso* configuration both in the case of terminal-penultimate coordination and terminal-monomer coordination, respectively. Gibbs free energy barriers for terminal-monomer coordination (7.00 kcal mol⁻¹ for *tri*-TS-S23-pro-*meso* and 9.73 kcal mol⁻¹ for *tri*-TS-S23-pro-*racemo*) are lower than the terminal-penultimate case (12.27 kcal mol⁻¹ for *tri*-TS-S12-pro-*meso* and 13.63 kcal mol⁻¹ for *tri*-TS-S12-pro-*racemo*) which indicates that the terminal-monomer complexation of the ScCl₃ is more favorable stereocontrolling the path during the polymerization of DMAM. The propagation rate constants obtained both in the dimeric and the trimeric cases revealed that Lewis acid has a dual role in the propagation of DMAM by accelerating and stereocontrolling the polymerization in favor of pro-*meso* selectivity.

Table 4.7. Gibbs free energy barriers, (ΔG^\ddagger , kcal mol⁻¹), activation energy barriers, (E_a , kcal mol⁻¹), propagation rate constants, (k_p , L mol⁻¹ s⁻¹), and tacticity percentages of the best dimeric and trimeric transition state pathways at 298.15 K (M06-2X/ 6-311+G(d,p)).

	TS	Name	ΔG^\ddagger	E_a	k_p	%
no ScCl₃	dimeric	<i>di</i> -TS-pro- <i>meso</i>	13.80	2.23	1.18E-02	35.44
		<i>di</i> -TS-pro- <i>racemo</i>	13.45	1.36	2.15E-02	64.56
	trimeric	<i>tri</i> -TS-pro- <i>meso</i>	14.42	2.11	4.14E-03	63.07
		<i>tri</i> -TS-pro- <i>racemo</i>	14.74	1.34	2.42E-03	36.93
with ScCl₃	dimeric*	<i>di</i> -TS-S12-pro- <i>meso</i>	7.31	7.49	6.70E+02	88.45
		<i>di</i> -TS-S12-pro- <i>racemo</i>	8.52	9.40	8.73E+01	11.55
	trimeric**	<i>tri</i> -TS-S12-pro- <i>meso</i>	12.27	1.56	1.57E-01	90.87
		<i>tri</i> -TS-S12-pro- <i>racemo</i>	13.63	0.99	1.57E-02	9.13
		<i>tri</i> -TS-S23-pro- <i>meso</i>	7.00	6.90	1.14E+03	99.02
		<i>tri</i> -TS-S23-pro- <i>racemo</i>	9.73	9.69	1.13E+01	0.98

* "S12" refers to transition states having ScCl₃ in the bridging position between the radical and the incoming monomer.

**"S12" and "S23" refer to the terminal-penultimate and terminal-monomer coordinated transition states, respectively.

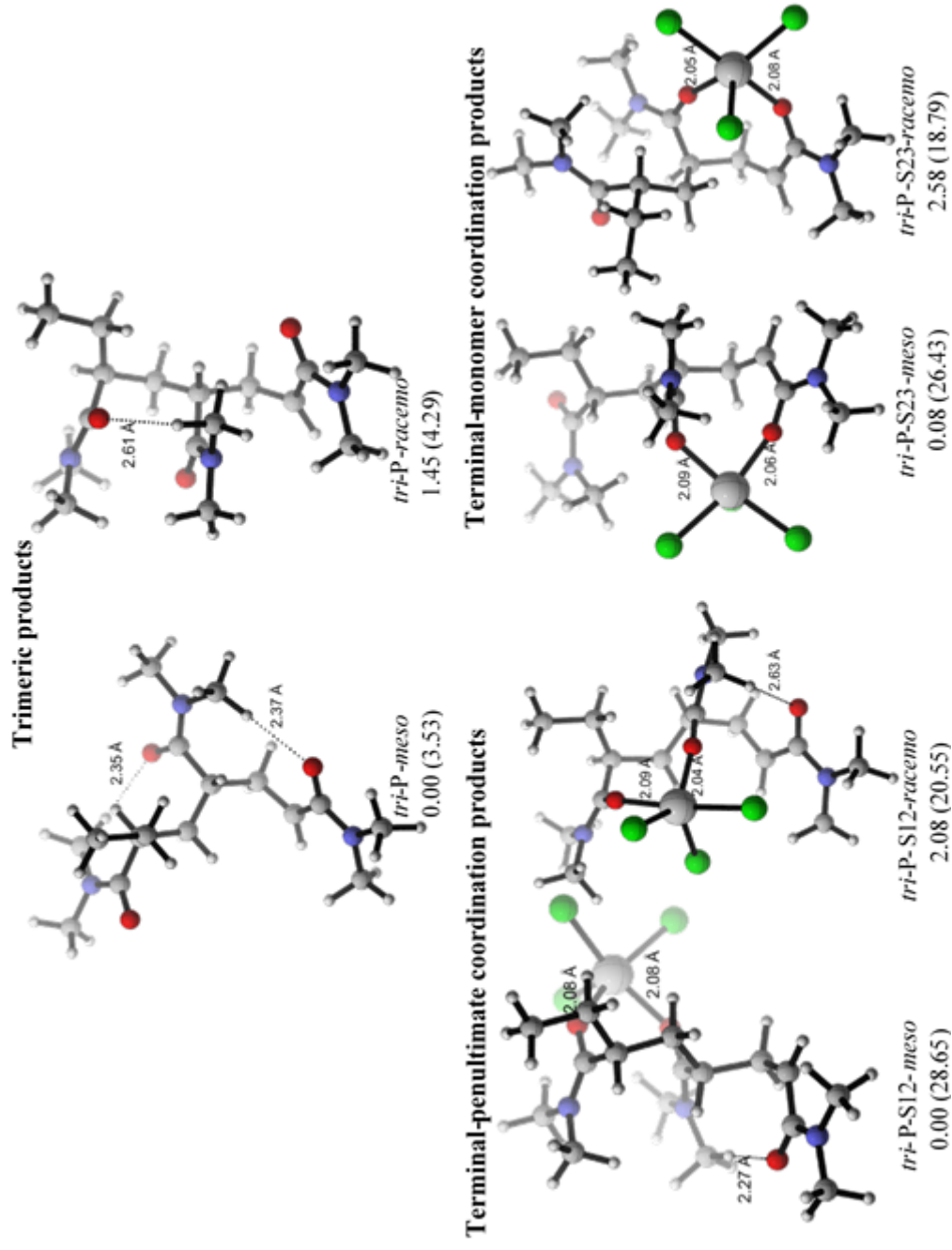


Figure 4.17. Relative Gibbs free energies (kcal mol^{-1}), and dipole moments (D) in parentheses for the trimeric products in the absence and presence of ScCl_3 in methanol (M06-2X/6-311+G(d,p)).

4.2.4. Conclusions

The mechanism of the free radical polymerization of DMAM in the absence and presence of the Lewis acid ScCl_3 and the effect of the latter on stereoselectivity have been modeled. Kinetic calculations with M06-2X/6-311+G(d,p) have shown that ScCl_3 increases the isotactic specificity for the pro-*meso* propagation both in the dimeric and the trimeric models. ScCl_3 interacts with the carbonyl oxygens of the side chains in a bridging manner, in this way the pro-*meso* propagation is favored sterically. In the presence of Lewis acid, the terminal-monomer coordination scenario was preferred over the terminal-penultimate coordination. Also, the propagation in the presence of ScCl_3 is catalytic. Such molecular level insight into the factors controlling the stereoselectivity may be obtained from detailed computational kinetic studies. Our results clearly show the catalytic function of the ScCl_3 species, as the propagation kinetics is faster in the presence of the Lewis acid. In further studies, the behavior of other Lewis acids in the polymerization of acrylamide derivatives can be investigated. On the basis of this work we suggest that strategies for effective stereocontrol need to be re-considered, our observation is such that reagents that simultaneously activate the monomer while binding to the terminal and penultimate groups are promising. A detailed DFT modeling of the propagation reaction, when carried out as demonstrated above, has the potential to guide experimentalists towards devising strategies to improve and control the stereoselectivity.

5. MULTISCALE MODELING OF POLY(2-ISOPROPYL-2-OXAZOLINE) CHAINS IN AQUEOUS SOLUTION

Poly(2-isopropyl-2-oxazoline) (PIPOX) is a thermo-responsive polymer exhibiting lower critical solution behaviour in water close to the human body temperature. PIPOX chains form crystalline nanoribbons in aqueous solutions above the critical temperature (T_c). The chain conformations in water prior to the crystallization is still much debated. In this study, a multi-scale computational approach is used to investigate the conformations of PIPOX chains well-below and well-above T_c . Molecular dynamics (MD) simulations are performed to obtain the parameters for dissipative particle dynamics simulations (DPD) which give the mesoscale morphologies of the polymer-solvent systems. Atomistic information is imposed by reverse-mapping, followed by MD simulations for relaxation. The conformation obtained from the reverse-mapping is a helical conformation with a pitch length of 15 monomers. This is the first observation of a helical chain conformation for PIPOX in water above T_c . The helical PIPOX chains are used to construct a triclinic unit cell that well-reproduce the experimental X-ray diffraction pattern for crystalline PIPOX nanoribbons formed in water above T_c . The two interacting helical PIPOX chains maintain their relative conformations at T_c , stabilized by hydrophobic interactions of the isopropyl side groups. The results are important in identifying a new helical conformation for PIPOX prior to crystallization in water above T_c . The new structure paves the way in understanding the interactions and phase transitions of thermo-responsive polymers in aqueous solutions around their T_c in light of their potential in biomedical applications.

5.1. Introduction

Thermo-responsive polymers have attracted interest as advanced materials [148, 149]. Among them, polymers showing lower critical solution temperature (LCST) behaviour are important because of their potential use in biomedical applications.

Poly(2-oxazolines) form an important class of thermo-responsive polymers showing lower critical solution behaviour in aqueous solutions. Poly(2-oxazolines) are reported to be non-toxic and can be tolerated by mammalian cells [150]. Below the critical temperature (T_c), poly(2-alkyl-2-oxazoline)s having methyl, ethyl, propyl and isopropyl side groups are soluble in water because of the hydration of the amide groups. As the temperature increases, the hydrogen bonds are weakened and the dehydration of the polymer leads to phase separation at T_c .

LCST of the aqueous poly(2-oxazoline) solutions can be controlled either by modifying the chemical structure of the chains or by changing the solvent quality. LCST of poly(2-oxazoline) was examined by the addition of 10 different salts from the Hofmeister series. As the hydrophilicity of the polymer increased, the cloud point could be tuned over a wider range upon addition of the salts [151]. In another study, the cloud point of thermo-responsive polyoxazolines was changed by altering the structure of the copolymers with click modification, thereby widening the application range for these polymers [152]. Living cationic copolymerization of 2-isopropyl-2-oxazoline with 2-n-propyl-, 2-n-butyl-, and 2-n-nonyl-2-oxazoline showed that comonomers having stronger amphiphilic character display a decrease of LCST behaviour and the LCST can be modulated by the copolymer composition [153]. Furthermore, end-group polarity in the living cationic ring-opening polymerization of 2-isopropyl-2-oxazolines is reported to affect the LCST of the resulting polymer. The introduction of hydrophobic end groups decreases the LCST, whereas hydrophilic ones increases it [154].

The length of the alkyl side chains determines the crystallization behaviour of poly(2-alkyl-2-oxazoline)s [155, 156]. The hindrance of crystallization in bulk with decreasing alkyl side chain length was attributed to stronger amide dipole interactions. In aqueous solutions, PIPOX and poly(2-ethyl-2-oxazoline) formed crystalline nanofibers above the T_c [157, 158]. Crystallization of poly(2-isobutyl-2-oxazoline) and poly(2-nonyl-2-oxazoline) was also observed in ethanol-water mixtures below the upper critical solution temperature [159].

Poly(*N*-isopropylacrylamide) (PNIPAM) is a structural isomer of PIPOX. The two isomers have the polar moiety at different locations which significantly affects their physicochemical properties in bulk and in solution. The polarity of end-groups and the pendant groups influenced the LCST of PIPOX in a much broader range compared to its structural isomer PNIPAM [154]. Layer-by-layer self-assembled films formed by association of tannic acid were reported to be thinner for PIPOX than for PNIPAM due to the availability of the carbonyl groups on the backbone of the PIPOX for hydrogen-bonding between the layers [160]. Obeid et al. studied the different behaviour of PIPOX and PNIPAM structural isomers in the formation of telechelic amphiphilic copolymers and concluded that micelles formed by PIPOX chains associates to mesoglobules above the LCST of the polymer having nearly 10 times larger hydrodynamic radii compared to the ones formed by PNIPAM chains. The distinction between these two polymers has been attributed to the hydrogen bonds formed between water molecules and the backbone amide nitrogen atoms in the PIPOX chains [161]. In contrast to PIPOX, PNIPAM shows reversible phase transition at LCST and does not form any self-assembled aggregates in water after annealing above T_c , indicating the significant effect of chemical structure and resulting chain conformations on physico-chemical properties.

The crystallization of PIPOX in aqueous solutions above T_c has been thoroughly investigated both experimentally and computationally. PIPOX nanofibers formed in aqueous solutions were characterized by scanning force microscopy, differential scanning calorimetry, and X-ray diffraction (XRD) studies [162]. Recently, crystallization of PIPOX in organic solvents was studied and the crystallites that formed were analysed by XRD. Similar diffraction peaks were observed to those crystallized in aqueous solutions [163]. However, it was concluded that crystallization process is much slower in organic solvents than in aqueous solution, and that the morphology of PIPOX crystallites is different in nonaqueous media. In the presence of co-solvents and at different concentrations, PIPOX experiences changes in morphology. Faster thermal response of PIPOX aqueous solutions compared to PNIPAM solutions due to weaker hydrogen bonding capacity of PIPOX particles was investigated by a modulated temperature differential scanning calorimetry experiment [164]. The crystallization process and the

time-dependent change of morphology of PIPOX particles were examined by XRD and cryogenic scanning electron microscopy [165]. Crystalline microparticles of PIPOX that precipitated above LCST were composed of nanofibers and crystallinity of the material reached a plateau after 8-10 h, so that isolated microspheres of uniform size were formed.

Understanding the changes in the conformation of PIPOX chains with temperature and identifying the irreversible conformational changes above T_c as precursor of crystallization in aqueous solution has been of recent interest [166–168]. A vibrational spectroscopy and molecular orbitals calculations study on PIPOX solutions revealed that above their LCST, polymer chains undergo a conformational change and adopt a mostly trans conformation during crystallization [166] which has also been supported by P. Wu et al. very recently with temperature-dependent IR spectroscopy and temperature-variable 1H NMR spectra [167]. However, in another recent study of IR/Raman spectroscopy and molecular dynamics (MD) simulations on the conformational changes of annealed PIPOX in solid state crystallization, the same group –P. Wu et al.- stated that the methylene groups on the backbone are mainly in gauche conformation, the conformation of backbone does not change much with crystallization and that this is in conflict with previous reports that in the crystalline state the backbone of PIPOX exhibits mostly all-trans conformation or PIPOX has a main-chain crystallization, because it is impossible for the backbone of PIPOX in the amorphous state to adopt an all-trans conformation [168]. Furthermore, single chain MD simulations have shown that ordered chain arrangement of amide dipoles together with the torsion of the backbone through C-N linkages is responsible for the crystallization of the PIPOX in solid state. On the other hand, the temperature effect on the polymer segment density distributions has been utilized by self-consistent lattice mean-field theory [169]. It has been concluded that favourable interactions with water at low temperatures are destroyed at elevated temperatures and water becomes a poor solvent. However, the modelling approach used in the work was not able to capture the crystallization at high temperatures.

While the crystallization of PIPOX in water above T_c has been well-established by experimental studies, the structural details such as the chain conformations above T_c prior to crystallization and how such conformations lead to the experimentally observed crystalline structures are still debated. A better understanding of the interactions at the atomistic scale for PIPOX chains in water will also help to explain the behaviour of other water-soluble polymers which may be tuned by chemical modifications. We therefore revert to computer simulations to answer these open questions.

The study of self-assembly on different length and time scales needs a multi-scale computational approach. MD simulations are amongst the most widely used techniques to study the time-dependent behaviour on the nanoscale, while retaining atomistic detail [170, 171]. Coarse-grained (CG) methods [38, 172–176] that reduce the groups of atoms into interacting beads on the mesoscale are frequently used to study oligomer morphologies. Dissipative particle dynamics (DPD) [35, 36, 38, 175, 177, 178] is a CG method which can be used for the simulation of liquid-liquid and liquid-solid interfaces [179, 180]. It makes use of the Flory-Huggins mean field theory of polymers [181–183] in which the miscibility of a polymer with a solvent is investigated by comparing the free energy of the polymer-solvent system before and after mixing. In DPD, particles correspond to beads (CG groups of atoms). Atomistic level detail can be implemented back by one of the reverse mapping procedures [172, 174, 184–186] on the CG system. Such multiscale approaches have previously been used to explain the dual scale roughness driven by microphase separation leading to tunable hydrophobicity of poly(styrene-co-perfluoroalkyl ethylacrylate) electrosprayed in THF, DMF, and their mixtures [187].

In this study, the behaviour of PIPOX chains in aqueous solution is examined by a similar multi-scale approach. MD simulations are performed on single oligomeric chains to deduce chain-solvent interactions in very dilute solutions. Hydrogen bonding analysis provides an insight on the phase separation of the chains around T_c . To obtain the multi-chain behaviour, first, MD simulations on the monomers are conducted to determine DPD interaction parameters that are used for DPD simulations to obtain the morphologies of the oligomer-solvent systems. The atomistic details are then

reverse-mapped followed by relaxation in water at full atomistic detail. The resulting chain conformations are subjected to a statistical analysis to determine most probable states which are used to construct a unit cell reproducing the XRD data of the crystalline PIPOX nanofibers formed in aqueous solution above T_c . Statistical analysis after reverse-mapping and the XRD data obtained with the model unit cell corroborates the major role of hydrophobic interactions and the helical chain conformation, which is observed for the first time for PIPOX in aqueous solution above T_c , on the crystallization of the PIPOX chain. To the best of our knowledge, this has been the first computational study to explain the phase transition of PIPOX around its T_c on the mesoscale, to find the presence of stable helical chains above T_c and to relate it with the experimental XRD pattern of the crystalline nanofibers formed in this temperature range. While the results introduce a new helical PIPOX chain conformation as precursor of crystallization, the procedure followed in this study may be adopted to provide an insight on the morphologies of similar polymers.

5.2. Computational Procedure

5.2.1. MD Simulations of single oligomeric chains in water

In this study, Materials Studio 6.0 [188] software package is used for all simulations. Amorphous Cell module of Materials Studio [189] is used for the construction of the initial simulation boxes. COMPASS (Condensed-phase Optimized Molecular Potentials for Atomistic Simulation Studies) force field [26] is used in geometry optimizations and MD simulations. This force field was shown to reproduce the conformational characteristics of PNIPAM, corroborated by density functional theory calculations [91]. For non-bonded interactions, the cutoff distance is 12 Å and a switching function with spline and buffer widths of 1.0 and 0.5 Å, respectively, is applied. Periodic boundary conditions are imposed on the systems with a cubic box of size 25.2 Å on each side generated with the Amorphous Cell module of Materials Studio. The box contains a single oligomer of eight repeating units and 500 water molecules, resulting in 10 weight % oligomer. The system is initially subjected to 5000 steps of conjugate gradients minimization converging to 1 kcal/mol/Å in the gradient of the potential. MD simula-

tions are performed to investigate the single chain conformations of PIPOX in water. Following minimization, 20 ps equilibration runs are performed in the NVT ensemble on the minimized systems. Finally, trajectory files to be analyzed are obtained with 1 ns production runs in the NVT ensemble. All MD simulations are performed both at 20°C and 60°C, which are well-below and well-above the T_c of PIPOX, respectively.

5.2.2. DPD simulations of multiple oligomers in water

The first step in the DPD simulations is to determine the beads. In this study, each repeating unit of the PIPOX chain is considered as one bead (labelled A in Figure 5.1). The DPD theory has been developed based on the assumption that beads have similar molar volumes. We therefore consider one repeat unit of the PIPOX chain as bead A and five water molecules -one solvent bead- as bead B (Figure 5.1).

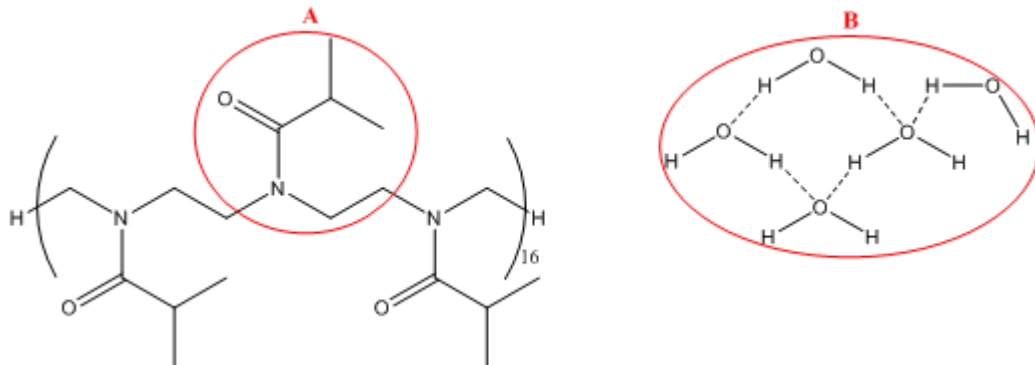


Figure 5.1. Partitioning of the beads for DPD simulations.

We next parameterize the bead-bead interactions. The maximum repulsion between interacting beads in DPD is described by a constant a_{ij} , which is calculated from the relationship for a system with a density of three DPD units:

$$a_{ij} \approx a_{ii} + 3.27\chi_{ij} \quad (5.1)$$

with $a_{ii} = 25$ (See ref. [38] for a detailed derivation of the above expression). The Flory-Huggins interaction parameter χ between DPD pairs of particles is related to the

mixing energy, ΔE_{mix} , and the molar volume of a bead, V_{bead} , through the relationship:

$$\chi = \left(\frac{\Delta E_{mix}}{RT} \right) V_{bead} \quad (5.2)$$

where R is the Boltzmann constant and T is the temperature. V_{bead} calculated by using the Spartan'08 software package [190] is 95.7 cm³/mol for A beads and 11.7 cm³/mol for one water molecule. ΔE_{mix} is defined by the cohesive energy E_{coh} per unit volume calculated through the expression [39]:

$$\Delta E_{mix} = \varphi_A \left(\frac{E_{coh}}{V} \right)_A + \varphi_B \left(\frac{E_{coh}}{V} \right)_B - \left(\frac{E_{coh}}{V} \right)_{mix} \quad (5.3)$$

where A and B represent the pure components and mix defines their blends, φ_A and φ_B are the volume fractions of the pure components in the mixture. E_{coh} is calculated from the relationship between solubility parameter (δ) obtained from Hildebrand's definition [40]:

$$\delta = \left(\frac{E_{coh}}{V} \right)^{1/2} = (CED)^{1/2} \quad (5.4)$$

where CED is the cohesive energy density.

To calculate the above parameters, 10 successive MD simulations, each 10 ps long, were performed for the monomer of PIPOX, water and their blends. MD simulations of the systems were carried out in the isothermal-isobaric (NPT) statistical ensemble, at $P = 1$ atm. To maintain the temperature and the pressure at their prescribed values, the Andersen-Berendsen thermostat-barostat is used [191, 192]. Solubility parameters (δ) are obtained from MD simulations in a box of 20 Å with 9.5 Å cutoff distances. 10 % (by weight) of monomer is mixed with 90 % water to calculate the solubility parameter for the mixtures, mimicking the experimental conditions [162]. This requires 67

water molecules for every PIPOX repeat unit. Using Equations 5.1-5.4, the calculated interaction parameter, a_{ij} , is 25.9 ± 0.8 at 20°C and 28.4 ± 0.7 at 60°C (a sample calculation is shown in the next section). Notice that $a_{ii} = 25$ for neutral interactions at a density of 3 DPD units. Thus, the PIPOX-water interactions are slightly repulsive at 20°C and repulsive at 60°C .

We then carry out the DPD simulations for chain lengths of 48 repeating units of A. Each simulation box has 9 such chains. DPD cubic boxes of size $18.2 \times 18.2 \times 18.2 r_c^3$ are constructed with a density of $\rho = 3$ DPD units, where u is the cutoff radius. Hence, the total number of beads is set to 6000, having 9 chains each with 48 repeat units, and 5568 water beads to achieve the experimental conditions of 10 wt % oligomer. The spring constant is chosen as 4.0 for consecutive beads in a chain. Systems are equilibrated with 20,000 DPD steps, followed by 150,000 steps of data collection.

5.2.3. Sample calculation for the average repulsion between interacting beads for PIPOX at 60°C

Density information for one repeating unit of PIPOX polymer and water molecule ($d_A = 0.86 \text{ g/cm}^3$ and $d_B = 0.94 \text{ g/cm}^3$, respectively) are obtained from short MD simulations. V_A ($95.74 \text{ cm}^3/\text{mol}$) and V_B ($11.68 \text{ cm}^3/\text{mol}$) are the molar volumes of the molecules.

$$wt \% A = \frac{N_A d_A V_A}{N_A d_A V_A + N_B d_B V_B} \times 100 \quad (5.5)$$

Then,

$$10 = \frac{1.00 \times 0.86 \times 95.74}{1.00 \times 0.86 \times 95.74 + N_B \times 0.94 \times 11.68} \times 100 \quad (5.6)$$

$$(N_B = 67)$$

Volume fractions of the pure components, φ_A and φ_B , were calculated as,

$$\varphi_A = \frac{V_A N_A}{V_A N_A + V_B N_B} = \frac{95.74 \times 1.00}{95.74 \times 1.00 + 11.68 \times 67} = 0.11 \quad (5.7)$$

$$\varphi_B = \frac{V_B N_B}{V_B N_B + V_A N_A} = \frac{11.68 \times 67}{11.68 \times 67 + 95.74 \times 1.00} = 0.89 \quad (5.8)$$

From Equations 5.1 - 5.4, a_{ij} for PIPOX at 60°C was calculated at every 10 ps MD simulation. As a result of 10 successive 10 ps run (total 100 ps), the average repulsion between interacting beads was calculated as 28.36.

5.2.4. Reverse-mapping and further system relaxation

To make an atomistic level explanation of the obtained morphologies, atomistic details of the beads should be reverse-mapped onto the CG system, for which there are various ways [172, 174, 184–186]. In this study, the methodology used for reverse-mapping is based on converting a bead model from the mesoscale back into atomistic representation where a combination of restraints and gradual relaxation of the atomistic geometry are performed [186]. Initially, a pattern document consisting of two files for solute and solvent molecules is formed. In the solute file, one polymer chain is constructed from 48 repeating units. Each repeating unit is taken as a motion group. In the solvent file, there are only five water molecules which are within hydrogen bonding distance of each other, forming another motion group. The particular configuration is selected as a representative of closely positioned molecules from the MD simulation of water used for cohesive energy density calculations described in the previous subsection. The polymer and the solvent beads used in the pattern document are shown in Figure 5.2. Once the reverse-mapping is completed, the constraints on the molecules in the simulation box are removed and the system is relaxed by performing geometry optimizations followed by MD simulations for further analysis.

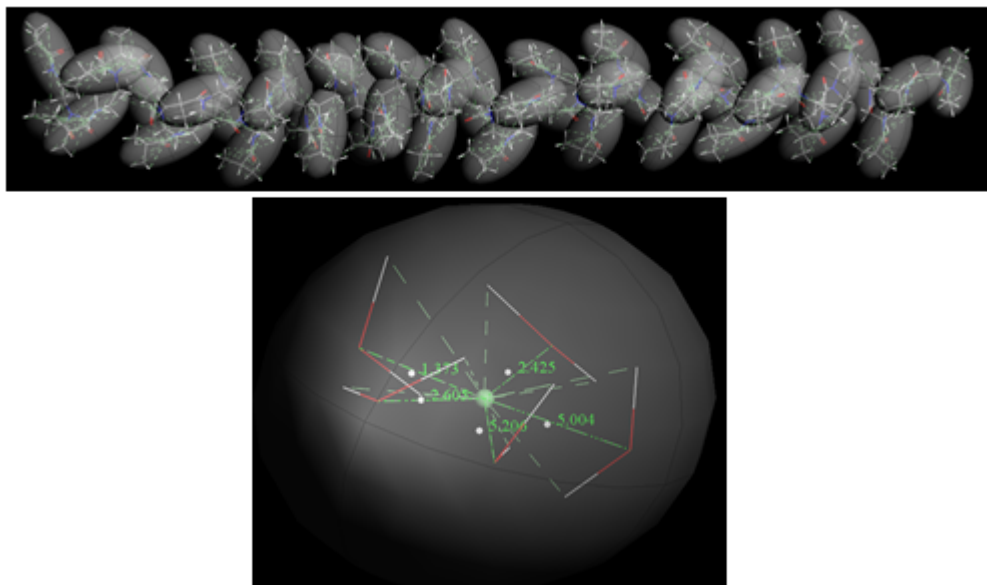


Figure 5.2. PIPOX and solvent beads used in the pattern document. A centroid was created for each bead (green beads in the centers). Green lines and numbers represent the distance of each atom to the center of mass of the bead (centroid) it belongs. Distances are kept constant by adding harmonic restraints (white dots).

5.2.5. XRD analysis

Reflex module of Materials Studio is used for the powder X-ray diffraction analysis. Bragg-Brentano geometry was used with Copper source ($\lambda = 1.54 \text{ \AA}$). The experimentally determined unit cell parameters in the literature [156,162] were modified to fit the experimental XRD data of PIPOX fibers crystallized in water above T_c [162].

5.3. Results and Discussion

5.3.1. Single chain properties of PIPOX in water

We first characterize the behaviour of single PIPOX chains in water at temperatures well-below and well-above the T_c (37°C) using MD simulations. We find the single PIPOX chains to be more compact at 60°C as opposed to 20°C with average radius of gyration values of 7.0 and 9.1 \AA at the two respective temperatures. We

seek the origin of the structural differences between the chains in the hydrogen bonding patterns. The radial distribution functions between the hydrogen atoms of water molecules and the oxygen atoms of the carbonyl groups residing on the side-chains of the oligomer, calculated at the two temperatures studied, are displayed in Figure 5.3. Carbonyl O—water H interactions are slightly more frequent below the T_c than above it. Not only is the first peak corresponding to direct hydrogen bonding interactions occurring at 1.9 \AA affected by the temperature, but also are second shell interactions and even farther density distributions decreased by the increased temperature. Moreover, we find that the lifetimes of oligomer-water hydrogen bonds are longer lived at 20°C . The number of hydrogen bonds decrease by $12 \pm 4 \%$ from 20 to 60°C , while the mean lifetime of the hydrogen bonds slightly drops from $3.4 \pm 0.2 \text{ ps}$ to $2.7 \pm 0.2 \text{ ps}$, respectively. Although the change is small, the shift is large enough to strengthen the chain-chain interactions and drive self-assembly above the T_c as we shall discuss in detail in the next subsection. However, we first investigate how these differences are reflected on the single-chain conformations in water.

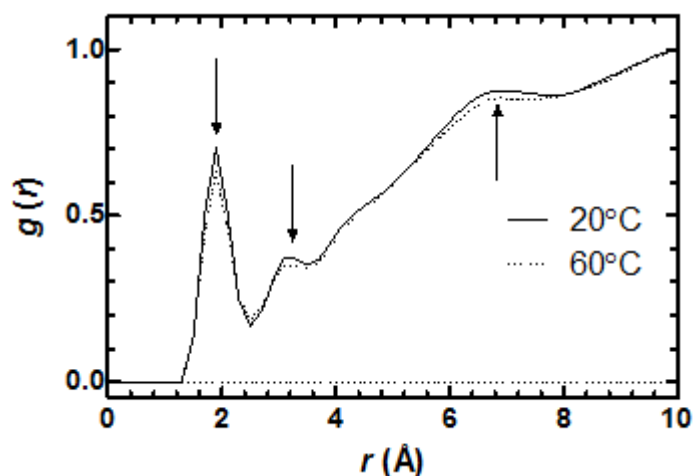


Figure 5.3. Radial Distribution Functions for the Hydrogen Bonding Interactions between PIPOX and water at two different temperatures.

To quantify the conformational behavior of the polymers in aqueous medium, we have carried out a statistical analysis over all the backbone torsional angles along the chain (Figure , Table 5.1). We then construct the structures shown in Figure using the most frequently observed values for each rotatable bond.

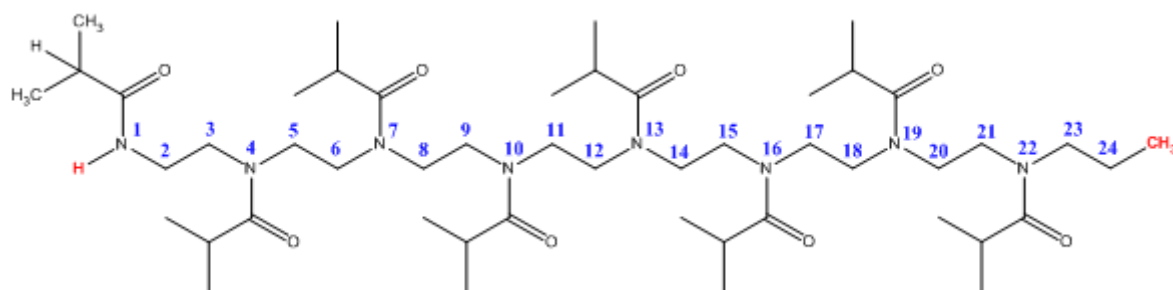


Figure 5.4. Numbering of the PIPOX chain (8 repeating units) for torsional analysis.

At 20°C, the polymer chain is elongated with the isopropyl side groups located so as to decrease the steric effects. However, above T_c , the polymer chain is desolvated and hydrophobic groups point to the same side, providing partial shielding from the solvent. As a result, the torsional analysis with even a single eight repeating unit chain below and above the T_c mimics the expected conformational behavior with longer PIPOX chains. However, to observe the intermolecular interactions between the chains, thereby the crystallization behavior of the polymer, more than one chain with higher number of repeating units must be studied. On the other hand, the number of atoms that must be included in all-atom MD simulations while mimicking the 10 weight % concentration of the experiments is prohibitively high. Moreover, the time scales needed to observe the self-assembly, starting from a random distribution of oligomers in the solvent is not achievable on realistic simulation times. We therefore revert to DPD simulations to achieve the equilibrium morphologies of multi-chain systems.

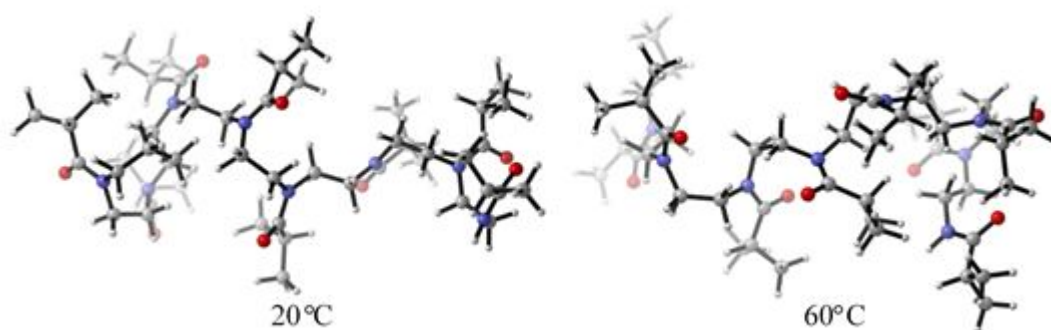


Figure 5.5. PIPOX conformations displaying the most frequently observed torsional angles in the MD simulations.

Table 5.1. The most frequently observed torsional angles during MD simulations for PIPOX (8 repeating units).

Torsional Angle	20°C	60°C
1 2 3 4	56	-177
2 3 4 5	-106	103
3 4 5 6	-93	-92
4 5 6 7	63	60
5 6 7 8	79	-93
6 7 8 9	111	-84
7 8 9 10	-177	-177
8 9 10 11	93	-86
9 10 11 12	91	94
10 11 12 13	-58	67
11 12 13 14	96	77
12 13 14 15	87	82
13 14 15 16	-171	64
14 15 16 17	91	76
15 16 17 18	-88	95
16 17 18 19	176	-59
17 18 19 20	-92	110
18 19 20 21	110	-90
19 20 21 22	-68	-171
20 21 22 23	-87	107
21 22 23 24	95	86

5.3.2. Morphologies of PIPOX chains in water

The morphologies obtained for nine, 48-repeat unit chains in water at the end of 150000 steps of DPD simulations are displayed in Figure 5.6. Periodic images of the simulation boxes are reproduced in 2 x 2 x 2 format for better visualization of the morphologies. The shapes are represented as isosurfaces around oligomeric beads, water beads are hidden for better visualization. Isosurfaces in red represent the hydrophobic groups and the grey areas represent the hydrophilic groups. At 20°C, polymer beads are miscible with water; thus, the slightly less attractive interactions between monomer and water beads compared to self-terms do not suffice to overcome the entropic tendency of chains to be distributed in the solvent. However, well-above the T_c (at 60°C), they are desolvated and a clear phase separation is observed between the solute and the solvent beads. We note that while DPD parameterization for temperatures more than $\pm 15^\circ\text{C}$

of the T_c clearly displayed solvation tendency (with a parameter close to $a_{ij} = 25$ in all snapshots evaluated) at low temperatures and desolvation tendency at high temperature (with a_{ij} close to 28 in all snapshots evaluated), it is not possible to get a consistent value within the range of the T_c . Therein, the parameter set displays a double peaked distribution, centered on either $a_{ij} = 25$ or $a_{ij} = 30$; this implies that the monomers are completely solvated part of the time, while they form clusters at other times near the T_c . This dual behavior is thought to lead to the critical behavior when the chain information and entropic contributions are factored in. Figure 5.7 depicts the density field representations of 6 successive frames (125^{th} - 130^{th} ps) during the MD simulations performed to obtain DPD interaction parameters at 40°C . It is clearly observed in Figure 5.7 that the monomers hover between the solvation and desolvation behavior within the range of T_c . Thus, while the DPD method well-represents chain behavior well-above and well-below the T_c , it is not sensitive enough to provide information near the T_c where a realistic representation of the competing interactions leading to the phase transition requires an all-atom representation.

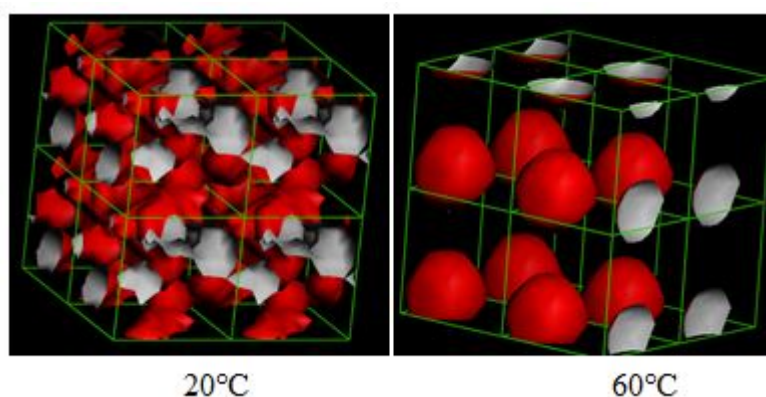


Figure 5.6. DPD simulation results for the aqueous solutions of PIPOX.

While DPD morphologies represent overall conformations of the chains in water (Figure 5.6), the atomistic detail as to whether they have tendency to form crystallites in water is lost at this level of representation. To provide an atomistic level explanation of the coagulation at high temperature and to investigate the crystallization behavior of the polymer above T_c , atomistic information is reverse-mapped to the mesoscopic structure obtained at the final snapshot of the DPD simulation at 60°C .

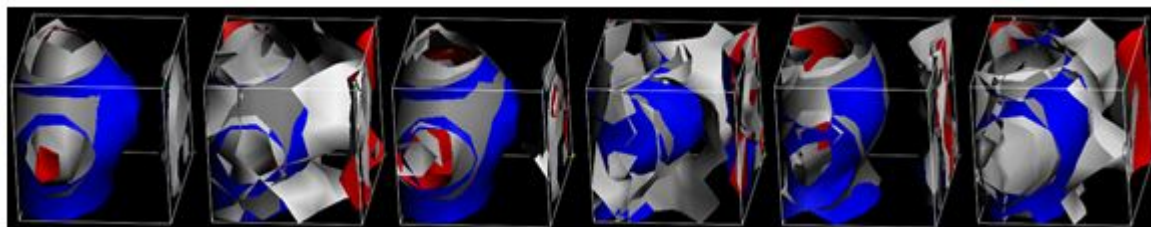


Figure 5.7. Density field representations of six successive frames (125^{th} - 130^{th} ps) during the MD simulations at 40°C .

The resulting reverse-mapped structure is shown in Figure 5.8 prior to the minimization of the system. We note that while the mapping was carried out successfully for both the oligomeric beads and solvent molecules, the latter are hidden from view for better visualization of the system. However, the atomistic structure still contains some strains, so before making any conclusions about the atomistic details, the geometry is relaxed by energy minimization, followed by MD simulations.

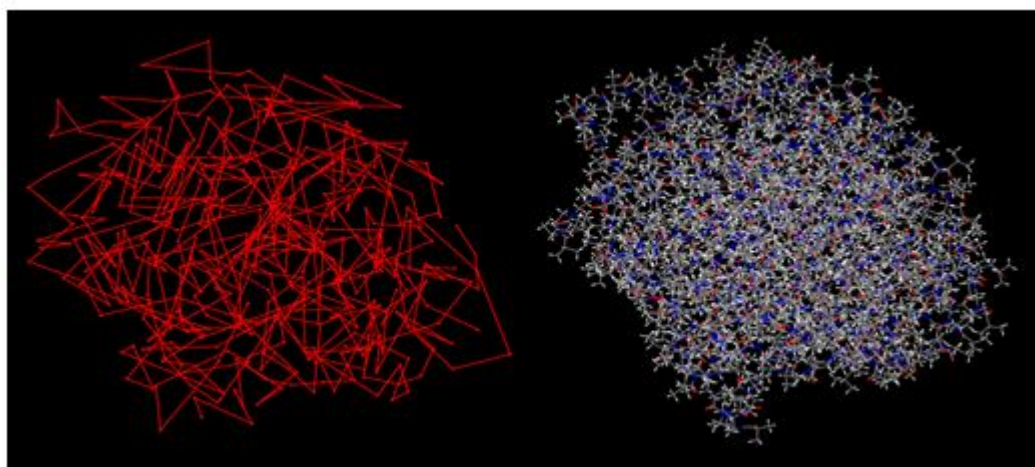


Figure 5.8. Reverse-mapping result for the PIPOX aqueous solution above T_c .

After 1 ns production run to the reverse-mapped simulation box in Figure , torsional analysis on the whole system is performed, similar to the procedure carried out for the single chains (Table). Now, we further lump the information together for the three types of torsions on the backbone of the polymer. Prior to energy minimization, the most probable value for the C-C-N-C, C-N-C-C, and N-C-C-N are 93° , -95° and -150° , respectively. We construct a 48 repeat unit PIPOX chain by repetitively setting

the three torsions to the most probable dihedral values. We then energy minimize this chain in water for 5000 steps, and carry on to the next round of energy minimization by using the most probable values obtained in the previous step. After 10 cycles of such optimization, average values for C-C-N-C, C-N-C-C, and N-C-C-N dihedrals converge to 102° , -89° , and -177° , respectively. Using these torsional angles, the most probable structure for the PIPOX chain at 60°C is shown in Figure . The chain has a helical conformation with a helical pitch of 15 monomers. We verified the pitch by measuring the backbone RMSD of two consecutive 15 repeating units pieces for which the value was 2.1 \AA . Note that the chain backbone is in helical conformation, but the side chain orientations are disordered and do not display a perfect overlap in consecutive pitches.

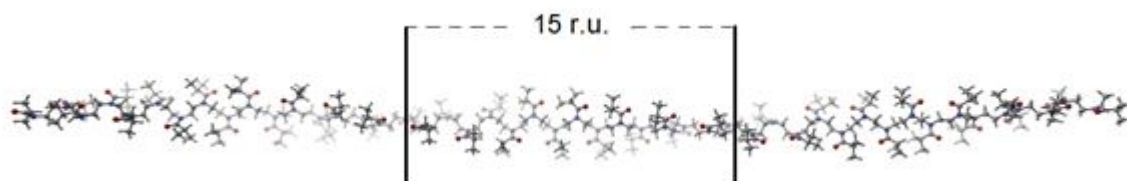


Figure 5.9. The most-probable PIPOX chain at 60°C after MD simulation to the reverse-mapped system.

This is the first time that a helical PIPOX chain conformation was observed in water above T_c . Previous spectroscopic and computational investigations [166,167] indicated that irreversible conformational transition to all-trans conformation occurred prior to crystallization which led to the conformation taken by the chain in the crystalline phase. The impossibility of all-trans PIPOX chain conformation was also reported [168]. To check whether the helical chain conformation can be a precursor of crystallization and lead to the experimentally observed crystalline structure [162], a triclinic unit cell was constructed using the helical chains as the building blocks as described below.

5.3.3. Structure and Stability of Crystalline PIPOX Fibers

One pitch of the helical chain in Figure 5.9 was taken as the building block for the PIPOX crystal. The XRD data of PIPOX fibers formed in aqueous solutions above the cloud point temperature [162] was taken as reference to construct a unit cell. Because of the vibrations and the lack of full crystallization behavior due to kinetics in the experimental environment, measured XRD peaks are broader than the calculated XRD peaks [155]. So, only the peak positions and the relative peak intensities will be compared with the experimental data. Figure (a) shows two helical chains along the helical axis and an assigned triclinic unit cell. The lattice constants are $a = 11.30 \text{ \AA}$, $b = 5.00 \text{ \AA}$, $c = 6.37 \text{ \AA}$ and the angles are $\alpha = 76^\circ$, $\beta = 89^\circ$, $\gamma = 88^\circ$. The neighboring chains in the b-direction (horizontal axis) are shifted along the helical axis such that the isopropyl side groups are partially interdigitated. This results in smaller distance between the centers of the helical axes in b-direction compared to a-direction. Experimentally, periodicity along the backbone of a PIPOX chain (-NCCNCC-) was found to be 6.4 \AA [156] which is consistent with the model cell having two twisted monomers in c-direction. The chains are extended in the c-direction not in all-trans, but in a helical conformation. Figure 5.10(b) shows the calculated XRD data corresponding to the unit cell of Figure 5.10(a). The calculated XRD data reproduced quite well the experimentally measured major peak positions at $2\theta = 7.84^\circ$ ($d = 11.30 \text{ \AA}$, (100) planes), 14.35° ($d = 6.18 \text{ \AA}$, (001) planes), 15.70° ($d = 5.65 \text{ \AA}$, (200) planes), 16.30° ($d = 5.42 \text{ \AA}$, (101) and $(10\bar{1})$ planes), 18.30° ($d = 4.850 \text{ \AA}$, (010) planes), 20.20° ($d = 4.40 \text{ \AA}$, $(11\bar{0})$ planes) and 21.4° ($d = 4.150 \text{ \AA}$, $(20\bar{1})$ planes), as well as their relative intensities.

Experimentally, the crystalline PIPOX fibers formed above T_c were found to be stable when temperature was decreased to below T_c . To check the stability of two interacting chains in water at the determined T_c of 37°C , the chains in Figure 5.11(a) were immersed in a simulation box of size $20 \times 15 \times 50 \text{ \AA}$ and filled with water molecules. The system was equilibrated with 1 ns MD run. Figure 5.11(b) shows the two chains at the end of equilibration after removing the water molecules from the system. The chains maintained their physical interaction and could not be dissolved by the water

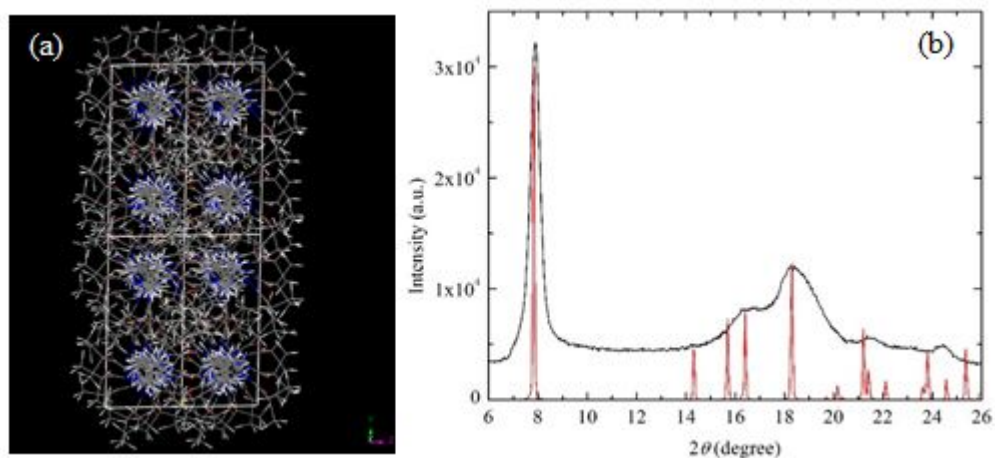


Figure 5.10. Triclinic unit cell assigned to two helical PIPOX chains: $a = 11.30 \text{ \AA}$; $b = 5.00 \text{ \AA}$; $c = 6.37 \text{ \AA}$; $\alpha = 76^\circ$; $\beta = 89^\circ$; $\gamma = 88^\circ$; (b) XRD data: Crystalline PIPOX nanoribbons formed in H_2O at 65°C (black); calculated XRD of the unit cell in (a) (red).

molecules. Although the orientation of one chain rotated slightly with respect to the other chain, the chains maintained their helicity and relative alignment along the chain axis. Figure 5.11(b) shows that the isopropyl side chains on either chain aligned towards each other, creating a layer of hydrocarbon units. We thus conclude that hydrophobic interactions play a dominant role in the stability of crystalline PIPOX fibers in water once they are formed. In order to support the idea that hydrophobic interactions have the major role on the stability of helical structure, another 1 ns MD run was performed by taking a single chain from the simulation box in Figure 5.11(b). The equilibrated single chain at the end of the simulation at 37°C is depicted in Figure 5.11(c) in which the helicity is destroyed and intra-chain hydrophobic interactions, thereby coil formation, are observed. Radius of gyration values of the two chains in Figure 5.11(b) are both 14.1 \AA , whereas it is 13.4 \AA for the single chain in Figure 5.11(c) showing that the single chain is more compact due to intramolecular hydrophobic interactions.

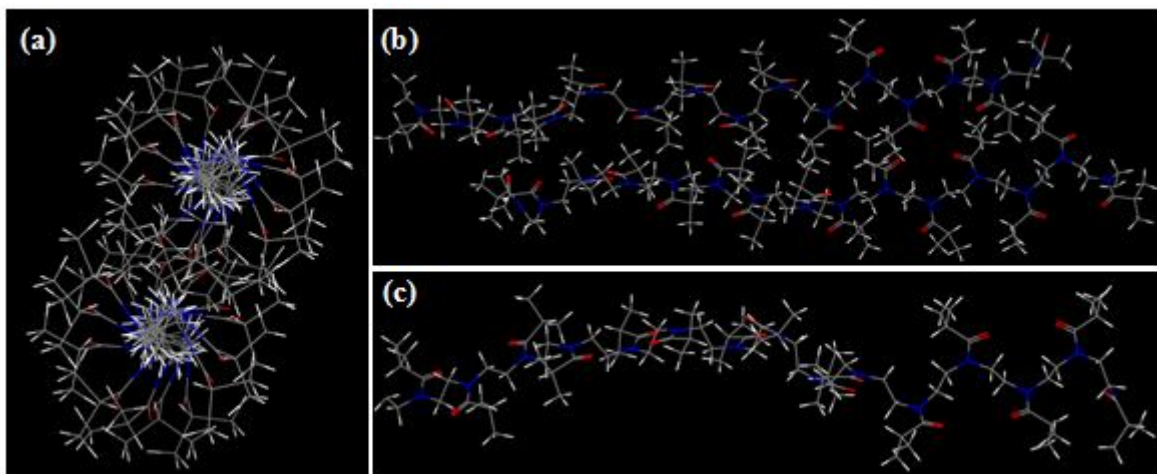


Figure 5.11. (a) The pair of helical chains selected for stability analysis. (b) Chains that are immersed in water as a pair and (c) a single chain in water at the end of 1 ns equilibration.

5.4. Conclusions

The morphological behavior of PIPOX well-below and well-above its T_c has been examined by the aid of a complementary set of computational tools. DPD interaction parameters obtained by the short MD simulations at 20°C and 60°C provided initial information about the morphologies at these temperatures. In particular, a small decrease in the amount of hydrogen bonding capacity is found to lead to the switch from a more open to a slightly more compact conformation even for a single oligomeric chain. DPD simulations for multiple chains revealed that below T_c , hydrophilic interactions are favorable, so that the polymer is miscible with the solvent. However, above T_c , hydrophobicity dominates, so that the polymers agglomerated in a spherical morphology. To obtain an atomistic explanation of these agglomerates above the T_c and to examine if crystallization is feasible, a reverse-mapping procedure was applied. After successive geometry optimizations on the reverse-mapped geometries, the most probable PIPOX chain internal coordinates well-above the T_c were evaluated. The chain had a helical conformation with a pitch of 15 monomers. A triclinic unit cell was formed using these helical chains as building blocks and the experimental XRD data of PIPOX fibers formed in water above T_c was reproduced. The two helical chains con-

sisting of isopropyl groups at the periphery were stabilized by hydrophobic interactions and maintained their structure even at T_c while single chains resulted in disordered conformations. The slightly reduced propensity of hydrogen bond formation above T_c throws the balance towards maximizing hydrophobic contacts between adjacent chains by adopting a repeated structure with interdigitated side chains, while single chains cannot sustain the helical conformation on their own and tend to collapse. Thus, the results introduce the helical conformation as the precursor leading to crystallization of PIPOX chains in water above T_c . The procedure followed in this study may be adopted to predict the morphological behavior of similar polymers in different solvents to interpret experimentally determined structural parameters. The presence of helical chain conformation found above T_c is the first in the literature, to the best of our knowledge. The multi-scale procedure used in this work provides a prescription for future studies on similar systems for proposing plausible atomistic detail to experimentally obtained data.

6. MODELING THE KINETICS IN CATIONIC RING-OPENING POLYMERIZATION OF BENZOXAZINES

6.1. Introduction

1,3-Benzoxazines are a class of heterocyclic compounds which are able to undergo ring opening polymerization, resulting in highly advanced materials in terms of mechanical strength, thermal stability, and durability under humid environment [193]. They have gained increasing interest in the materials science especially as the potential materials for the aerospace application. One of the significant advantages of benzoxazines is their easy synthesis from the corresponding phenolic compound, amine, and formaldehyde [194]. The molecular structure of the polybenzoxazines provides various design flexibility, thereby allowing the adjustment of the properties of the cured materials for a wide range of applications [195]. Unique features of the polybenzoxazine resins are (i) near-zero volumetric change upon curing, (ii) low water absorption, (iii) for some polybenzoxazine based materials much higher T_g than cure temperature, (iv) high char yield, (v) no strong acid catalysts required for curing, and (vi) release of no by-products (even nontoxic) during curing [196]. However, high polymerization temperatures to obtain polybenzoxazines may be disadvantageous since the corresponding polymer may be damaged or degraded at high temperatures [197–199]. So, catalysts involving Lewis acids [200–207] and nucleophilic catalysts [200–203] have been used to lower the polymerization temperature.

Since spectroscopic observation of active species is difficult, mechanism of ring opening polymerization of benzoxazines remained speculative over the years of study on this subject. In 1968, ring/chain tautomerism upon protonation of 3,4-dihydro-2H-1,3-benzoxazines was proposed [208]. Iminium ions in the chain form were produced by the migration of the proton from the oxygen to the nitrogen atom. Riess *et.al.* [209] proposed a mechanism where various kinds of phenols are used for the protonation in

the initial ring-opening step. Product is obtained after condensation of the iminium species. Dunkers and Ishida [205] proposed that the ring-opening polymerization of benzoxazines initiated by the protonation of oxygen atom to form iminium ion followed by the electrophilic aromatic substitution. However, it was proposed that ring/chain tautomerism with the iminium species is observed under acidic conditions [208]. Also, it was proven that to obtain high molecular weight polybenzoxazines with monofunctional benzoxazine monomers is quite difficult with Lewis acid catalysts [210]. It has been proposed that at elevated temperatures with less acidic cationic initiators, benzoxazine monomers polymerize to a phenylether (N,O-acetal linkage) repeat unit [206] and then rearranges to the phenolic (Mannich-type) structure [201]. Also, depending on the type of the catalysts used, phenoxy or phenolic type polymer structures can be obtained [211]. Yagci *et.al.* studied photoinitiated cationic polymerization of a monofunctional benzoxazine at room temperature and proposed different ring-opening processes of the protonated monomer either at the oxygen or nitrogen atoms can cause different structures [211]. Also, Wang and Ishida studied the effect of position of substituents on the resulting polymers and proposed 3 different mechanisms giving rise to phenoxy and phenolic type polymers [212]. In 2010, Chutayothin and Ishida [210] claimed that in the protonation initiation step, the oxygen protonated species is reactive and the nitrogen one is stable, and the Mannich bridge structure (phenolic) is less stable than methylene bridge structure and can be rearranged to it. In 2011, a comprehensive mechanism with lithium iodide as bifunctional catalyst was proposed [213]. Lithium cation is the Lewis acid and effectively coordinates with the oxygen or nitrogen atoms and promotes ring-opening mechanism generating three possible cationic intermediates resulting in the polymers having phenoxy and phenolic structure. Finally, the phenoxy structure is transformed into the phenolic structure by rearrangement.

The cationic polymerization mechanism of benzoxazine resins are still not well established. In this study, for four methyl substituted benzoxazines depicted in Figure 6.1, possible cationic ring-opening polymerization mechanisms that are proposed by Wang and Ishida [212] and possible rearrangement mechanisms during the polymerization will be modeled by quantum mechanical tools to shed light on the polymerization mechanisms of these monomers.

6.2. Computational Procedure

Cationic ring-opening polymerization of the monomers in Figure 6.1 will be studied by density functional theory (DFT) with the Gaussian 09 program package [106]. To achieve our goal, the stationary points corresponding to the 3D structures along the reaction paths depicted in Figure 6.2 will be located using M06-2X/6-31+G(d,p) [10] since this methodology is recommended for thermochemistry, kinetics, and noncovalent interactions. Geometries in solution will be located using the Conductor-like Polarizable Continuum Model (CPCM) [96, 214].

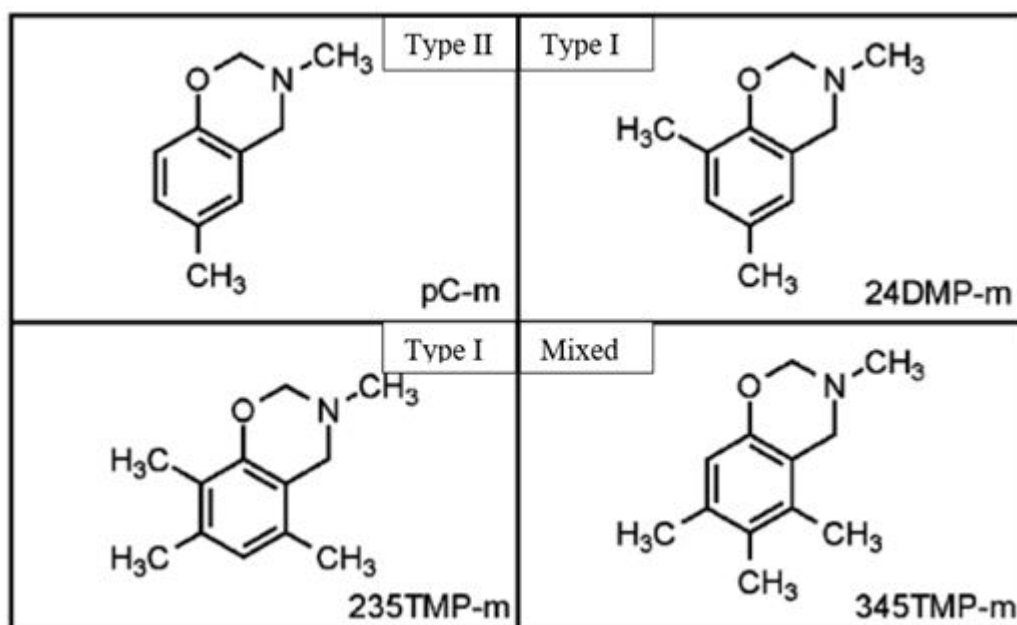


Figure 6.1. Methyl substituted benzoxazines to be modeled.

Wang and Ishida proposed that the change in the position of the substituents gives rise to the phenoxy (Type I) or phenolic (Type II) types of polymers from the starting materials depicted in Figure 6.1 [212]. To obtain the desired products, mechanisms in the Figure 6.2 were proposed and this study will start with the modeling of ring-opening upon protonation (TS1 in Figure 6.2) of the monomers and following phenolic and phenoxy type product formation (TS2 in Figure 6.2). The rearrangement of the phenoxy product to the phenolic product is investigated, too. For this purpose, bromine which behaves like a nucleophile in the proposed rearrangement mechanism is used as catalyst [213] (Figure 6.2). Also in an earlier experimental study, the main

chain rearrangement was achieved at high temperatures around 150-200°C in the absence of a catalyst [201].

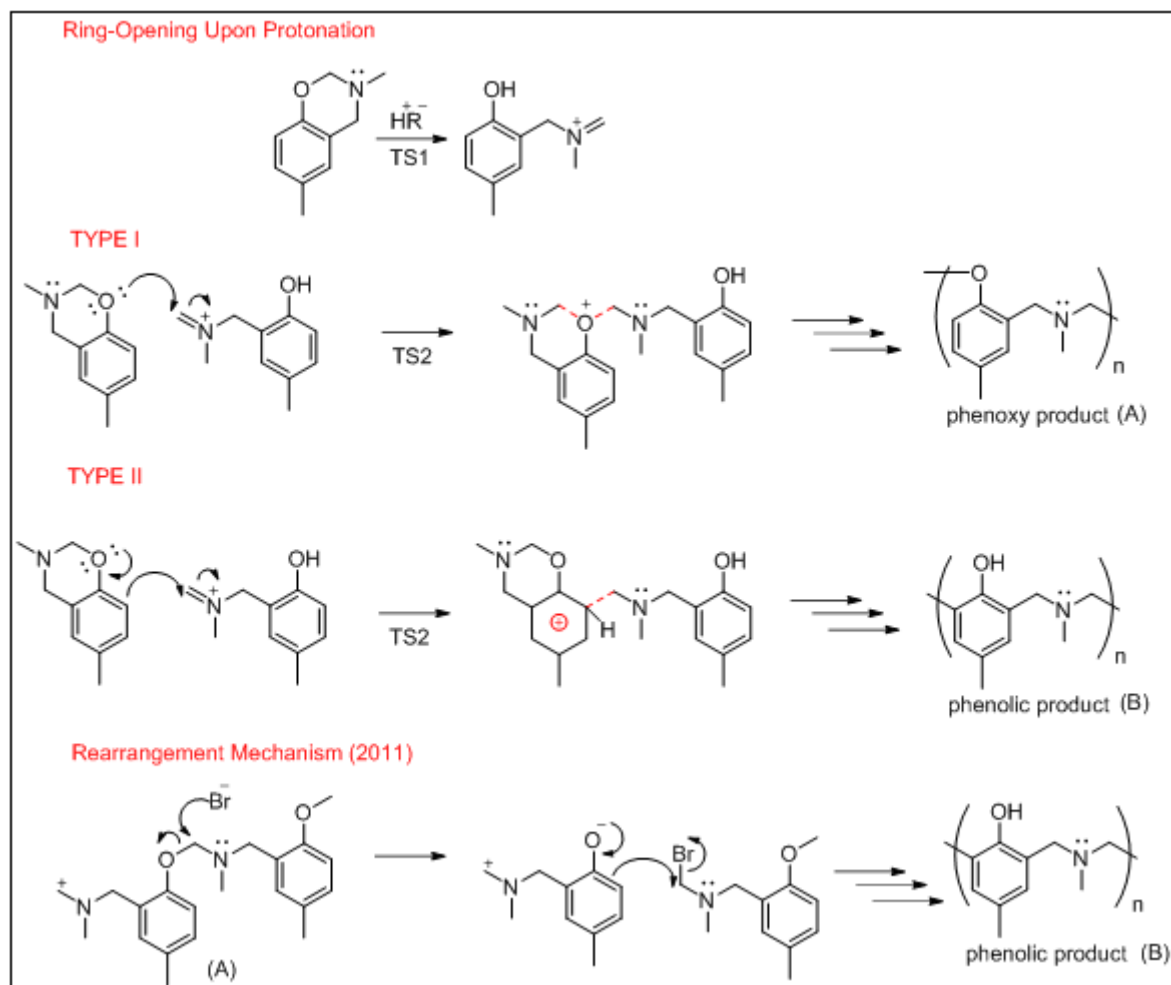


Figure 6.2. Ring-opening, propagation and rearrangement mechanisms for pC-m.

6.3. Results and Discussion

6.3.1. Ring-Opening Upon Protonation

First of all, a conformational analysis was performed on the monomer pC-m, its most stable conformations are depicted in Figure 6.3. A single crystal X-ray crystallographic study [215] revealed that the preferential conformation of a mono-oxazine ring containing benzoxazine is a distorted semi-chair structure. Nitrogen atom is located

Table 6.1. Relative Gibbs Free Energies (kcal/mol) of the most stable conformers of monomer pC-m. (Relative electronic energies (kcal/mol) are given in the parenthesis). (Functional/6-31+G(d,p)).

	pC-m1	pC-m2	pC-m3	pC-m4
B3LYP	1.44 (1.07)	0.36 (0.02)	1.45 (1.07)	0.00 (0.00)
B3LYP-CPCM	0.53 (0.47)	0.00 (0.00)	0.43 (0.46)	0.02 (0.00)
M06-2X	2.44 (2.04)	0.00 (0.00)	2.44 (2.03)	0.19 (0.02)
M06-2X-CPCM	1.56 (1.25)	0.00 (0.01)	1.56 (1.25)	0.02 (0.00)

above the benzene ring plane and the carbon atom between the oxygen and nitrogen is below the plane. Our preliminary results support these findings (Table 6.1). The monomer having the lowest Gibbs free energy (pC-m2) was selected as the starting monomer for the rest of the study. For the CPCM calculations, water was chosen as the reaction medium.

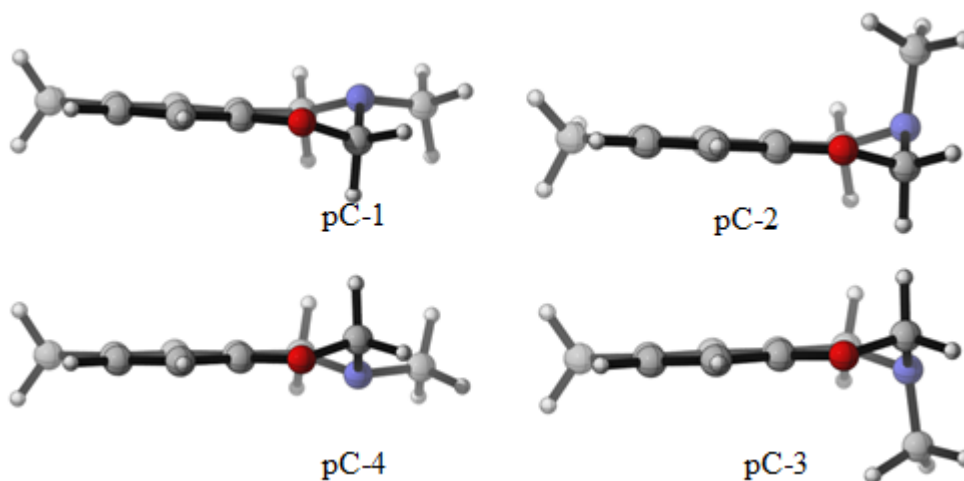


Figure 6.3. Most stable conformers for the monomer pC-m.

Monomers in Figure 6.3 were protonated initially at oxygen atom. It was observed that ring structure of only 2 of the monomers (pC-m2 and pC-m3) remained closed and the others were easily opened (Figure 6.4). Opened protonated monomer (p-pC-m-open) was 30 kcal/mol more stable than the closed ones in water. So, low kinetic barriers were expected for the ring-opening step upon protonation of the monomers.

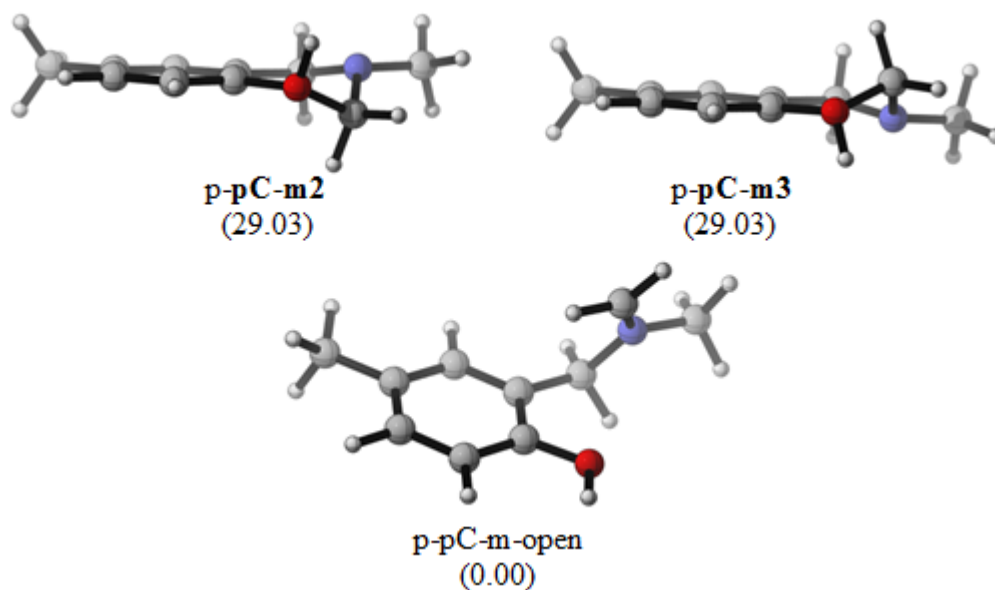


Figure 6.4. Protonated monomers and their relative Gibbs free energies (kcal/mol).
 (M06-2X/6-31+G(d,p) – CPCM).

Dunkers and Ishida [205] proposed that in the presence of a strong organic acid like trifluoroacetic acid (CF_3COOH), ring opening polymerization of benzoxazine occurs immediately at room temperature. However, in the presence of a weaker organic acid, like sebacic acid, polymerization was slow. So, for an initial guess on the ring-opening part of the polymerization, trifluoroacetic acid formula and acetic acid (CH_3COOH) were selected as strong and weak acids, respectively. Transition

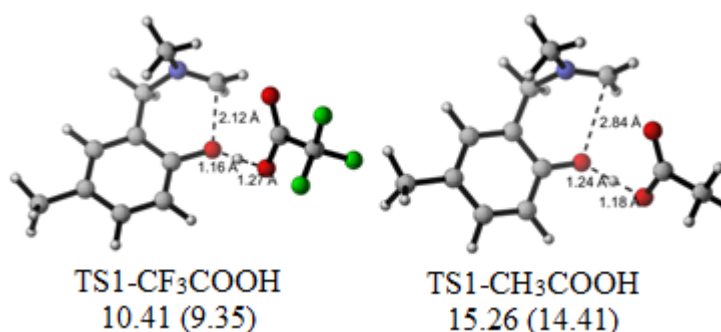


Figure 6.5. Gibbs free energy, ΔG^\ddagger and activation energy barriers (in parenthesis), E_a (kcal/mol) for TS1 for pC-m with trifluoroacetic acid (CF_3COOH) and acetic acid (CH_3COOH). (B3LYP/6-31+G(d)- Gas phase).

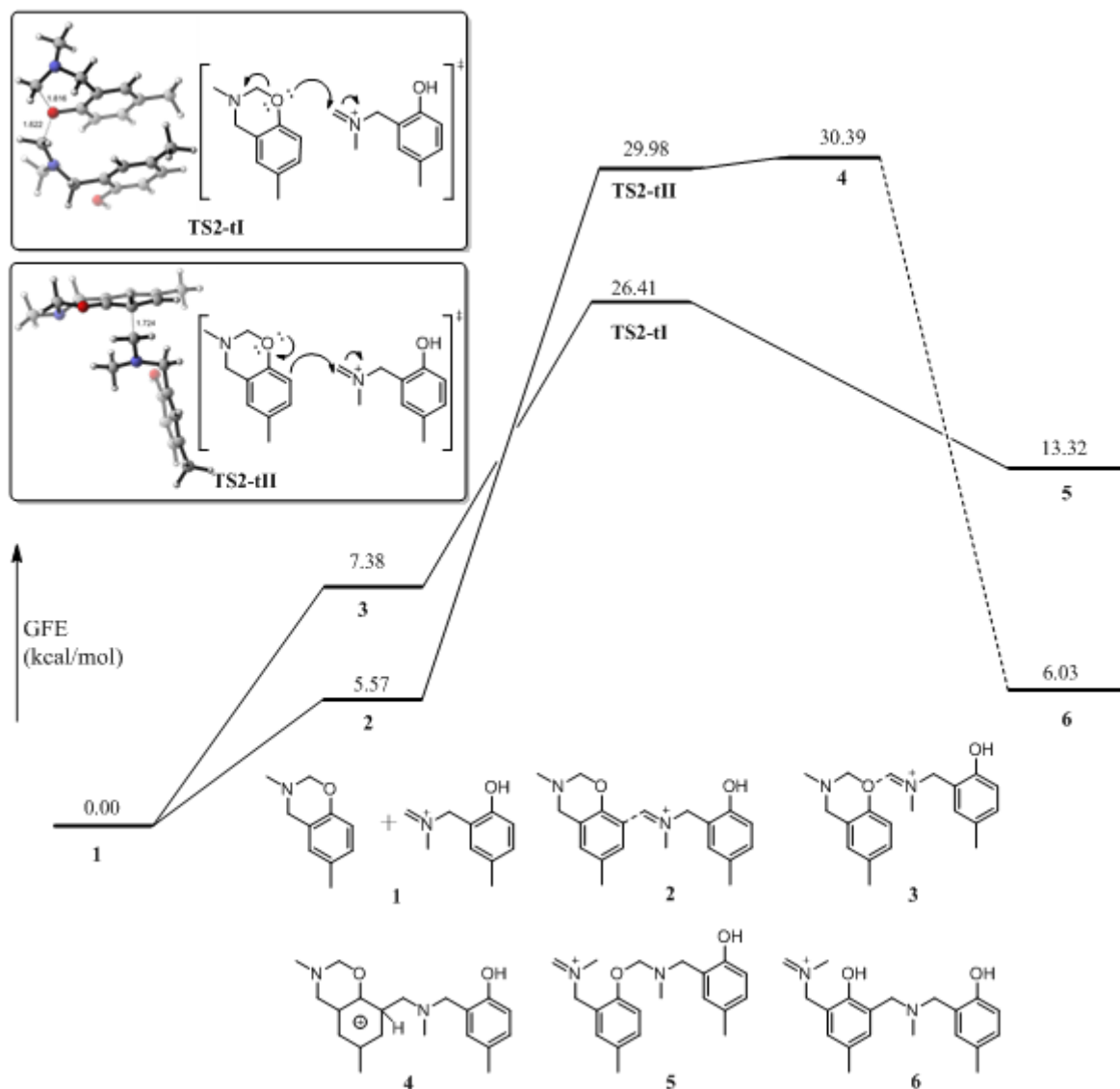


Figure 6.6. Reaction paths and Gibbs free energy barriers for Type I and Type II chain propagation steps (M06-2X/6-31+G(d,p) – CPCM).

state structures and the Gibbs free energy and activation energy barriers for the ring-opening step (B3LYP/6-31+G(d)-gas phase) with the protonation of oxygen atom on the benzoxazine rings are shown in Figure 6.5. In the presence of acetic acid, Gibbs free energy and activation energy barriers for ring-opening step were lower than the case with the strong acid. These preliminary results were in accordance with the experimental results showing the slower ring-opening with the catalysis of a weak acid.

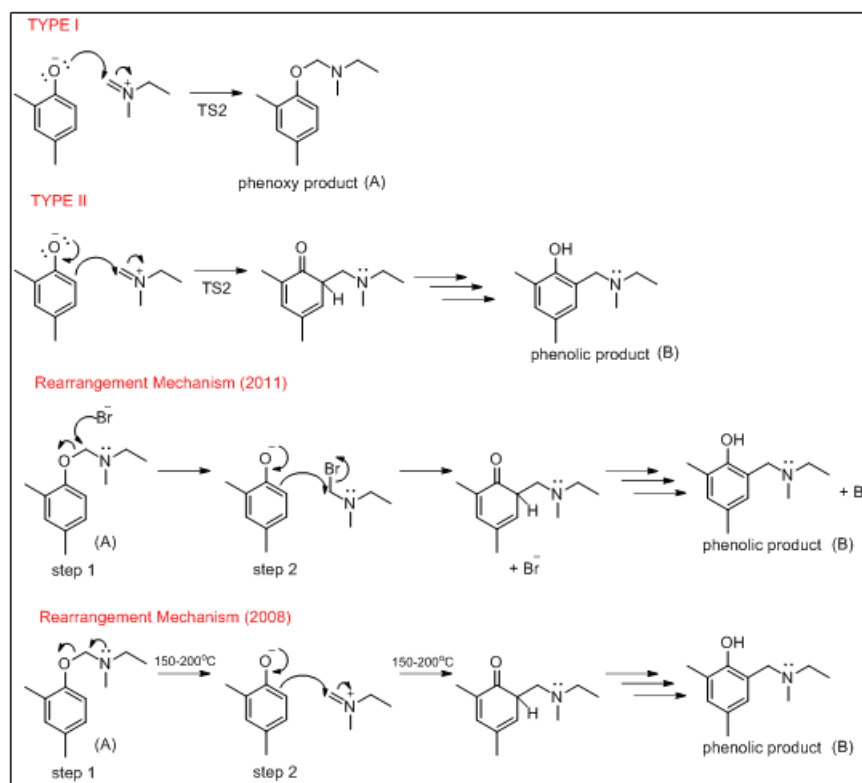


Figure 6.7. Mechanisms for model reactions.

6.3.2. Type I and Type II Chain Propagation Mechanisms for pC-m

Chain propagation for pC-m monomer in water was modeled both following the Type I and Type II mechanisms. According to the experimental study [212], Type II product was expected from this monomer. However, calculated Gibbs free energy barrier for Type I mechanism was lower than Type II mechanism (Figure 6.6). On the other hand, Type II product was thermodynamically more stable than Type I product by 7.29 kcal/mol in terms of Gibbs energy. So, some rearrangement mechanisms may be expected starting from the Type I product (phenoxy).

6.3.3. Rearrangement of phenoxy product to phenolic product

In order to reduce the computational cost in designing rearrangement mechanisms, reaction paths are constructed with model structures as shown in Figure 6.7. Also, Type I and Type II mechanisms are re-constructed with model systems to be

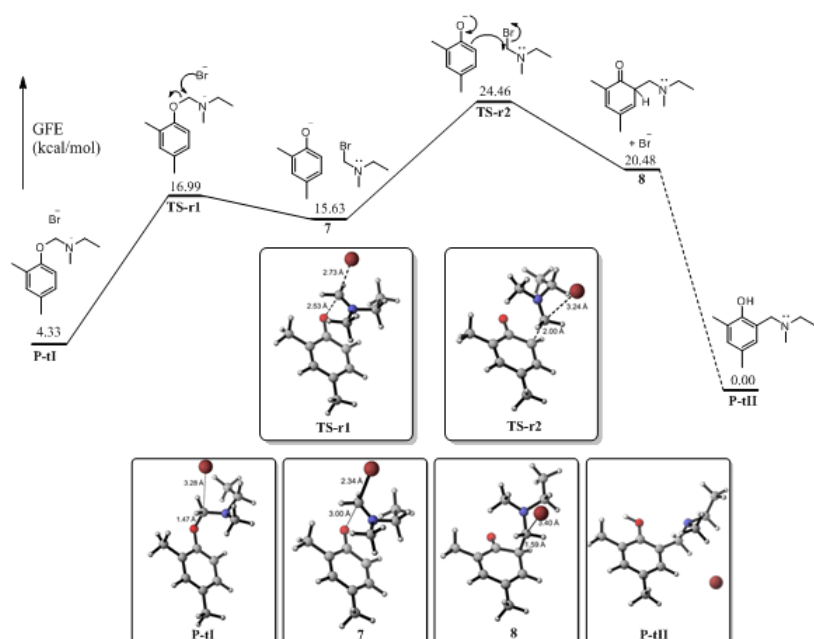


Figure 6.8. Reaction paths and Gibbs free energy barriers for rearrangement mechanism (2011) with the mechanisms for model reactions in Figure 6.7 (M06-2X/6-31+G(d,p) – Gas phase).

able to make a full reaction path including rearrangement mechanisms. All structures are optimized with M06-2X/6-31+G(d,p) in the gas phase. Reaction path including Gibbs free energy barriers is shown in Figure 6.8. Thermodynamically stable Type II product (P-tII) is obtained starting from the Type I product (P-tI).

6.4. Conclusions and Future Work

In this study the aim was to model the cationic ring-opening polymerization of pC-m, 24DMP-m, 235TMP-m and 345TMP-m monomers. For the chain propagation step, both Type I and Type II propagation mechanisms giving phenoxy and phenolic type products, respectively were modeled. Thermodynamically the most stable product obtained by polymerization of pC-m was phenolic (Type II) as detected experimentally. However, computed Gibbs free energy barriers for phenoxy (Type I) and phenolic (Type II) type mechanisms revealed that Type I barrier was lower than Type II barrier. So, modeling some rearrangement steps from phenoxy product to phenolic

should be possible. For this purpose, a bromine anion was used as a nucleophile initiating the rearrangement mechanism with the help of catalysis at room temperature. Rearrangement path is completed with a model system in the gas phase. However, in order to draw a conclusion on whether this path has low enough barrier that can pass through the phenoxy to phenolic product without exceeding the TS2 barrier, the whole path should be re-modeled with the benzoxazine derivatives in solution. CPCM calculations with the realistic models for the rearrangement mechanism in the presence of catalyst are currently in progress.

After completing the rearrangement mechanism in the presence of catalyst, the catalyst will be removed and the rearrangement mechanism at high temperatures (150-200°C) will be investigated, too. Ring-opening and chain propagation for 24DMP-m, 235TMP-m and 345TMP-m monomers will also be modeled to investigate their different behaviour compared to pC-m, since these monomers give phenoxy (24DMP-m and 235 TMP-m) or mixed (345TMP-m) type products. On the other hand, ring protonation may occur at the nitrogen atom instead of oxygen atom. Ring-opening and further chain propagation after protonation at nitrogen will be investigated, too.

7. CONCLUDING REMARKS

This dissertation presents examples of modeling the solvent effect and catalysis in the free-radical polymerization kinetics, polymer morphology and cationic ring-opening polymerization kinetics. Our calculations on the solvent effect on the homopolymerization and copolymerization of ST/HEMA copolymer system revealed the importance of noncovalent interactions like H-bonding within the monomers or with the solvent as well as the solvent dependence of polymerization reactions. The results highlighted that intramolecular interactions in bulk and nonpolar media are replaced with intermolecular H-bonding interactions between HEMA and polar solvent in DMF, giving rise to the rate reduction and reduced HEMA fraction in the ST/HEMA copolymer system. The procedure followed in this study is proposed as a reliable method to investigate solvent effects in similar systems in future studies.

We provided molecular level insight to the effect of Lewis acid contribution on the free-radical polymerization kinetics of DMAM and on the stereoselectivity of the propagating chain. The results revealed that the Lewis acid bridging between the monomer and the terminal unit is the preferred path increasing the isotactic specificity for the pro-*meso* propagation. In the light of the results of this work, reagents activating the monomer while binding to the terminal unit can be chosen to be used in stereocontrolling the propagation in the polymerization of similar types of monomers.

Multi-scale approach used in the investigation of morphological behavior of PIPOX in aqueous solution provided reliable atomistic detail which is in accordance with the experimental data. To the best of our knowledge, this is the first study in the literature which reveals the presence of helical chains above T_c . The results introduce the helical conformation stabilized by hydrophobic interactions between the chains as the precursor leading to the crystallization of PIPOX chains in water above T_c .

Finally, the cationic-ring opening polymerization of benzoxazines is studied with DFT. Ring-opening and chain propagation steps with two possible pathways have been

completed with the monomer pC-m and it has been concluded that phenolic type product was thermodynamically more stable than phenoxy type product as detected experimentally. A model rearrangement mechanism giving phenolic type product starting from phenoxy type product was proposed. Also, reaction mechanisms for other benzoxazine monomers having different phenoxy/phenolic product ratios will be modeled. The mechanism of this reaction is still under investigation.

Overall throughout this dissertation, we have addressed several issues such as the solvent effect, the polymer morphology, the kinetics and catalysis in polymerization reactions. The majority of the calculations have been performed with DFT, however molecular dynamics and coarse-grained simulations were used for the polymer morphology analysis. The predictions made on the copolymer composition upon the change in the solvent medium, on the stereoregularity according to the catalysis used in the free radical polymerization, on the crystallinity behavior upon temperature change and the reaction mechanisms of ring-opening polymerization reactions will shed light on the future experimental and modeling studies. Modeling approaches used in this dissertation are advantageous in terms of the investigation of the challenging problems in polymerization reactions by saving the time spent for experiments. The conclusions related with the specific problems are drawn within the relevant chapters.

REFERENCES

1. Ramachandran, K. I., G. Deepa and K. Namboori, *Computational Chemistry and Molecular Modeling: Principles and Applications*, Springer, Berlin, 2008.
2. Cramer, C. J., *Essentials of Computational Chemistry: Theories and Models*, Wiley, Chichester, West Sussex, England ; Hoboken, NJ, 2nd edition, 2004.
3. Parr, R. G. and W. Yang, *Density-Functional Theory of Atoms and Molecules*, Oxford University Press, New York, 1989.
4. Becke, A. D., "A New Mixing of Hartree-Fock and Local Density-Functional Theories", *Journal of Chemical Physics*, Vol. 98, pp. 1372–1377, 1993.
5. Becke, A. D., "Density-Functional Exchange-Energy Approximation with Correct Asymptotic-Behavior", *Physical Review A*, Vol. 38, pp. 3098–3100, 1988.
6. Leach, A. R., *Molecular Modelling: Principles and Applications*, Prentice Hall, New York, 2nd edition, 2001.
7. Lee, C. T., W. T. Yang and R. G. Parr, "Development of the Colle-Salvetti Correlation-Energy Formula into a Functional of the Electron-Density", *Physical Review B*, Vol. 37, pp. 785–789, 1988.
8. Becke, A. D., "Density-Functional Thermochemistry. 3. The Role of Exact Exchange", *Journal of Chemical Physics*, Vol. 98, pp. 5648–5652, 1993.
9. Pauling, L., "The Nature of the Chemical Bond. IV. The Energy of Single Bonds and the Relative Electronegativity of Atoms", *Journal of the American Chemical Society*, Vol. 54, pp. 3570–3582, 1932.
10. Zhao, Y. and D. Truhlar, "The M06 Suite of Density Functionals For Main Group

- Thermochemistry, Thermochemical Kinetics, Noncovalent Interactions, Excited States, and Transition Elements: Two New Functionals and Systematic Testing of Four M06-Class Functionals and 12 Other Functionals”, *Theoretical Chemistry Accounts*, Vol. 120, pp. 215–241, 2008.
11. Jensen, F., *Introduction to Computational Chemistry*, Wiley, Odense, Denmark, 2nd edition, 2007.
 12. Tapia, O. and J. Bertrán, *Solvent Effects and Chemical Reactivity*, Kluwer Academic Publishers, Dordrecht; Boston, 1996.
 13. Tomasi, J., B. Mennucci and R. Cammi, “Quantum Mechanical Continuum Solvation Models”, *Chemical Reviews*, Vol. 105, pp. 2999–3093, 2005.
 14. Cramer, C. J. and D. G. Truhlar, “Implicit Solvation Models: Equilibria, Structure, Spectra, and Dynamics”, *Chemical Reviews*, Vol. 99, pp. 2161–2200, 1999.
 15. Barone, V., M. Cossi and J. Tomasi, “Geometry Optimization of Molecular Structures in Solution by the Polarizable Continuum Model”, *Journal of Computational Chemistry*, Vol. 19, pp. 404–417, 1998.
 16. Barone, V. and M. Cossi, “Quantum Calculation of Molecular Energies and Energy Gradients in Solution by a Conductor Solvent Model”, *Journal of Physical Chemistry A*, Vol. 102, pp. 1995–2001, 1998.
 17. Mennucci, E. C., B. and J. Tomasi, “Evaluation of Solvent Effects in Isotropic and Anisotropic Dielectrics and in Ionic Solutions with a Unified Integral Equation Method: Theoretical Bases, Computational Implementation, and Numerical Applications”, *Journal of Physical Chemistry B*, Vol. 101, pp. 10506–10517, 1997.
 18. Mennucci, B. and J. Tomasi, “Continuum Solvation Models: a New Approach to the Problem of Solute’s Charge Distribution and Cavity Boundaries”, *Journal of Chemical Physics*, Vol. 106, pp. 5151–5158, 1997.

19. Karplus, M. and J. A. McCammon, “Molecular dynamics simulations of biomolecules”, *Nature Structural Biology*, Vol. 9, pp. 646–652, 2002.
20. Alder, B. J. and T. E. Wainwright, “Phase Transition for a Hard Sphere System”, *Journal of Chemical Physics*, Vol. 27, pp. 1208–1209, 1957.
21. Mccammon, J. A., B. R. Gelin and M. Karplus, “Dynamics of Folded Proteins”, *Nature*, Vol. 267, pp. 585–590, 1977.
22. Noon, W., *Molecular Dynamics Simulations of Bio-Fullerene Interfaces*, Phd thesis, 2004.
23. MacKerell, A. D., D. Bashford, M. Bellott, R. L. Dunbrack, J. D. Evanseck, M. J. Field, S. Fischer, J. Gao, H. Guo, S. Ha, D. Joseph-McCarthy, L. Kuchnir, K. Kuczera, F. T. K. Lau, C. Mattos, S. Michnick, T. Ngo, D. T. Nguyen, B. Prodhom, W. E. Reiher, B. Roux, M. Schlenkrich, J. C. Smith, R. Stote, J. Straub, M. Watanabe, J. Wiorkiewicz-Kuczera, D. Yin and M. Karplus, “All-Atom Empirical Potential for Molecular Modeling and Dynamics Studies of Proteins”, *Journal of Physical Chemistry B*, Vol. 102, pp. 3586–3616, 1998.
24. Adcock, S. A. and J. A. McCammon, “Molecular Dynamics: Survey of Methods for Simulating the Activity of Proteins”, *Chemical Reviews*, Vol. 106, No. 5, pp. 1589–1615, 2006.
25. Allen, M. P. and D. J. Tildesley, *Computer Simulation of Liquids*, Oxford University Press, New York, 1987.
26. Sun, H., “COMPASS: An Ab Initio Force-Field Optimized for Condensed-Phase Applications - Overview with Details on Alkane and Benzene Compounds”, *Journal of Physical Chemistry B*, Vol. 102, pp. 7338–7364, 1998.
27. Sun, H., S. J. Mumby, J. R. Maple and A. T. Hagler, “Ab-Initio Calculations on Small-Molecule Analogs of Polycarbonates”, *Journal of Physical Chemistry*,

- Vol. 99, pp. 5873–5882, 1995.
28. Sun, H., “Ab-Initio Calculations and Force-Field Development for Computer-Simulation of Polysilanes”, *Macromolecules*, Vol. 28, pp. 701–712, 1995.
 29. Sun, H., S. J. Mumby, J. R. Maple and A. T. Hagler, “An Ab-Initio Cff93 All-Atom Force-Field for Polycarbonates”, *Journal of the American Chemical Society*, Vol. 116, pp. 2978–2987, 1994.
 30. Sun, H., “Force-Field for Computation of Conformational Energies, Structures, and Vibrational Frequencies of Aromatic Polyesters”, *Journal of Computational Chemistry*, Vol. 15, pp. 752–768, 1994.
 31. Peng, Z. W., C. S. Ewig, M. J. Hwang, M. Waldman and A. T. Hagler, “Derivation of Class II Force Fields .4. Van Der Waals Parameters of Alkali Metal Cations and Halide Anions”, *Journal of Physical Chemistry A*, Vol. 101, pp. 7243–7252, 1997.
 32. Maple, J. R., M. J. Hwang, T. P. Stockfisch and A. T. Hagler, “Derivation of Class-Ii Force-Fields .3. Characterization of a Quantum Force-Field for Alkanes”, *Israel Journal of Chemistry*, Vol. 34, pp. 195–231, 1994.
 33. Maple, J. R., M. J. Hwang, T. P. Stockfisch, U. Dinur, M. Waldman, C. S. Ewig and A. T. Hagler, “Derivation of Class-Ii Force-Fields .1. Methodology and Quantum Force-Field for the Alkyl Functional-Group and Alkane Molecules”, *Journal of Computational Chemistry*, Vol. 15, pp. 162–182, 1994.
 34. Hwang, M. J., T. P. Stockfisch and A. T. Hagler, “Derivation of Class-Ii Force-Fields .2. Derivation and Characterization of a Class-Ii Force-Field, Cff93, for the Alkyl Functional-Group and Alkane Molecules”, *Journal of the American Chemical Society*, Vol. 116, pp. 2515–2525, 1994.
 35. Hoogerbrugge, P. J. and J. M. V. A. Koelman, “Simulating Microscopic Hydro-

- dynamic Phenomena with Dissipative Particle Dynamics”, *Europhysics Letters*, Vol. 19, pp. 155–160, 1992.
36. Espanol, P. and P. Warren, “Statistical-Mechanics of Dissipative Particle Dynamics”, *Europhysics Letters*, Vol. 30, pp. 191–196, 1995.
37. Moeendarbary, E., T. Y. Ng and M. Zangeneh, “Dissipative Particle Dynamics: Introduction, Methodology and Complex Fluid Applications - a Review”, *International Journal of Applied Mechanics*, Vol. 1, pp. 737–763, 2009.
38. Groot, R. D. and P. B. Warren, “Dissipative Particle Dynamics: Bridging the Gap Between Atomistic and Mesoscopic Simulation”, *Journal of Chemical Physics*, Vol. 107, pp. 4423–4435, 1997.
39. Lee, W. J., S. P. Ju, Y. C. Wang and J. G. Chang, “Modeling of Polyethylene and Poly (L-Lactide) Polymer Blends and Diblock Copolymer: Chain Length and Volume Fraction Effects on Structural Arrangement”, *Journal of Chemical Physics*, Vol. 127, p. 064902, 2007.
40. Hildebrand, J. H., *Solubility of Non-electrolytes*, Reinhold publishing corporation, New York, 2nd edition, 1936.
41. Liang, K., M. Dossi, D. Moscatelli and R. A. Hutchinson, “An Investigation of Free-Radical Copolymerization Propagation Kinetics of Styrene and 2-Hydroxyethyl Methacrylate”, *Macromolecules*, Vol. 42, pp. 7736–7744, 2009.
42. Fried, J. R., *Polymer Science Technology*, Prentice Hall, NJ, 2003.
43. Mayo, F. R. and F. M. Lewis, “Copolymerization. I. A Basis for Comparing the Behavior of Monomers in Copolymerization; The Copolymerization of Styrene and Methyl Methacrylate”, *Journal of the American Chemical Society*, Vol. 66, pp. 1594–1601, 1944.

44. Brandrup, J. and E. H. Immergut, *Polymer Handbook*, John Wiley Sons, New York, 3rd edition, 1989.
45. Jenkel, E., *Zeitschrift fur Physikalische Chemie, Abteilung A*, Vol. 24, p. 190, 1942.
46. Turner Alfrey, J. and G. Goldfinger, "The Mechanism of Copolymerization", *The Journal of Chemical Physics*, Vol. 12, pp. 205–209, 1944.
47. Merz, E., T. Alfrey and G. Goldfinger, "Intramolecular Reactions in Vinyl Polymers as a Means of Investigation of the Propagation Step", *Journal of Polymer Science*, Vol. 1, pp. 75–82, 1946.
48. Coote, M. L., T. P. Davis, B. Klumperman and M. J. Monteiro, "A Mechanistic Perspective on Solvent Effects in Free-Radical Copolymerization", *Journal of Macromolecular Science-Reviews in Macromolecular Chemistry and Physics*, Vol. C38, pp. 567–593, 1998.
49. Fukuda, T., Y. D. Ma and H. Inagaki, "Free-Radical Copolymerization .3. Determination of Rate Constants of Propagation and Termination for the Styrene Methyl-Methacrylate System - a Critical Test of Terminal-Model Kinetics", *Macromolecules*, Vol. 18, pp. 17–26, 1985.
50. Fukuda, T., K. Kubo and Y. D. Ma, "Kinetics of Free-Radical Copolymerization", *Progress in Polymer Science*, Vol. 17, pp. 875–916, 1992.
51. ODriscoll, K. F., M. L. Monteiro and B. Klumperman, "The Effect of Benzyl Alcohol on Pulsed Laser Polymerization of Styrene and Methylmethacrylate", *Journal of Polymer Science Part a-Polymer Chemistry*, Vol. 35, pp. 515–520, 1997.
52. Liang, K. and R. A. Hutchinson, "Solvent Effects on Free-Radical Copolymerization Propagation Kinetics of Styrene and Methacrylates", *Macromolecules*,

- Vol. 43, pp. 6311–6320, 2010.
53. Coote, M. L. and T. P. Davis, “The Mechanism of the Propagation Step in Free-Radical Copolymerisation”, *Progress in Polymer Science*, Vol. 24, pp. 1217–1251, 1999.
 54. Coote, M. L., T. P. Davis and L. Radom, “Conformational Dependence of the Penultimate Unit Effect in Free-Radical Copolymerization”, *Macromolecules*, Vol. 32, pp. 5270–5276, 1999.
 55. Coote, M. L., T. P. Davis and L. Radom, “The Effect of Remote Substituents in Free Radical Addition Reactions: New Evidence for the Penultimate Unit Effect”, *Journal of Molecular Structure-Theochem*, Vol. 461, pp. 91–96, 1999.
 56. Coote, M. L., T. P. Davis and L. Radom, “Effect of the Penultimate Unit on Radical Stability and Reactivity in Free-Radical Polymerization”, *Macromolecules*, Vol. 32, pp. 2935–2940, 1999.
 57. Coote, M. L. and T. P. Davis, “Copolymerization Propagation Kinetics of Para-Substituted Styrenes: A Critical Test of the Implicit Penultimate Model”, *Macromolecules*, Vol. 32, pp. 3626–3636, 1999.
 58. Lin, C. Y., M. L. Coote, A. Petit, P. Richard, R. Poli and K. Matyjaszewski, “Ab Initio Study of the Penultimate Effect for the ATRP Activation Step Using Propylene, Methyl Acrylate, and Methyl Methacrylate Monomers”, *Macromolecules*, Vol. 40, pp. 5985–5994, 2007.
 59. Roberts, G. E., M. L. Coote, J. P. A. Heuts, L. M. Morris and T. P. Davis, “Roberts, G. E., M. L. Coote, J. P. A. Heuts, L. M. Morris and T. P. Davis”, *Macromolecules*, Vol. 32, pp. 1332–1340, 1999.
 60. Ito, T. and T. Otsu, “Solvent Effect in Radical Copolymerization of Methyl Methacrylate with Styrene”, *Journal of Macromolecular Science: Part A - Chem-*

istry, Vol. 3, p. 197, 1969.

61. Harwood, H. J., "Structures and Compositions of Copolymers", *Makromolekulare Chemie-Macromolecular Symposia*, Vol. 10, pp. 331–354, 1987.
62. Klumperman, B. and K. F. Odriscoll, "Interpreting the Copolymerization of Styrene with Maleic-Anhydride and with Methyl-Methacrylate in Terms of the Bootstrap Model", *Polymer*, Vol. 34, pp. 1032–1037, 1993.
63. Beuermann, S. and M. Buback, "Rate Coefficients of Free-Radical Polymerization Deduced from Pulsed Laser Experiments", *Progress in Polymer Science*, Vol. 27, pp. 191–254, 2002.
64. Yee, L. H., M. L. Coote, R. P. Chaplin and T. P. Davis, "Determination of Propagation Rate Coefficients for an Alpha-Substituted Acrylic Ester: Pulsed Laser Polymerization of Dimethyl Itaconate", *Journal of Polymer Science Part a-Polymer Chemistry*, Vol. 38, pp. 2192–2200, 2000.
65. Hutchinson, R. A., D. A. Paquet, J. H. McMinn and R. E. Fuller, "Measurement of Free-Radical Propagation Rate Coefficients for Ethyl, Butyl, and Isobutyl Methacrylates by Pulsed-Laser Polymerization", *Macromolecules*, Vol. 28, pp. 4023–4028, 1995.
66. Buback, M., R. G. Gilbert, R. A. Hutchinson, B. Klumperman, F. D. Kuchta, B. G. Manders, K. F. Odriscoll, G. T. Russell and J. Schweer, "Critically Evaluated Rate Coefficients for Free-Radical Polymerization. 1. Propagation Rate Coefficient for Styrene", *Macromolecular Chemistry and Physics*, Vol. 196, pp. 3267–3280, 1995.
67. Sarnecki, J. and J. Schweer, "Conditions for the Determination of Precise and Accurate Free-Radical Propagation Rate Coefficients from Pulsed-Laser-Made Polymer", *Macromolecules*, Vol. 28, pp. 4080–4088, 1995.

68. Bergert, U., S. Beuermann, M. Buback, C. H. Kurz, G. T. Russell and C. Schmaltz, "Effect of Photoinitiator on the Molar-Mass Distribution Obtained from a Pulsed-Laser Polymerization", *Macromolecular Rapid Communications*, Vol. 16, pp. 425–434, 1995.
69. Coote, M. L. and T. P. Davis, "Propagation Rate Coefficients for Styrene Solution Polymerization in Dimethyl Formamide and Acetonitrile", *European Polymer Journal*, Vol. 36, pp. 2423–2427, 2000.
70. Beuermann, S., D. A. Paquet, J. H. McMinn and R. A. Hutchinson, "Propagation Kinetics of Methacrylic Acid Studied by Pulsed-Laser Polymerization", *Macromolecules*, Vol. 30, pp. 194–197, 1997.
71. Kuchta, F. D., A. M. van Herk and A. L. German, "Propagation Kinetics of Acrylic and Methacrylic Acid in Water and Organic Solvents Studied by Pulsed-Laser Polymerization", *Macromolecules*, Vol. 33, pp. 3641–3649, 2000.
72. Zammit, M. D., T. P. Davis, G. D. Willett and K. F. O'Driscoll, "The Effect of Solvent on the Homopolymerization Rate Coefficients of Styrene and Methyl Methacrylate", *Journal of Polymer Science Part A-Polymer Chemistry*, Vol. 35, pp. 2311–2321, 1997.
73. Beuermann, S., M. Buback, P. Hesse, S. Kukuckova and I. Lacik, "Propagation Kinetics of Free-Radical Methacrylic Acid Polymerization in Aqueous Solution. The Effect of Concentration and Degree of Ionization", *Macromolecular Symposia*, Vol. 248, pp. 23–32, 2007.
74. Beuermann, S., M. Buback, P. Hesse, S. Kukuckova and I. Lacik, "Propagation Rate Coefficient of Non-Ionized Methacrylic Acid Radical Polymerization in Aqueous Solution. The Effect of Monomer Conversion", *Macromolecular Symposia*, Vol. 248, pp. 41–49, 2007.
75. Beuermann, S., M. Buback, P. Hesse and I. Lacik, "Free-Radical Propagation

- Rate Coefficient of Nonionized Methacrylic Acid in Aqueous Solution from Low Monomer Concentrations to Bulk Polymerization”, *Macromolecules*, Vol. 39, pp. 184–193, 2006.
76. Lacik, I., S. Beuermann and M. Buback, “Aqueous Phase Size-Exclusion-Chromatography Used for PLP-SEC Studies into Free-Radical Propagation Rate of Acrylic Acid in Aqueous Solution”, *Macromolecules*, Vol. 34, pp. 6224–6228, 2001.
77. Lacik, I., S. Beuermann and M. Buback, “PLP-SEC Study into Free-Radical Propagation Rate of Nonionized Acrylic Acid in Aqueous Solution”, *Macromolecules*, Vol. 36, pp. 9355–9363, 2003.
78. Ganachaud, F., R. Balic, M. J. Monteiro and R. G. Gilbert, “Propagation Rate Coefficient of Poly(N-Isopropylacrylamide) in Water Below its Lower Critical Solution Temperature”, *Macromolecules*, Vol. 33, pp. 8589–8596, 2000.
79. Seabrook, S. A., M. P. Tonge and R. G. Gilbert, “Pulsed Laser Polymerization Study of the Propagation Kinetics of Acrylamide in Water”, *Journal of Polymer Science Part a-Polymer Chemistry*, Vol. 43, pp. 1357–1368, 2005.
80. Laidler, K. J. and M. C. King, “The Development of Transition-State Theory”, *Journal of Physical Chemistry*, Vol. 87, pp. 2657–2664, 1983.
81. Truhlar, D. G., W. L. Hase and J. T. Hynes, “Current Status of Transition-State Theory”, *Journal of Physical Chemistry*, Vol. 87, pp. 2664–2682, 1983.
82. Truhlar, D. G., B. C. Garrett and S. J. Klippenstein, “Current Status of Transition-State Theory”, *Journal of Physical Chemistry*, Vol. 100, pp. 12771–12800, 1996.
83. Dossi, M., G. Storti and D. Moscatelli, “A Quantum Chemistry Study of the Free-Radical Copolymerization Propagation Kinetics of Styrene and 2-Hydroxyethyl

- Acrylate”, *Polymer Engineering and Science*, Vol. 51, pp. 2109–2114, 2011.
84. Dossi, M., K. Liang, R. A. Hutchinson and D. Moscatelli, “Investigation of Free-Radical Copolymerization Propagation Kinetics of Vinyl Acetate and Methyl Methacrylate”, *Journal of Physical Chemistry B*, Vol. 114, pp. 4213–4222, 2010.
 85. Coote, M. L., “Quantum-Chemical Modeling of Free-Radical Polymerization”, *Macromolecular Theory and Simulations*, Vol. 18, pp. 388–400, 2009.
 86. Van Speybroeck, V., K. Van Cauter, B. Coussens and M. Waroquier, “Ab Initio Study of Free-Radical Polymerizations: Cost-Effective Methods to Determine the Reaction Rates”, *Chemphyschem*, Vol. 6, pp. 180–189, 2005.
 87. Cieplak, P. and A. Kaim, “Theoretical Study of the Free-Radical Copolymerization of Styrene with Methyl Methacrylate: Comparative Study to the Styrene-Acrylonitrile Monomer System”, *Journal of Polymer Science Part a-Polymer Chemistry*, Vol. 42, pp. 1557–1565, 2004.
 88. Dogan, B., S. Catak, V. Van Speybroeck, M. Waroquier and V. Aviyente, “Free Radical Polymerization of Ethyl Methacrylate and Ethyl Alpha-Hydroxy Methacrylate: A Computational Approach to the Propagation Kinetics”, *Polymer*, Vol. 53, pp. 3211–3219, 2012.
 89. Furuncuoglu, T., I. Ugur, I. Degirmenci and V. Aviyente, “Role of Chain Transfer Agents in Free Radical Polymerization Kinetics”, *Macromolecules*, Vol. 43, pp. 1823–1835, 2010.
 90. Degirmenci, I., V. Aviyente, V. Van Speybroeck and M. Waroquier, “DFT Study on the Propagation Kinetics of Free-Radical Polymerization of alpha-Substituted Acrylates”, *Macromolecules*, Vol. 42, pp. 3033–3041, 2009.
 91. Ozaltin, T. F., I. Degirmenci, V. Aviyente, C. Atilgan, B. De Sterck, V. Van Speybroeck and M. Waroquier, “Controlling the Tacticity in the Polymerization of N-

- Isopropylacrylamide: A Computational Study”, *Polymer*, Vol. 52, pp. 5503–5512, 2011.
92. Thickett, S. C. and R. G. Gilbert, “Propagation Rate Coefficient of Acrylic Acid: Theoretical Investigation of the Solvent Effect”, *Polymer*, Vol. 45, pp. 6993–6999, 2004.
93. Miertus, S., E. Scrocco and J. Tomasi, “Electrostatic Interaction of a Solute with a Continuum - a Direct Utilization of Abinitio Molecular Potentials for the Prevision of Solvent Effects”, *Chemical Physics*, Vol. 55, pp. 117–129, 1981.
94. Miertus, S. and J. Tomasi, “Approximate Evaluations of the Electrostatic Free-Energy and Internal Energy Changes in Solution Processes”, *Chemical Physics*, Vol. 65, pp. 239–245, 1982.
95. Izgorodina, E. I. and M. L. Coote, “Accurate Ab Initio Prediction of Propagation Rate Coefficients in Free-Radical Polymerization: Acrylonitrile and Vinyl Chloride”, *Chemical Physics*, Vol. 324, pp. 96–110, 2006.
96. Klamt, A. and G. Schuurmann, “Cosmo - a New Approach to Dielectric Screening in Solvents with Explicit Expressions for the Screening Energy and Its Gradient”, *Journal of the Chemical Society-Perkin Transactions 2*, pp. 799–805, 1993.
97. Klamt, A., “Conductor-Like Screening Model for Real Solvents - a New Approach to the Quantitative Calculation of Solvation Phenomena”, *Journal of Physical Chemistry*, Vol. 99, pp. 2224–2235, 1995.
98. Klamt, A., *COSMO-RS : From Quantum Chemistry to Fluid Phase Thermodynamics and Drug Design*, Elsevier, Oxford, 2005.
99. Klamt, A., V. Jonas, T. Burger and J. C. W. Lohrenz, “Refinement and Parametrization of COSMO-RS”, *Journal of Physical Chemistry A*, Vol. 102, pp. 5074–5085, 1998.

100. Degirmenci, I., D. Avci, V. Aviyente, K. Van Cauwer, V. Van Speybroeck and M. Waroquier, "Density Functional Theory Study of Free-Radical Polymerization of Acrylates and Methacrylates: Structure-Reactivity Relationship", *Macromolecules*, Vol. 40, pp. 9590–9602, 2007.
101. Alfrey, T., "Mechanical-Properties", *Abstracts of Papers of the American Chemical Society*, p. 36, 1976.
102. Lin, C. Y., E. I. Izgorodina and M. L. Coote, "First Principles Prediction of The Propagation Rate Coefficients of Acrylic and Vinyl Esters: Are We There Yet?", *Macromolecules*, Vol. 43, pp. 553–560, 2010.
103. Matyjaszewski, K. and T. P. Davis, *Handbook of Radical Polymerization*, Wiley-Interscience, Hoboken, 2002.
104. McQuarrie, D. A. and J. D. Simon, *Physical Chemistry : A Molecular Approach*, University Science Books, Sausalito, 1997.
105. Atkins, P. W. and J. D. Paula, *Atkins' Physical Chemistry*, Oxford University Press, New York, 8th edition, 2006.
106. Frisch, R., *Gaussian09*, Gaussian, Inc., 2009.
107. Louwen, J. N. P. and E. V. Lenthe, *Theoretical Chemistry*, Vrije Universiteit: Amsterdam, The Netherlands, 2008.
108. Liptak, M. D., K. C. Gross, P. G. Seybold, S. Feldgus and G. C. Shields, "Absolute pK(a) Determinations for Substituted Phenols", *Journal of the American Chemical Society*, Vol. 124, pp. 6421–6427, 2002.
109. Alfrey, T., F. J. Honn and H. Mark, "Preparation, Purification, and Polymerization of Diethyl Silicon Dichloride", *Journal of Polymer Science*, Vol. 1, pp. 102–120, 1946.

110. Alfrey, T. and C. C. Price, “Relative Reactivities in Vinyl Copolymerization”, *Journal of Polymer Science*, Vol. 2, pp. 101–106, 1947.
111. Moad, G. and D. H. Solomon, *The Chemistry of Radical Polymerization*, Elsevier, Oxford, 2nd edition, 2006.
112. Kamigaito, M. and K. Satoh, “Stereospecific Living Radical Polymerization for Simultaneous Control of Molecular Weight and Tacticity”, *Journal of Polymer Science Part a-Polymer Chemistry*, Vol. 44, pp. 6147–6158, 2006.
113. Odian, G. G., *Principles of Polymerization*, Wiley, New York, 3rd edition, 1991.
114. Soldera, A., “Comparison between the Glass Transition Temperatures of the Two PMMA Tacticities: A Molecular Dynamics Simulation Point of View”, *Macromolecular Symposia*, Vol. 133, pp. 21–32, 1998.
115. Wu, C. F., “Multiscale Simulations of the Structure and Dynamics of Stereoregular Poly(Methyl Methacrylate)s”, *Journal of Molecular Modeling*, Vol. 20, pp. 121–126, 2014.
116. Zhao, H. Y., Z. N. Yu, F. Begum, R. C. Hedden and S. L. Simon, “The Effect of Nanoconfinement on Methyl Methacrylate Polymerization: T-G, Molecular Weight, and Tacticity”, *Polymer*, Vol. 55, pp. 4959–4965, 2014.
117. Sitar, S., V. Aseyev and K. Kogej, “Differences in Association Behavior of Isotactic and Atactic Poly(Methacrylic Acid)”, *Polymer*, Vol. 55, pp. 848–854, 2014.
118. Horinouchi, A. and K. Tanaka, “An Effect of Stereoregularity on the Structure of Poly(Methyl Methacrylate) at Air and Water Interfaces”, *Rsc Advances*, Vol. 3, pp. 9446–9452, 2013.
119. Nishi, K., T. Hiroi, K. Hashimoto, K. Fujii, Y. S. Han, T. H. Kim, Y. Katsumoto and M. Shibayama, “SANS and DLS Study of Tacticity Effects on Hydrophobicity

- and Phase Separation of Poly(N-isopropylacrylamide)”, *Macromolecules*, Vol. 46, pp. 6225–6232, 2013.
120. Katsumoto, N. K., Y. and T. Miyata, “Molecular Approach To Understand the Tacticity Effects on the Hydrophilicity of Poly(N-isopropylacrylamide): Solubility of Dimer Model Compounds in Water”, *Journal of Physical Chemistry B*, Vol. 114, pp. 13312–13318, 2010.
121. Autieri, E., E. Chiessi, A. Lonardi, G. Paradossi and M. Sega, “Conformation and Dynamics of Poly(N-isopropyl acrylamide) Trimers in Water: A Molecular Dynamics and Metadynamics Simulation Study”, *Journal of Physical Chemistry B*, Vol. 115, pp. 5827–5839, 2011.
122. Satoh, K. and M. Kamigaito, “Stereospecific Living Radical Polymerization: Dual Control of Chain Length and Tacticity for Precision Polymer Synthesis”, *Chemical Reviews*, Vol. 109, pp. 5120–5156, 2009.
123. Imoto, M., T. Otsu and S. Shimizu, “Vinyl Polymerization. 66. The Effect of Zinc Chloride on the Radical Polymerization of Vinyl Monomers”, *Makromolekulare Chemie*, Vol. 65, pp. 174–179, 1963.
124. Imoto, M., T. Otsu and Y. Harada, “Vinyl Polymerization. 68. The Polymerization of Methyl Methacrylate in the Presence of Zinc Chloride”, *Makromolekulare Chemie*, Vol. 65, pp. 180–193, 1963.
125. Imoto, M., T. Otsu, B. Yamada and A. Shimizu, “Further Results on Effect of Zinc Chloride in Copolymerization of Methyl Methacrylate or Acrylonitrile with Some Butenes or Allylic Compounds”, *Makromolekulare Chemie*, Vol. 82, pp. 277–278, 1965.
126. Matsumoto, A. and S. Nakamura, “Radical Polymerization of Methyl Methacrylate in the Presence of Magnesium Bromide as the Lewis Acid”, *Journal of Applied Polymer Science*, Vol. 74, pp. 290–296, 1999.

127. Habaue, S., H. Baraki and Y. Okamoto, "Catalytic Stereocontrol by Scandium Trifluoromethanesulfonate in Radical Polymerization of Alpha-(Alkoxyethyl)Acrylates", *Polymer Journal*, Vol. 32, pp. 1017–1021, 2000.
128. Isobe, Y., T. Nakano and Y. Okamoto, "Stereocontrol During the Free-Radical Polymerization of Methacrylates with Lewis Acids", *Journal of Polymer Science Part a-Polymer Chemistry*, Vol. 39, pp. 1463–1471, 2001.
129. Jiang, J. G., X. Y. Lu and Y. Lu, "Stereospecific Preparation of Polyacrylamide with Low Polydispersity by ATRP in the Presence of Lewis Acid", *Polymer*, Vol. 49, pp. 1770–1776, 2008.
130. Isobe, Y., D. Fujioka, S. Habaue and Y. Okamoto, "Efficient Lewis Acid-Catalyzed Stereocontrolled Radical Polymerization of Acrylamides", *Journal of the American Chemical Society*, Vol. 123, pp. 7180–7181, 2001.
131. Habaue, S., Y. Isobe and Y. Okamoto, "Stereocontrolled Radical Polymerization of Acrylamides and Methacrylamides using Lewis Acids", *Tetrahedron*, Vol. 58, pp. 8205–8209, 2002.
132. Isobe, Y., Y. Suito, S. Habaue and Y. Okamoto, "Stereocontrol During the Free-Radical Polymerization of Methacrylamides in the Presence of Lewis Acids", *Journal of Polymer Science Part a-Polymer Chemistry*, Vol. 41, pp. 1027–1033, 2003.
133. Suito, Y., Y. Isobe, S. Habaue and Y. Okamoto, "Isotactic-specific Radical Polymerization of Methacrylamides in the Presence of Lewis Acids", *Journal of Polymer Science Part a-Polymer Chemistry*, Vol. 40, pp. 2496–2500, 2002.
134. Yakimansky, A. V. and A. H. E. Muller, "Quantum-Chemical Study of the Effect of Triethylaluminum on the Chain-End Structure and Tacticity of Poly(N,N-Dimethylacrylamide) with Lithium Counterion in THF", *Macromolecules*, Vol. 39, pp. 4228–4234, 2006.

135. Xu, X., S. Feng, Y. Zhu, H. Li, X. Shen, C. Zhang, J. Bai and L. Zhang, “Stereospecific Radical Polymerization of Optically Active (S)-N-(2-Hydroxy-1-Phenylethyl) Methacrylamide Catalyzed by Lewis Acids”, *European Polymer Journal*, Vol. 49, pp. 3673–3680, 2013.
136. Hirano, T., T. Saito, Y. Kurano, Y. Miwa, M. Oshimura and K. Ute, “Dual Role for Alkali Metal Cations in Enhancing the Low-Temperature Radical Polymerization of N,N-Dimethylacrylamide”, *Polymer Chemistry*, Vol. 6, pp. 2054–2064, 2015.
137. Jiang, Z. M., Z. Q. Su, L. Li, K. Zhang and G. S. Huang, “Antiaging Mechanism for Partly Crosslinked Polyacrylamide in Saline Solution under High-Temperature and High-Salinity Conditions”, *Journal of Macromolecular Science Part B-Physics*, Vol. 52, pp. 113–126, 2013.
138. Triftaridou, A. I., F. Checot and I. Iliopoulos, “Poly(N,N-dimethylacrylamide)-block-Poly(L-lysine) Hybrid Block Copolymers: Synthesis and Aqueous Solution Characterization”, *Macromolecular Chemistry and Physics*, Vol. 211, pp. 768–777, 2010.
139. Kalogianni, A., E. Pefkianakis, A. Stefopoulos, G. Bokias and J. K. Kallitsis, “pH-Responsive Photoluminescence Properties of a Water-Soluble Copolymer Containing Quinoline Groups in Aqueous Solution”, *Journal of Polymer Science Part B-Polymer Physics*, Vol. 48, pp. 2078–2083, 2010.
140. De Lusancay, G. C., S. Norvez and I. Iliopoulos, “Temperature-Controlled Release of Catechol Dye in Thermosensitive Phenylboronate-Containing Copolymers: A Quantitative Study”, *European Polymer Journal*, Vol. 46, pp. 1367–1373, 2010.
141. Degirmenci, I., S. Eren, V. Aviyente, B. De Sterck, K. Hemelsoet, V. Van Speybroeck and M. Waroquier, “Modeling the Solvent Effect on the Tacticity in the Free Radical Polymerization of Methyl Methacrylate”, *Macromolecules*, Vol. 43, pp. 5602–5610, 2010.

142. Noble, B. B., L. M. Smith and M. L. Coote, “The Effect of LiNTf₂ on the Propagation Rate Coefficient of Methyl Methacrylate”, *Polymer Chemistry*, Vol. 5, pp. 4974–4983, 2014.
143. Zhang, G. Z., I. A. Konstantinov, S. G. Arturo, D. C. Yu and L. J. Broadbelt, “Assessment of a Cost-Effective Approach to the Calculation of Kinetic and Thermodynamic Properties of Methyl Methacrylate Homopolymerization: A Comprehensive Theoretical Study”, *Journal of Chemical Theory and Computation*, Vol. 10, pp. 5668–5676, 2014.
144. Gonzalez, C. and H. B. Schlegel, “An Improved Algorithm for Reaction-Path Following”, *Journal of Chemical Physics*, Vol. 90, pp. 2154–2161, 1989.
145. Gonzalez, C. and H. B. Schlegel, “Reaction-Path Following in Mass-Weighted Internal Coordinates”, *Journal of Physical Chemistry*, Vol. 94, No. 14, pp. 5523–5527, 1990.
146. De Sterck, B., R. Vaneerdeweg, F. Du Prez, M. Waroquier and V. Van Speybroeck, “Solvent Effects on Free Radical Polymerization Reactions: The Influence of Water on the Propagation Rate of Acrylamide and Methacrylamide”, *Macromolecules*, Vol. 43, pp. 827–836, 2010.
147. Baraki, H., S. Habaue and Y. Okamoto, “Stereospecific Radical Polymerization of Alpha-(Alkoxyethyl)Acrylates Controlled by Lewis Acid Catalysts: Mechanistic Study and Effect of Amino Alcohols as Ligand for Zinc Bromide”, *Macromolecules*, Vol. 34, pp. 4724–4729, 2001.
148. Dimitrov, I., B. Trzebicka, A. H. E. Muller, A. Dworak and C. B. Tsvetanov, “Thermosensitive Water-Soluble Copolymers with Doubly Responsive Reversibly Interacting Entities”, *Progress in Polymer Science*, Vol. 32, pp. 1275–1343, 2007.
149. Gil, E. S. and S. M. Hudson, “Stimuli-Responsive Polymers and their Bioconjugates”, *Progress in Polymer Science*, Vol. 29, pp. 1173–1222, 2004.

150. Luxenhofer, R., G. Sahay, A. Schulz, D. Alakhova, T. K. Bronich, R. Jordan and A. V. Kabanov, "Structure-Property Relationship in Cytotoxicity and Cell Uptake of Poly(2-Oxazoline) Amphiphiles", *Journal of Controlled Release*, Vol. 153, pp. 73–82, 2011.
151. Bloksma, M. M., D. J. Bakker, C. Weber, R. Hoogenboom and U. S. Schubert, "The Effect of Hofmeister Salts on the LCST Transition of Poly(2-oxazoline)s with Varying Hydrophilicity", *Macromolecular Rapid Communications*, Vol. 31, pp. 724–728, 2010.
152. Diehl, C. and H. Schlaad, "Thermo-Responsive Polyoxazolines with Widely Tunable LCST", *Macromolecular Bioscience*, Vol. 9, pp. 157–161, 2009.
153. Huber, S. and R. Jordan, "Modulation of the Lower Critical Solution Temperature of 2-Alkyl-2-Oxazoline Copolymers", *Colloid and Polymer Science*, Vol. 286, pp. 395–402, 2008.
154. Huber, S., N. Hutter and R. Jordan, "Effect of End Group Polarity Upon the Lower Critical Solution Temperature of Poly(2-Isopropyl-2-Oxazoline)", *Colloid and Polymer Science*, Vol. 286, pp. 1653–1661, 2008.
155. Demirel, A. L., P. T. Guner, B. Verbraeken, H. Schlaad, U. S. Schubert and R. Hoogenboom, "Revisiting the Crystallization of Poly(2-alkyl-2-oxazoline)s", *Journal of Polymer Science Part B-Polymer Physics*, Vol. 54, pp. 721–729, 2016.
156. Litt, M., F. Rahl and L. G. Roldan, "Polymerization of Cyclic Imino Ethers. 6. X-Ray Study of Some Polyaziridines", *Journal of Polymer Science Part a-2-Polymer Physics*, Vol. 7, pp. 463–473, 1969.
157. Guner, P. T. and A. L. Demirel, "Effect of Anions on the Cloud Point Temperature of Aqueous Poly(2-ethyl-2-oxazoline) Solutions", *Journal of Physical Chemistry B*, Vol. 116, pp. 14510–14514, 2012.

158. Guner, P. T., A. Miko, F. F. Schweinberger and A. L. Demirel, "Self-Assembled Poly(2-Ethyl-2-Oxazoline) Fibers in Aqueous Solutions", *Polymer Chemistry*, Vol. 3, pp. 322–324, 2012.
159. Diehl, C., I. Dambowsky, R. Hoogenboom and H. Schlaad, "Self-Assembly of Poly(2-alkyl-2-oxazoline)s by Crystallization in Ethanol-Water Mixtures Below the Upper Critical Solution Temperature", *Macromolecular Rapid Communications*, Vol. 32, pp. 1753–1758, 2011.
160. Erel, I., H. Schlaad and A. L. Demirel, "Effect of Structural Isomerism and Polymer End Group on the Ph-Stability of Hydrogen-Bonded Multilayers", *Journal of Colloid and Interface Science*, Vol. 361, pp. 477–482, 2011.
161. Obeid, R., E. Maltseva, A. F. Thunemann, F. Tanaka and F. M. Winnik, "Temperature Response of Self-Assembled Micelles of Telechelic Hydrophobically Modified Poly(2-alkyl-2-oxazoline)s in Water", *Macromolecules*, Vol. 42, pp. 2204–2214, 2009.
162. Demirel, A. L., M. Meyer and H. Schlaad, "Formation of Polyamide Nanofibers by Directional Crystallization in Aqueous Solution", *Angewandte Chemie-International Edition*, Vol. 46, pp. 8622–8624, 2007.
163. Oleszko, N., A. Utrata-Wesolek, W. Walach, M. Libera, A. Hercog, U. Szeluga, M. Domanski, B. Trzebicka and A. Dworak, "Crystallization of Poly(2-isopropyl-2-oxazoline) in Organic Solutions", *Macromolecules*, Vol. 48, pp. 1852–1859, 2015.
164. Zhao, J., R. Hoogenboom, G. Van Assche and B. Van Mele, "Demixing and Remixing Kinetics of Poly(2-isopropyl-2-oxazoline) (PIPOZ) Aqueous Solutions Studied by Modulated Temperature Differential Scanning Calorimetry", *Macromolecules*, Vol. 43, pp. 6853–6860, 2010.
165. Diehl, C., P. Cernoch, I. Zenke, H. Runge, R. Pitschke, J. Hartmann, B. Tiersch and H. Schlaad, "Mechanistic Study of the Phase Separation/Crystallization

- Process of Poly(2-Isopropyl-2-Oxazoline) in Hot Water”, *Soft Matter*, Vol. 6, pp. 3784–3788, 2010.
166. Katsumoto, Y., A. Tsuchiizu, X. P. Qiu and F. M. Winnik, “Dissecting the Mechanism of the Heat-Induced Phase Separation and Crystallization of Poly(2-isopropyl-2-oxazoline) in Water through Vibrational Spectroscopy and Molecular Orbital Calculations”, *Macromolecules*, Vol. 45, pp. 3531–3541, 2012.
167. Li, T. J., H. Tang and P. Y. Wu, “Molecular Evolution of Poly(2-isopropyl-2-oxazoline) Aqueous Solution during the Liquid-Liquid Phase Separation and Phase Transition Process”, *Langmuir*, Vol. 31, pp. 6870–6878, 2015.
168. Sun, S. T. and P. Y. Wu, “Conformational Changes in the Heat-Induced Crystallization of Poly(2-Isopropyl-2-Oxazoline) in the Solid State”, *Physical Chemistry Chemical Physics*, Vol. 17, pp. 31084–31092, 2015.
169. An, J. X., X. Y. Liu, P. Linse, A. Dedinaite, F. M. Winnik and P. M. Claesson, “Tethered Poly(2-isopropyl-2-oxazoline) Chains: Temperature Effects on Layer Structure and Interactions Probed by AFM Experiments and Modeling”, *Langmuir*, Vol. 31, pp. 3039–3048, 2015.
170. Kirmizialtin, S., Y. Z. Menceloglu and C. Baysal, “New Surfactants Design for CO₂ Applications: Molecular Dynamics Simulations of Fluorocarbon-Hydrocarbon Oligomers”, *Journal of Chemical Physics*, Vol. 119, pp. 4953–4961, 2003.
171. Klein, M. L. and W. Shinoda, “Large-Scale Molecular Dynamics Simulations of Self-Assembling Systems”, *Science*, Vol. 321, pp. 798–800, 2008.
172. Spyriouni, T., C. Tzoumanekas, D. Theodorou, F. Muller-Plathe and G. Milano, “Coarse-Grained and Reverse-Mapped United-Atom Simulations of Long-Chain Atactic Polystyrene Melts: Structure, Thermodynamic Properties, Chain Conformation, and Entanglements”, *Macromolecules*, Vol. 40, pp. 3876–3885, 2007.

173. Maly, M., P. Posocco, S. Pricl and M. Fermeglia, “Self-Assembly of Nanoparticle Mixtures in Diblock Copolymers: Multiscale Molecular Modeling”, *Industrial Engineering Chemistry Research*, Vol. 47, pp. 5023–5038, 2008.
174. Harmandaris, V. A., D. Reith, N. F. A. Van der Vegt and K. Kremer, “Comparison between Coarse-Graining Models for Polymer Systems: Two Mapping Schemes for Polystyrene”, *Macromolecular Chemistry and Physics*, Vol. 208, pp. 2109–2120, 2007.
175. Groot, R. D. and T. J. Madden, “Dynamic Simulation of Diblock Copolymer Microphase Separation”, *Journal of Chemical Physics*, Vol. 108, pp. 8713–8724, 1998.
176. Praprotnik, M., C. Junghans, L. Delle Site and K. Kremer, “Simulation Approaches to Soft Matter: Generic Statistical Properties vs. Chemical Details”, *Computer Physics Communications*, Vol. 179, pp. 51–60, 2008.
177. Maiti, A. and S. McGrother, “Bead-Bead Interaction Parameters in Dissipative Particle Dynamics: Relation to Bead-Size, Solubility Parameter, and Surface Tension”, *Journal of Chemical Physics*, Vol. 120, pp. 1594–1601, 2004.
178. Koelman, J. M. V. A. and P. J. Hoogerbrugge, “Dynamic Simulations of Hard-Sphere Suspensions under Steady Shear”, *Europhysics Letters*, Vol. 21, pp. 363–368, 1993.
179. Ozen, A. S., U. Sen and C. Atilgan, “Complete Mapping of the Morphologies of Some Linear and Graft Fluorinated Co-Oligomers in an Aprotic Solvent by Dissipative Particle Dynamics”, *Journal of Chemical Physics*, Vol. 124, p. 064905, 2006.
180. Can, H., G. Kacar and C. Atilgan, “Surfactant Formation Efficiency of Fluorocarbon-Hydrocarbon Oligomers in Supercritical CO₂”, *Journal of Chemical Physics*, Vol. 131, p. 124701, 2009.

181. Teraoka, I., *Polymer Solutions : An Introduction to Physical Properties*, Wiley, New York, 2002.
182. Jones, R. A. L., *Soft Condensed Matter*, Oxford University Press, Oxford ; New York, 2002.
183. Jones, R. A. L. and R. W. Richards, *Polymers at Surfaces and Interfaces*, Cambridge University Press, Cambridge ; New York, 1999.
184. Kacar, G., C. Atilgan and A. S. Ozen, “Mapping and Reverse-Mapping of the Morphologies for a Molecular Understanding of the Self-Assembly of Fluorinated Block Copolymers”, *Journal of Physical Chemistry C*, Vol. 114, pp. 370–382, 2010.
185. Harmandaris, V. A., N. P. Adhikari, N. F. A. van der Vegt and K. Kremer, “Hierarchical Modeling of Polystyrene: From Atomistic to Coarse-Grained Simulations”, *Macromolecules*, Vol. 39, pp. 6708–6719, 2006.
186. Rzepiela, A. J., L. V. Schäfer, N. Goga, H. J. Risselada, A. H. De Vries and S. J. Marrink, “Reconstruction of Atomistic Details from Coarse-Grained Structures”, *Journal of Computational Chemistry*, Vol. 31, pp. 1333–1343, 2010.
187. Ozden-Yenigun, E., E. Simsek, Y. Z. Menciloglu and C. Atilgan, “Molecular Basis for Solvent Dependent Morphologies Observed on Electrosprayed Surfaces”, *Physical Chemistry Chemical Physics*, Vol. 15, pp. 17862–17872, 2013.
188. *Materials Studio*, Accelrys, Inc., San Diego, 2002.
189. Theodorou, D. N. and U. W. Suter, “Detailed Molecular-Structure of a Vinyl Polymer Glass”, *Macromolecules*, Vol. 18, pp. 1467–1478, 1985.
190. *Spartan’08*, Wavefunction, Inc., Irvine, CA, 2006.
191. Berendsen, H. J. C., J. P. M. Postma, W. F. Vangunsteren, A. Dinola and J. R.

- Haak, "Molecular-Dynamics with Coupling to an External Bath", *Journal of Chemical Physics*, Vol. 81, pp. 3684–3690, 1984.
192. Andersen, H. C., "Molecular-Dynamics Simulations at Constant Pressure and-or Temperature", *Journal of Chemical Physics*, Vol. 72, pp. 2384–2393, 1980.
193. Endo, T. and A. Sudo, "Development and Application of Novel Ring-Opening Polymerizations to Functional Networked Polymers", *Journal of Polymer Science Part a-Polymer Chemistry*, Vol. 47, pp. 4847–4858, 2009.
194. Burke, W. J., "3,4-Dihydro-1,3,2h-Benzoxazines - Reaction of Para-Substituted Phenols with N,N-Dimethylolamines", *Journal of the American Chemical Society*, Vol. 71, pp. 609–612, 1949.
195. Ghosh, N. N., B. Kiskan and Y. Yagci, "Polybenzoxazines - New High Performance Thermosetting Resins: Synthesis and Properties", *Progress in Polymer Science*, Vol. 32, pp. 1344–1391, 2007, times Cited: 342.
196. Nair, C. P. R., "Advances in Addition-Cure Phenolic Resins", *Progress in Polymer Science*, Vol. 29, pp. 401–498, 2004.
197. Low, H. Y. and H. Ishida, "Mechanistic Study on the Thermal Decomposition of Polybenzoxazines: Effects of Aliphatic Amines", *Journal of Polymer Science Part B-Polymer Physics*, Vol. 36, pp. 1935–1946, 1998.
198. Low, H. Y. and H. Ishida, "Structural Effects of Phenols on the Thermal and Thermo-Oxidative Degradation of Polybenzoxazines", *Polymer*, Vol. 40, pp. 4365–4376, 1999.
199. Ishida, H. and D. P. Sanders, "Regioselectivity of the Ring-Opening Polymerization of Monofunctional Alkyl-Substituted Aromatic Amine-Based Benzoxazines", *Polymer*, Vol. 42, pp. 3115–3125, 2001.

200. Sudo, A., S. Hirayama and T. Endo, "Highly Efficient Catalysts-Acetylacetonato Complexes of Transition Metals in the 4th Period for Ring-Opening Polymerization of 1,3-Benzoxazine", *Journal of Polymer Science Part a-Polymer Chemistry*, Vol. 48, pp. 479–484, 2010.
201. Sudo, A., R. Kudoh, H. Nakayama, K. Arima and T. Endo, "Selective Formation of Poly(N,O-acetal) by Polymerization of 1,3-Benzoxazine and Its Main Chain Rearrangement", *Macromolecules*, Vol. 41, pp. 9030–9034, 2008.
202. Kimura, H., A. Matsumoto and K. Ohtsuka, "Studies on New Type of Phenolic Resin - Curing Reaction of Bisphenol-A-Based Benzoxazine with Epoxy Resin using Latent Curing Agent and the Properties of the Cured Resin", *Journal of Applied Polymer Science*, Vol. 109, pp. 1248–1256, 2008.
203. Andreu, R., M. A. Espinosa, M. Galia, V. Cadiz, J. C. Ronda and J. A. Reina, "Synthesis of Novel Benzoxazines Containing Glycidyl Groups: A Study of the Crosslinking Behavior", *Journal of Polymer Science Part a-Polymer Chemistry*, Vol. 44, pp. 1529–1540, 2006.
204. Espinosa, M. A., V. Cadiz and M. Galia, "Synthesis and Characterization of Benzoxazine-Based Phenolic Resins: Crosslinking Study", *Journal of Applied Polymer Science*, Vol. 90, pp. 470–481, 2003.
205. Dunkers, J. and H. Ishida, "Reaction of Benzoxazine-Based Phenolic Resins with Strong and Weak Carboxylic Acids and Phenols as Catalysts", *Journal of Polymer Science Part a-Polymer Chemistry*, Vol. 37, pp. 1913–1921, 1999.
206. Wang, Y. X. and H. Ishida, "Cationic Ring-Opening Polymerization of Benzoxazines", *Polymer*, Vol. 40, pp. 4563–4570, 1999.
207. Cid, J. A., Y. X. Wang and H. Ishida, "Cationic Polymerization of Benzoxazine Monomers by Boron Trifluoride Complex", *Polymers Polymer Composites*, Vol. 7, pp. 409–420, 1999.

208. McDonagh, A. F. and H. E. Smith, "Ring-Chain Tautomerism of Derivatives of O-Hydroxybenzylamine with Aldehydes and Ketones. Nuclear Magnetic Resonance Spectra of Immonium Ions", *Journal of Organic Chemistry*, Vol. 33, pp. 8–, 1968.
209. Culbertson, B. M. and J. E. McGrath, *Advances in Polymer Synthesis*, Plenum Press, New York, 1985.
210. Chutayothin, P. and H. Ishida, "Cationic Ring-Opening Polymerization of 1,3-Benzoxazines: Mechanistic Study Using Model Compounds", *Macromolecules*, Vol. 43, pp. 4562–4572, 2010.
211. Kasapoglu, F., I. Cianga, Y. Yagci and T. Takeichi, "Photoinitiated Cationic Polymerization of Monofunctional Benzoxazine", *Journal of Polymer Science Part a-Polymer Chemistry*, Vol. 41, pp. 3320–3328, 2003.
212. Wang, Y. X. and H. Ishida, "Synthesis and Properties of New Thermoplastic Polymers from Substituted 3,4-Dihydro-2H-1,3-Benzoxazines", *Macromolecules*, Vol. 33, pp. 2839–2847, 2000.
213. Liu, C., D. M. Shen, R. M. Sebastian, J. Marquet and R. Schonfeld, "Mechanistic Studies on Ring-Opening Polymerization of Benzoxazines: A Mechanistically Based Catalyst Design", *Macromolecules*, Vol. 44, pp. 4616–4622, 2011.
214. Cossi, M., N. Rega, G. Scalmani and V. Barone, "Energies, Structures, and Electronic Properties of Molecules in Solution with the C-PCM Solvation Model", *Journal of Computational Chemistry*, Vol. 24, pp. 669–681, 2003.
215. Liu, X. and Y. Gu, "Effects of Molecular Structure Parameters on Ring-Opening Reaction of Benzoxazines", *Science in China Series B-Chemistry*, Vol. 44, pp. 552–560, 2001.